Mechanically flexible, transparent conductors based on ultrathin metallic layers

Zur Erlangung des akademischen Grades eines

DOKTOR-INGENIEURS

an der Fakultät für

Elektrotechnik und Informationstechnik
des Karlsruher Instituts für Technologie (KIT)

genehmigte

DISSERTATION

von
Nadia Formica, MSc.
geb. in Catania

Tag der mündlichen Prüfung: 18.5.2015

Hauptreferent: Prof. Dr. Valerio Pruneri
Koreferent: Prof. Dr. Uli Lemmer

DOI: 10.5445/IR/1000048413

Zusammenfassung

Transparente Leiter (TL) sind essenzielle Bauteile vieler Anwendungen, zum Beispiel lichtemittierender Dioden (LEDs), starrer, taktiler Bildschirme, intelligenter Fenster oder von Solarzellen, da sie eine effiziente Lichttransmission erlauben waehrend elektrische Signale angelegt oder gespeichert werden. Derzeit zeigt Indium-dopiertes Zinnoxid (ITO) die beste Balance zwischen hoher optischer Transparenz und geringer elektrischer Resistenz, was es zur ersten Wahl als TL fuer die moisten optoelektronischen Anwenugen macht. Allerdings weist ITO viele gewichtige Nachteile auf, wie hohe Kosten, niedrige mechanische Flexibilitaet und mangelnde Kompatibilitaet mit organischen Komponenten, welche eine Verwendung in zukuenftigen flexiblen und kosteneffizienten Geraeten hoher Leistung verhindert. Eine potentielle Alternative, die diese Einschraenkungen umgeht, sind – dank ihrer grossen mechanischen Flexibilitat, der Moeglichkeit von niedrig-Temperatur Prozessierung und ihrer niedrigen Kosten – Ultraduenne Metallfilme (UTMFs). Allerdings ist ihre moegliche niedrige Haltbarkeit unter oxidierenden und korrosiven Bedingungen ein wichtiges Hindernis fuer viele Anwendungen. In dieser Doktorarbeit wurden verschiedene Kombinationen von UMTFs untersucht und optimiert um zu zeigen, dass sie als effiziente Alternative zu konventionellem ITO dienen koennen. Insbesondere wurden mehrere Designs und Methoden entwickelt um die Stabilitaet von UTMFs zu verbessern unter Bewahrung guter optischer und elektrischer Eigenschaften. Mit dem Ziel flexible Geraete zu entwickeln wurden die neuartigen TL-Strukturen ebenfalls auf flexible Substrate, naemlich Polyethylen therephtalat (PET) und das vor Kurzem entwickelte Corning Willow Ultrathin Glass ®, aufgebracht wobei hohe Transparenz, elektrische Leitfaehigkeit und Stabilitaet gezeigt wurden.

Die groesste Verbesserung an Stabilitaet wurden mittels einer zwischen 0.5 und 1 nm dicken Keimschicht aus Kupfer erreicht, die vor dem Wachstum der Silberschicht aufgebracht wurde. Im Vergleich zu Arbeiten auf dem bisherigen Stand der Technik erweist sich die resultierende Schicht bei wesentlich kleineren Silberschichtdicken als elektrisch leitfaehig (3nm anstelle von 6nm). Sie ist erheblich glatter und stabiler. So zeigt sie keinerlei signifikante Anzeichen von Oxidation selbst nach mehreren Monaten an der Umgebungsluft. Die Doktorarbeit behandelt eine weitere Technik um die Stabilitaet von Silberschichten oder -legierungen gegenueber Temperatur und Oxidation zu erhoehen, die auf einer Schutzschicht aus Nickel basiert. Eine niedrige Dicke der Nickelschicht (~1nm) erlaubt es, die elektro-optischen Eigenschaften der Silberschicht beizubehalten, waehrend das Nickel die Austrittsarbeit der TL-Struktur erhoeht, eine nuetzliche Eigenschaft fuer viele Komponenten. Wir haben die selbe Technik auch fuer Silber-Kupfer-Legierungen verwendet.

Zusaetzlich zur erhoehten Stabilitaet durch die Nickel-Schutzschicht sind die optischen Eigenschaften der Legierungsschicht verbessert, da das Transmissionsspektrum im sichtbaren Bereich wesentlich flacher ist als dies fuer die individuellen Komponenten der Fall ist.

Um verbesserte TL zu erreichen wurden die vorgeschlagenen UTMFs darueberhinaus mit verschiedenen Indium-freien transparenten leitfaehigen Oxiden, wie zum Beispiel Aluminium-dopiertes Zinkoxid (AZO), kombiniert. Wir haben Silber/AZO-Bilayer-Strukturen entwickelt, die die hohe Reflektivitaet von Metallen ablegen koennen, waehrend ihre vorteilhaften elektrischen Eigenschaften und niedrige Schichtdicken beibehalten werden. Ausserdem haben wir zwei verschiedene Ansaetze vorgeschlagen um die Stabilitaet von UTMFs und AZO-Schichten bei hohen Temperaturen und in rauhen Umgebungsbedingungen zu verbessern. In dem ersten Ansatz konnten wir zeigen, dass eine Titanschicht die Stabilitaet des AZO-Films substantiell erhoehen kann ohne die elektro-optischen Eigenschaften zu beeintraechtigen. In dem zweiten Ansatz haben wir gezeigt, dass eine einzige Schicht von Graphen als Schutzschicht gegen die Alterung von sowohl AZO als auch UTMFs dienen kann. Diese Ansaetze stellen damit geeignete Schutschichten fuer TL gegen Sauerstoff und Wasserdampf zur Verfuegung, die die mechanische Flexibiliteat nicht verringern. Wiederholte Beugezyklen beweisen die ausgezeichnete mechanische Belastbarkeit von UTMFs, im Gegensatz zu ITO, welches wie alle Oxide ein zerbrechliches Material ist.

Schliesslich zeigt die vorliegende Doktorarbeit das Potential fuer technische Anwendungen, indem UTMF-basierte TL in organische Solarzellen inkorporiert wurden, mit einer Effizienz vergleichbar zu derjenigen von ITO-Komponenten auf dem derzeitigen Stand der Technik. Die Forschungsergebnisse dieser Doktorarbeit eroeffnen neue Wege fuer kostenguenstige Produktion von flexiblen optoelektronischen Komponenten in grossem Massstab.

Abstract

Transparent Conductors (TCs) are essential components in many applications, such as light emitting diodes, solar cells, rigid and tactile displays and smart windows, since they allow efficient light transmission while electric signals are applied or collected. To date, indium doped tin oxide (ITO) exhibits the best trade-off between high optical transparency and low electrical resistance, making it the first choice as TC for most optoelectronics applications. However, ITO has several important drawbacks such as high cost, poor mechanical flexibility and incompatibility with organic compounds, all of which prevent its use in future flexible and cost-effective high-performance devices. A potential alternative avoiding these restrictions are Ultrathin Metal Films (UTMFs), thanks to their large mechanical flexibility, the possibility of low temperature-processing, and their low cost**.** Their low potential durability under oxidizing and corrosive conditions may be a major concern for several applications**.** In this Thesis, various combinations of UTMFs have been investigated and optimized, to demonstrate that they can serve as an effective alternative to conventional ITO. Most importantly, several designs and methods have been developed for improving the stability of UTMFs, while at the same time still maintaining high optical and electrical characteristics. Aiming at flexible devices, the newly developed TC structures have also been deposited on flexible substrates, namely Polyethylene therephtalate (PET) and the recently developed Corning Willow ultrathin glass ®, and their high transparency, electrical conductivity, and stability have been demonstrated.

The largest improvement in stability has been achieved by employing a 0.5 to 1 nm copper (Cu) seed layer prior to the growth of silver (Ag) films. Compared to prior art work, the resulting film is electrically conductive at much smaller Ag thicknesses (3 nm instead of 6 nm), much smoother and more stable, as it does not show any significant sign of oxidation after several months in ambient air. A technique for increasing further the stability of Ag films or alloys against temperature and oxidation is demonstrated in the thesis. This is based on applying a nickel (Ni) capping layer. While a small thickness of the Ni layer (~1nm) ensures that the Ag layer retains its electro-optic properties, the Ni increases the work function of the TC structure, a useful feature in several devices. We have also applied the same technique on Ag-Cu alloy films. Additionally to the increased stability due to the Ni capping layer, the optical response of the alloy film is greatly improved, because of a much flatter transmission spectrum in the visible region than that of the individual components.

Furthermore, to obtain improved TCs, the proposed UTMFs have been combined with several indium-free transparent conductive oxides, e.g., Aluminum doped Zinc Oxide (AZO). Ag/AZO bilayer structures have been developed that can overcome the high reflection of metals while retaining their favorable electrical behavior and keeping the total film thickness at small values. Also, two different approaches have been proposed to improve the stability of UTMFs and AZO layers at high temperature and in harsh ambient conditions. In a first approach, an ultrathin oxidized Ti layer was found to greatly enhance the stability of AZO film without affecting the electro-optical properties. In a second approach, it was demonstrated that a single sheet of Graphene works as protection layer against degradation both for AZO and UTMFs. The search of proper barrier layers for TCs against oxygen and water vapor was thus addressed without compromising the mechanical flexibility. Repetitive bending cycles demonstrate the superior mechanical strength of UTMFs, unlike ITO which, as all the oxides, is a fragile material.

Finally, the Thesis demonstrates potential for technological applications by incorporating UTMF based TCs in organic solar cells with efficiencies comparable to those with state-of-the-art ITO. The research and results of the thesis open new routes for low cost and large scale manufacturing of flexible optoelectronic devices.

Acknowledgements

This PhD thesis would not have been possible without the assistance of a large number of people.

I would like to thank my supervisor Prof. Valerio Pruneri for his great scientific support and all the things he taught me during those four years. I learned a lot from him not only scientifically but also in terms of presentation and writing skills.

I would like to thank my co-supervisor Prof. Uli Lemmer who welcomed me during my staying in Karlsruhe.

Also I want to thank people in my group for the stimulating discussions and inspiring ideas and more important the friendship I gained. In particular a special thanks goes to Miriam, Fabian, Marc with whom I shared the office where we had a lot of fun, Davide, Ilaria, Miquel, Albert, Dhriti, Tong Lai Chen, Pedro, Valdimar, Roland, Domenico, Judith and Vaghan.

I am also grateful to the Organic Photovoltaics group, especially Professor Jordi Martorell, Pablo, Paola, Alberto, Camilla, Rafael, and the researchers from BASF, J. Hwang, C. Eickhoff, and from Corning Inc., Dr. Prantik Mazumder Dr. Minghuang Huang, Dr. Sean Garner, for their collaboration, their competence and the efficient way we achieved significant results during this thesis work.

I want to thank the members of the thesis committee for taking the time to read this thesis and coming to Barcelona for my defense.

Also I would like to thank all people I met in ICFO and specially the great friends I made during those years, Federica, David, Gonzalo, Alex, Maria Alejandra, Michela, Elsa, Pablo, Roberto, Carmelo, Valeria, Claudia, Noslen, Alberto.

I am thankful to Fabiola, Eliana, Paola, Rita, Anna, Massimo, Ann, Laura, Maria Vittoria, who although the distance always have been demonstrating their love, friendship towards me and support in any circumstance.

My immense gratitude goes to my family, Nina, Pippo, Pamela, Massimo, Aurora, Annemarie, Hans, Sebastian and Desiree, who supported and trusted me. Thanks to them I found the motivation and the enthusiasm to work hard and overcame the difficulties faced during this work. Finally, I thank my husband Philipp who has been always comprehensive with me, cheered me up with his jokes and humor, and gave me his immense love.

Publications

An Indium Tin Oxide-Free Polymer Solar Cell on Flexible Glass, Nadia Formica, Paola Mantilla-Perez, Dhriti Sundar Ghosh, Davide Janner, Tong Lai Chen, Minghuang Huang, Sean Garner, Jordi Martorell, Valerio Pruneri, (just accepted) Applied Materials and Interfaces (2015)

Ultrathin metals and nano-structuring for photonic applications, N. Formica, Albert Carrilero,Tong Lai Chen, Dhriti. S. Ghosh, Prantik Mazumder, V. Pruneri, Proc. SPIE 8982, Optical Components and Materials XI, 89820I (2014)

Ultrathin oxidized Ti to increase stability and smoothness of Al doped ZnO transparent conductors for high efficiency indium-free polymer solar cells, N. Formica, D. S. Ghosh, A. M. Otero, T. L. Chen, J. Martorell, V. Pruneri, Appl. Phys. Lett. 103, 183304 (2013)

Solution processed metallic nanowire based transparent electrode capped with a multifunctional layer, D. S. Ghosh, T. L. Chen, V. Mkhitaryan, N. Formica, V. Pruneri, Appl. Phys. Lett. 102, 221111 (2013)

Cu-Ag alloy capped with Ni transparent electrodes for indium-free orgaicphotovoltaics and lighting devices, D. S. Ghosh, N. Formica, T. L. Chen, J. Hwang, C. Eickhoff, V. Pruneri, Sol. Energ. Mat. Sol. C. 116, 89-93 (2013)

Ultrastable and atomically smooth ultrathn silver films grown on a copper seed layer, N. Formica, D. S. Ghosh, A. Carrilero, T. L. Chen, R. E. Simpson, V. Pruneri, ACS Appl. Mater. Interfaces 5, 3048-3053 (2013)

High figure-of-merit Ag/Al:ZnOnano-thick transparent electrode for indium-free flexiblephotovoltaics, D. S. Ghosh, T. L. Chen, N. Formica, J. Hwang, I. Bruder, V. Pruneri Sol. Energ. Mat. Sol. C. 107, 338-343 (2012)

Highly stable Ag-Ni based transparent electrodes on PET substrates for flexible organic solarcells, N. Formica, D. S. Ghosh, T. L. Chen, C. Eickhoff, I. Bruder, V. Pruneri, Sol. Energ. Mat. Sol. C. 107, 63-68 (2012) IX

Graphene as anti-permeation and protective layer for indium-free transparent electrodes, T. L. Chen D. S.Ghosh, N. Formica, V. Pruneri, Nanotechnology 23, 395603 (2012)

Contents

Chapter I

Introduction

1.1 Transparent Conductors

In many everyday devices, such as displays (liquid-crystal, plasma, light-emitting diode [LED]), touch screens (resistive, capacitive), electronic books, smart windows, thin-film solar cells, light needs to be efficiently transmitted while applying or collecting electrical signals. This function is realized by Transparent Conductors (TCs) whose properties influence the performance of the devices and accordingly their specifications vary based on their requirements. For example, while surface roughness and work function are already important for resistive touch screens, they become absolutely crucial for Organic LEDs (OLEDs) and organic solar cells (OSCs). On the other hand the optical scattering (haze) can increase efficiency in solar cells but reduces view clarity in displays. Mechanical flexibility is indispensable for bendable devices but not essential for devices built on rigid substrates. Table 1.1 summarizes device requirements which pose substantial challenges to the development of TCs, especially for high volume commercial applications.

Nevertheless, optical transmission (T) and electrical sheet resistance (R_s) are crucial parameters in common for all these devices. Any TC's material has a trade-off between T and R_s, since the larger its thickness the lower T and R_s. Often, R_s values are reported at different T, which makes difficult a straight comparison between TCs. For this reason, a figure of merit (σ_{dc} /σ_{op}), where σ_{dc} is the dc (electrical) conductivity and σ_{op} is the optical conductivity, is widely used to evaluate the performance of TCs.

Table 1.1: *List of several TCs' applications and corresponding key features*.

Application	Key Features (Optical transmission and electrical sheet resistance are common features).
Touch Panels	• Mechanical flexibility • Patterning • Stability
Displays	• Surface smoothness • Conformal coating • Color/Haze • Stability
OLED/Solar cell	• Work function • Surface smoothness • Stability

Table 1.2 lists the most common devices, such as displays, touch panels, OLEDs and solar cells together with the sheet resistance and visible light transmission requirements. In a material, σ_{op} is generally described through theimaginary part of the refractive index or the extinction coefficient [1]. Materials like metals that are highly electrically conductive will typically not transmit light, while, on the contrary, materials like glasses are highly transparent but very insulating. The challenge is to decouple these two properties in such a way that one can tune the electrical properties of a material without affecting its optical properties and vice versa. To achieve this, until now, the majority of the effort has been in developing dielectric transparent media into conductive ones without significantly altering their transparency, such as is the case of transparent conductive oxides (TCOs) [2-4]. Less effort has been made from the opposite side, i.e., to increase the optical transparency of electrically conductive materials, such as metals. This will be the approach of this thesis.

Table 1.2: *TC requirements for various devices (T (%) indicates visible total transmission through both the conductive film and the substrate).*

Device Type	T Range (%)	R_s Range (Ω/sq)
Resistive touch panel	86-90	200-500
Projected Capacitive touch panel	88-92	100-300
Surface Capacitive touch panel	88-90	900-1500
LCD	87-90	30-300
OLEDs	>90	<10
Solar cells	90	10-30

1.2 Applications and Market

The TCs' market is rapidly growing with applications in flexible electronics, touch screens, lighting, displays, smart windows, photovoltaics and Electro-Magnetic Interference (EMI) shielding. The application space keeps increasing and a range of product and manufacturing methods needs to be addressed. According to the report from industry analyst firm NanoMarkets, the global market for TCs will exceed $8 billions in revenues by 2018. Figure 1.1 shows the growth rate of TCs' market in different applications. Flat Panel Displays is by far the largest user of TCs but many devices are showing rapid growth such as touch screen sensors and OLEDs. Due to the recent advancements in thin film solar cells, the corresponding TCs' market is expected to fastly grow over the next years.

Besides purely visible light transmission, several other parameters are important for optical devices, including 1) total light transmission 2) type magnitude of color 3) haze level and 4) refractive index.

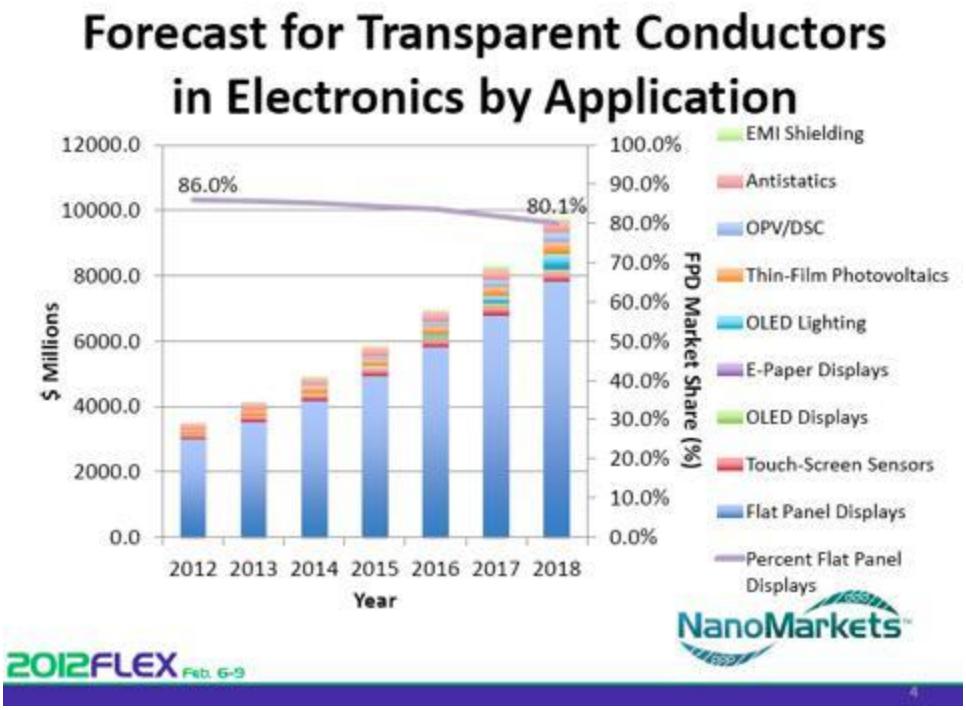

Figure 1.1: *Market forecasts for TCs in different application areas (Source: www.nanomarkets.com).*

Besides the applications discussed above, there are many other application opportunities for TCs, including passive devices such as microwave shielding, transparent loudspeakers, transparent heaters, infrared imaging, or active ones such as artificial actuators, transparent thin-film transistors and transparent thin film energy storage devices. Different applications will require different R_s and T. For example, ~100 kΩ/sq R_s is required for static discharge dissipation, while microwave shielding will require lower sheet resistance for medical applications since the shielding effectiveness increases proportional to log ($1/R_s$). For infrared imaging applications, T in the infrared region is required.

The key technical drivers of the market are (a) large-sized devices, (b) low power consumption, (c) minimal reflection, (d) thinness, (e) low cost, (f) ease of patterning, (g) simplified value chain, and (h) robustness and/or flexibility.

Of these features, the last one, flexibility, would be a major breakthrough in the world of electronics, which will enable a new paradigm in design and functionality for the devices. Flexible devices have already begun to make their way into the commercial realm. They are lightweight, rugged, bendable, rollable, portable, and potentially foldable. However, it still remains a challenge to adapt the processes and materials in the production of today's rigid glass displays to new substrates such as plastic.

Flexible substrates can also be used to print large-area electronics, including displays and solar cells on roll-to-roll systems like those used to print newspapers, potentially enabling significant cost reduction in large volume production. One critical challenge is to guarantee the environmental stability and impermeability to gas and water by a proper design of sealing or barrier layers in flexible devices.This is one of the key aspects investigated by this thesis.

1.3 State-of-the-art and drawbacks

Doped metal oxides, known as transparent conductive oxides (TCOs), are the most widely used TCs. TCOs consist of a group of materials that can be thought of as 'conjugate property materials' in which electrical conductivity is strongly coupled to the optical extinction coefficient. In this regard, it can be stated that materials like metals, that are highly conductive, will not normally transmit visible light, while highly transparent media, like oxide glasses, behave as insulators. The challenge for achieving materials that are both electrically conductive and optically transparent is to decouple these properties through a detailed understanding of the fundamental relationships between the structure of a material and its characteristics.

Among these materials, Indium doped Tin Oxide (ITO) is the most established TC in display industry and in optoelectronic devices. It is a highly doped degenerate semiconductor with

optical band gap above 3 eV; these features make it both transparent to wavelengths greater than approximately 400 nm [5-9] and conductive. A commercial ITO film of 100 nm thickness has typically a sheet resistance of 15-20 Ω/sq and an average visible transparency > 85%, which is an excellent trade-off that meets most of the application-specific device requirements. References to ITO are dated back as early as 1947 (Patent #2564706) [10] making it a very mature technology. Thin films of ITO are mostly deposited using physical vapor deposition techniques, like electron beam evaporation and sputtering.

However, ITO has several important drawbacks. For instance, the migration of indium and oxygen from ITO into organic semiconductors can cause degradation during the operation of devices, such as OLEDs and OSCs [11, 12]. The electrical properties of ITO are sensitive to the condition of the film preparation [13, 14]. Its rough surface limits the efficiency of the hole injection as does its low work function, ~4.7 eV [15]. The typical R_s of ITO, 20~80 Ω/sq, is in some cases still high, which causes a voltage drop along the electro-optic lines, limiting the operation of large area matrix OLED arrays [16]. The R_s has to be even lower in solar cells. In addition, it has been recently reported that ITO is not an optimum electrode for OSC applications because its band structure hinders efficient photocurrent generation [17].

Moreover, the poor mechanical flexibility of ITO is another crucial issue. Since ITO is a fragile oxide, it can crack and fracture at relatively low strains (2–3%), an effect that is increased with fatigue associated to continuous and repetitive use [18]. These micro-cracks can propagate, eventually leading to sharp decreases in the film's electrical conductivity. ITO failure at relatively low strains, though less of an issue for rigid devices, certainly places a limitation on the durability and lifetime of flexible devices. Figure 1.2 shows the Scanning Electron Microscopy (SEM) image of a commercial ITO electrode on Polyethylene Therephtalate (PET)

substrate after bending test with a radius of ~12 mm, with clear evidence of cracking problems. But even in rigid devices, material damage during device handling, assembling, and patterning can be a major concern. Another potential issue with ITO films is its relatively high index of refraction (n ~ 2.0), which leads to unwanted reflection when coupled with lower index substrates and materials. Although anti-reflective coating stacks have been developed to alleviate this problem, these can be quite expensive.

Possibly the most serious one is the high cost of indium metal. Indium is a rare metal that is largely a byproduct of zinc mining [19], thus limiting its supply (which is dominated by China and Canada). Furthermore the sputtering deposition process is quite inefficient with only 3-30% of indium in the sputtering target reaching the film. The unused part of the ITO material also includes the grinding sludge and the after-process residue left on the walls of the sputtering chamber.

Due to the limited supply, recycling ITO is becoming important in industry. One LCD manufacturer has even developed a process to recycle indium directly from old LCD panels by crushing the panels to millimeter-sized particles and then soaking them in an acid solution to dissolve the ITO, from which the indium is recovered [20].While the supplies of indium (and ITO) are limited, the demand for ITO has increased dramatically with the popularity of LCDs (which accounts for 83% of Indium usage) [21], touch panels, e-paper, solar panels, and solid state lighting, all of which use one or more layers of ITO. Also, ITO is deposited via low vacuum based techniques. These factors have resulted in quite large price fluctuations over the last decade, as shown in Figure 1.3 and in table 1.3, with the price reaching $20 per troy ounce during 1980 when the annual average price was $17 to the historical peak of more than $30 per troy ounce in 2005 (The troy ounce (oz t) is a unit of measure which in the present day is most

commonly used to gauge the mass of precious metals. One troy ounce is equivalent to about 31 g). Table 1.3 lists the significant events that affected the indium price. While other device components continue to fall in price, if ITO continues to play such as important role, it will represent an ever increasing fraction of the device cost. Therefore, there is a strong need to find alternative materials to replace ITO as TC.

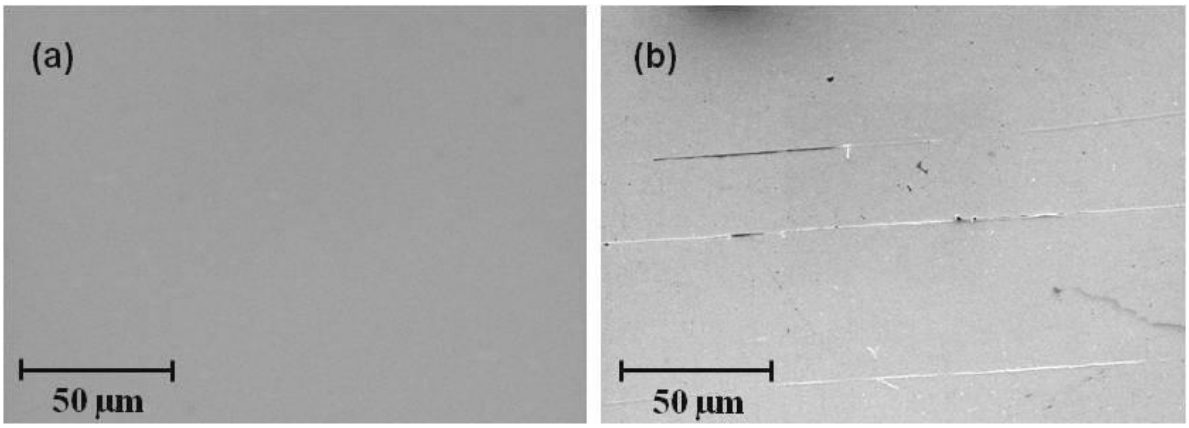

Figure 1.2: *SEM images of* ***(a)*** *ITO, before bending;* ***(b)*** *ITO, after 20 bending cycles [22].*

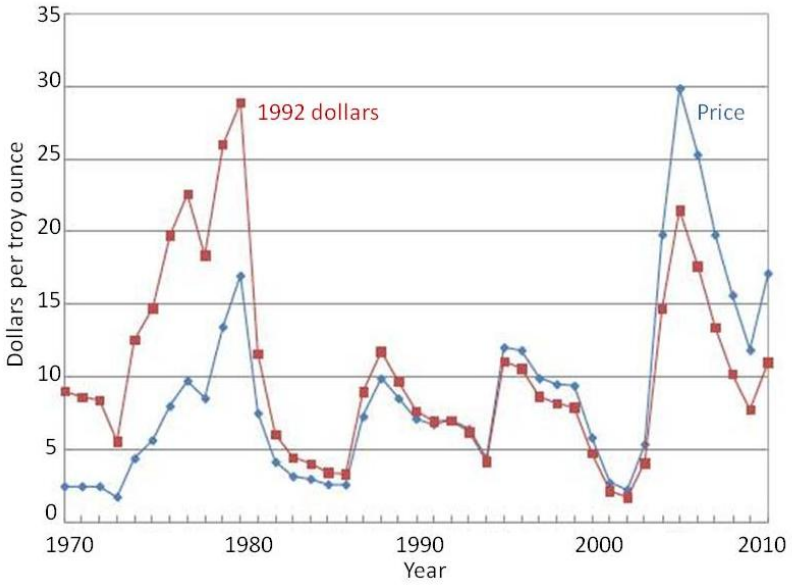

Figure 1.3: *Annual average Indium price per troy ounce over the last several decades (Source: U.S. Geological Survey).*

Table 1.3: *List of events that affected Indium price*

Significant events affecting indium prices since 1970	
1973-80	Period of high demand, significant increase for nuclear control rods
1979	Lower demand after nuclear power plant accident at Three Mile Island
1980-82	Economic recessions
1985	Development of Indium phoshide semiconductors and Indium-tin oxide thin films
1989	Indium added to National Defense stockpile (NDS) Acquisition plan
1992-94	NDS acquisition of Indium : price declined
1995	Steady price increase owing to tight supply and strong demand
1996	Steady price decline owing to greater supply and significant recycling
1997	Release of more than one-half of NDS holdings
1997-98	Reduced demand owing to decrease in production of liquid crystal displays (LCDs) and to shift to more efficient thin-film technology
2003-05	Reduced supply owing to closure of primary production facility in France and several zinc mine closuresin China : price increases
2005-08	Significant increases in secondary capacity and production in Japan
2008-09	Global economic crisis

1.4 Alternative Materials to replace ITO

In order to replace ITO for future applications, a great effort has been done to investigate alternative materials. These include pure SnO_2, Fluorine doped Tin Oxide (FTO), ZnO or ZnO doped with metals (i.e. aluminum (Al), gallium (Ga), etc.) and Antimony doped Tin Oxide (ATO). Among these, Al doped ZnO (AZO) and FTO are considered the most viable alternatives to replace ITO [23, 24]. FTO is also used as TC for OLEDs and OSCs instead of ITO [25, 27], mainly because of its lower cost. Even though it shows relatively good results for devices, several problems prevent its use for high performance device applications. Firstly, its low work

function limits efficient hole injection, especially in OLEDs. Secondly, its rough surface causes high leakage current in organic devices, leading to low efficiencies. Thirdly, the properties of FTO films are strongly dependent on the fabrication method.

AZO, another valid alternative to ITO, is showing promise for TC applications because it uses Zn, which is inexpensive, and because it can achieve electrical conductivity comparable to those of ITO. It has been investigated as a transparent anode in OLEDs. However, optimum performance has yet to be achieved because its work function and real conductivity are lower than those of ITO [28, 29]. Fine tuning of the deposition is also required before practical use, because the electrical properties of AZO films are strongly dependent on the deposition methods and conditions [30]. One of the major concerns for AZO is the electrical stability of the film in humid environments, especially for films thinner than 100 nm. This will be explained in more detail in **Chapter III**.

Even though TCOs show promising characteristics, such as high optical transmittance and electrical conductivity, none of them is the optimum replacement for ITO as TC for future flexible applications because of their limitations associated to high temperature processing and poor mechanical flexibility. In fact, most of these TCOs need high temperature annealing of 300 to 600°C to achieve high transmittance and conductivity, which is not compatible with a flexible plastic substrate. Also, due to their fragility they are easily cracked under bending stress.

Carbon Nanotubes

Carbon nanotube networks (CNTs) are another newly-emerging class of TCs that can potentially replace ITO [31-33]. CNTs are molecular scale tubes of carbon molecules with outstanding properties. One of the critical requirements for CNT films is that the density of nanotubes must

be above the threshold for the formation of percolation networks [34]. Although the conductivity of individual nanotubes is high, the CNTs film conductivity is limited by the large resistance between overlapping CNTs, referred often to as the junction resistance [35].Various methods, such as spin coating, transfer printing and vacuum filtration, have been developed to control thickness, as well as optical and electrical characteristics [36]. One of the major advantages in using CNTs is their mechanical flexibility and compatibility with existing roll-to-roll coating processes, making them suitable for flexible electronics.

However, CNTs have been slow to find a commercial use. One of the major impediments is the inability to obtain bulk quantities of material with suitable purity. CNTs, as produced, typically contain a mixture of various materials including catalyst particles, catalyst support, amorphous or non-tubular carbon, and a mixture of nanotubes of various lengths, diameters, tube number, and chirality. The ability to pick the proverbial needle from this haystack, and do it in large scale and at low cost, remains one of the major material challenges for CNTs.

The best trade-off between R_S and transparency, reported so far, has been 30 Ω/sq and 70%, still far from the requirements of most applications. Therefore, a new fabrication method that can reduce the sheet resistance of carbon nanotube films has still to be developed.

Conductive Polymers

Conductive polymers were reported in the mid of the 20th century as derivatives of polyaniline [37]. Research on such polymers intensified in the 1960s and 70s and even continued in the 21st century [38, 39]. Most conductive polymers are derivatives of polyacetylene, polyaniline, polypyrrole, or polythiophenes [40]. These polymers have conjugated double bonds that allow for conduction. By manipulating the band structure, polythiophenes have been modified to

achieve a HOMO-LUMO separation (bandgap) that is large enough to make them transparent to visible light (HOMO stands for the highest occupied molecular orbital and LUMO for the lowest unoccupied molecular orbital). Transparent conductive polymers have been used as TCs in light emitting diodes and photovoltaic devices [41]. They have conductivity below that of TCOs but do absorb some of the visible spectrum and significant amounts of the mid to near IR. Therefore, they lower the efficiency of photovoltaic devices. On the other hand, despite their lower conductivity transparent conductive polymers can be produced in flexible films making them attractive for flexible devices.

Among them, poly(3,4-ethylenedioxythiophene):poly(styrenesulfonate) (PEDOT: PSS) has gained strong attention. It can be dispersed in water and some organic solvents, and high-quality PEDOT: PSS films can be readily coated on substrates through the conventional solution processing techniques [42, 43]. An as-prepared PEDOT: PSS film from aqueous PEDOT: PSS solution usually has conductivity below 1 S/cm, which is remarkably lower than ITO. Several methods have been reported to enhance further the conductivity of PEDOT: PSS, including the addition of an organic compounds into PEDOT: PSS aqueous solution, such as ethylene glycol, dimethyl sulfoxide (DMSO), ionic liquid, anionic surfactant, or dimethyl sulfate, and the treatment of PEDOT: PSS films with a polar organic compound, salt, zwitterion, carboxylic or inorganic acid, or co-solvent. The lowest R_s (< 65 Ω/sq) with high transparencies (> 80%) have been achieved by Kim et al. [44] by the addition of solvent, and an additional post-treatment method. This improvement was attributed to the removal of PSS from the PEDOT: PSS layer.

However, improving the stability of these conducting polymers is still an important issue since when exposed to UV light, thermal or chemical stress, they can degrade resulting in a decrease in electrical conductivity.

Graphene

Graphene is an allotrope of carbon whose structure is a single planar sheet of sp^2-bonded carbon atoms, densely packed in a honeycomb crystal lattice. It can be described as a one-atom thick layer of the layered mineral graphite. Intrinsic graphene is a semi-metal or zero-gap semiconductor. High-quality graphene is very strong, light, nearly transparent, and an excellent conductor of heat and electricity. Its interaction with other materials and with light, and its inherently two-dimensional nature produce unique properties.

Graphene only reflects < 0.1% of the incident light in the visible region. The optical absorption of graphene layers is linearly proportional to the number of layers, each of them absorbing 2.3% over the visible spectrum.

There are different methods of obtaining graphene, such as expitaxial growth on silicon carbide, on metal substrates, graphite oxide reduction, mechanical exfoliation and chemical vapor deposition (CVD). In general, The R_s of graphene films fabricated by the different approaches strongly depend on their surface morphology and crystal quality. However, the graphene films prepared by these methods are far below the requirement for replacing ITO. Up to now, the most promising way to obtain large area and highly conductive graphene films is the use of CVD. The typical experimental R_s of undoped synthesized graphene is between 2 kΩ/sq and 5 kΩ/sq, roughly 100 times larger than the theoretical minimum [45].

Doping has been reported to be an efficient approach to reduce the R_s of graphene films. Simple atomic or molecular doping can directly modify the carrier concentration of graphene. For example Polyvinil alcohol (PVA) induces n-type doping with values of R_s decreasing from 4 kΩ/sq to 400 Ω/sq while the transmittance value is not affected.

With HNO_3 as p-type doping, the R_s of monolayer grapheme can be decreased from 274 kΩ/sq to 125 Ω/sq. Four-layer doped graphene films fabricated by roll-to-roll process displayed R_s as low as 30 Ω/sq. Although the TCs performance of the doped graphene is much better than undoped graphene, its stability is an issue, especially in air and under thermal loading [46].

Metallic nanowires

Recently, networks of randomly distributed metal nanowires, especially silver nanowires (Ag NWs), have been explored as an emerging TC candidate since these networks maintain the advantages of patterned metal films such as high transparency, low sheet resistance, and mechanical flexibility, and combine that with the low cost manufacturing available with solution deposited roll-to-roll techniques. Solution-processed Ag NW electrodes show excellent performance in terms of transparency and sheet resistance. Coleman et al. [47] prepared films with a transmission value of 85% and R_s of 13 Ω/sq and showed the films to be electromechanically robust (no change in resistance after being bent more than 1000 cycles). Solution-processed Ag NWs thin films exhibit electrical and optical properties comparable with ITOin the visible range and also in the near infrared region. In this latter region, transmittance of ITO decreases for wavelengths >1100 nm while Ag NWs exhibit a flat transmittance spectrum.

However, Ag is also similar to Indium in price ($500/kg). Copper, instead, possesses a comparable conductivity to Ag, is 1000 times more abundant than In or Ag, and is 100 times less expensive. Therefore, Cu-based nanomaterials hold great promise as cheap and scalable TCs. As a result, research has been focused toward designing and developing Cu-based one-dimensional nanostructures. Zeng et al. [48] demonstrated that Cu nanowires (Cu NWs) can be synthesized by a simple room temperature solution process. The size and spacing of the Cu NWs in the mesh

lead to significant light scattering (haze), which is undesirable in many display applications but can help light absorption in the active layer of solar cells.

The large diameter of these nanowires (50 nm–200 nm) causes significant surface roughness in the TC films, which is not desirable for applications with thin active layers. Additionally, the long term environmental electrical stability of such films is a concern, as they can oxidize, even when they are exposed to ambient air. Suitable barrier layers or other corrosion inhibitors may be necessary to prevent the slowdegradation of metallic nanowire film conductivity over time [49].

Beside this drawback, other challenges, such as contact resistance between TC and active materials, electrical shorting problems due to their large aspectratio, uniformity, defects, and scalable fabrication must be overcome to fully integrate metallic NWs into commercial devices.

1.5 Aim of the thesis

Due to their high free-electron density, metals have the highest conductivity among materials at room temperature. In general bulk metals are highly reflective in the visible and near infrared range and cannot function as TCs. However, as the thickness of the metal becomes less than 10 nm, the Ultra Thin Metal Film (UTMF) becomes more transparent to visible light. There is a tradeoff between making the films thin enough to transmit sufficient light without becoming discontinuous, thus suffering from poor electrical conductivity. UTMF based TCs potentially offer a number of advantages, including compatibility with nearly all organic and semiconductor materials and related device fabrication steps, improved mechanical flexibility and low temperature processing**.** In addition their deposition technology, physical vapor deposition, is cost-effective since it can be carried out on large scale using roll-to-roll geometry. Contrary to

ITO, UTMFs are made of abundantly available inexpensive metals, making raw material cost 60 % less than that of ITO films.

The aim of this thesis is the development of UTMF based TCs on glass and polymeric substrates with high electrical and optical performance, which can replace costly and brittle ITO in flexible electronic and optoelectronic applications.

In the thesis, sputtering deposition techniques have been employed to coat with UTMFs the substrates. By changing the deposition parameters, different UTMFs and their combinations have been investigated and optimized, to demonstrate in this way that they can serve as an effective alternative to conventional ITO. Furthermore, to obtain improved TCs, the proposed UTMFs have been combined with some indium-free TCOs, like AZO.

The deposition of TCs on flexible substrates, particularly on plastic, carries several challenges, especially to make them commercially viable, such as long-term environmental stability, coating-substrate adhesion, chemical resistance, internal stress, etc. In the thesis, effort has been devoted to overcome some of these issues.

From a device perspective, it is shown that single component UTMFs or multilayer UTMF based TC structures integrated into organic solar cells allow to achieve electro-optical performance comparable to those of ITO-based devices**.** At the same time they offer the advantage of being mechanically flexible and processable at room temperature, being those crucial aspects for industrialization.

1.6 Thesis Outline

The thesis is organized in seven chapters, the current introductory chapter and 6 additional ones.

In **Chapter II** a brief overview is given on the fundamentals of UTMF based TCs and TCOs. Moreover, it provides a short introduction to the deposition techniques used for fabricating thin TCs together with a description of the experimental equipment used to characterize their main properties. The **Chapter III** discusses in particular an effective method to deposit atomically smooth ultrathin silver (Ag) films by employing a 1 nm copper (Cu) seed layer. The inclusion of the Cu seed layer strongly influences the morphology of the subsequently deposited Ag layer. The wetting of Ag on the substrate is significantly improved by the increased surface energy of theseed material resulting in enhanced electrical properties. Typically, Ag films grown on a dielectric material form rough and granular layers which are not conductive below thicknesses of 10 nm.With Cu acting as seed layer, Ag forms a continuous, smooth,conductive layer down to a thickness of 3 nm with extremely low surface roughness (<0.5 nm).

Cu which is widely used in microelectronics has excellent electrical andoptical properties. The visible optical spectrum of UTMFs within the visible range is non-uniform due to the presence of a characteristic plasma frequency and intraband electronic transitions. A detailed theoretical and experimental investigationon utilizing Cu-Ag alloy films as TCs is described, which can offer a flatter wavelength response with respect to single component UTMFs. In the same chapter, a bilayer structure of metal/oxide (Al:ZnO capped Ag nano-thick film) is studied which can overcome the high reflection of metals, yet retaining their good electrical behavior and keeping the totalfilm-thickness to minimum values. Electrical and optical properties as well as environmental stability of the bilayer structure are theoretically and experimentally studied.

A concern regarding UTMFs is that the outer layers can oxidize, thus increasing the electrical resistivity. This prevents the films from being stable when they are thinner than about 10 nm. Similarly AZO thin films tend to degrade at elevated temperature and even more in the presence of humidity, the effect being correlated with hydrolysis-induced corrosion processes at the grain boundaries. It is thus crucial to design and develop new structures which include protection of films from degradation. **Chapter IV** focuses on the thermal and long-term environmental stability of UTMFs and AZO layers and two different approaches are proposed to improve there liability at high temperature and in harsh ambient conditions. One approach consists in oxidizing intentionally the outer few atomic layers of the metal film, thus passivating the material from further changes. In practice, a protective oxide layer on top of the metallic film is formed, which prevents further oxidation of the metal underneath. Another alternative method of avoiding oxidation and overcomingthis instability is to use a monolayer graphene capping layer to protect the active surfaces with minimal influences on the electricaland optical properties.

Chapter V presents the TCs mentioned above on flexible substrates, Corning Inc. Willow glassand plastic PET. Corning Inc. Willow glassis a thin (0.1-0.2 mm thick) glass sheet, which is mechanically flexible while retains the inherent benefits of glass, such as impermeability to water and surface smoothness. It can also be processed at temperatures up to 500° C, a processing capability that is not within the reach of polymer films. The electrical and optical properties of the proposed flexible TCs are optimized and bending tests are performed to demonstrate that their performance are maintained even under relatively high mechanical stress.

Chapter VI presents a short introduction to photovoltaics, and the developed TCs, described in the previous chapters, are shown to be used efficiently in OSCs. The electro-optical performance of OSCs employing UTMFs and UTMFs combined with metal oxide is comparable to that of

similar devices using commercially available ITO. Also, an OSC on a flexible substrate is demonstrated.

In a conclusive chapter (**Chapter VII**), a brief summary of the main results is presented together with possible future research directions.

References

[1] G. J. Exarhos, X. D. Zhou, Thin Solid Films 515, 7025, 2007.

[2] D. S. Ginley, C. Bright, MRS Bulletin 25, 15, 2000.

[3] B. G. Lewis, D. C. Paine, MRS Bulletin 25, 22, 2000.

[4] T. Minami, MRS Bulletin 25, 38, 2000.

[5] S. K. Park, J. I. Han, W. K. Kim, and M. G. Kwak, Thin Solid Films 397, 49, 2001.

[6] F. L. Wong, M. K. Fung, S. W. Tong, C. S. Lee, and S. T. Lee, Thin Solid Films 466, 225, 2004.

[7] J. Szczyrbowski, A. Dietrich, and H. Hoffmann, Phys. Stat. Sol. A, 78, 243, 1983.

[8] K. Sreenivas, T. S. Rao, A. Mansingh, and S. Chandra, J. Appl. Phys. 57, 384, 1985.

[9] M. Higuchi, S. Uekusa, R. Nakano, and K. Yokogawa, Jpn. J. Appl. Phys. 1, 302, 1994.

[10] J. M. Mochel, U.S. Patent No. 2, 564,706 (7 April 1947).

[11] J. R. Sheats and D. B. Roitman, Synth. Met 95, 79, 1998.

[12] M. P. De Jong, D. P. L. Simons, M. A. Reijme, L. J. van Ijzendoorn, A. W. Denier van der Gon, M. J. A. de Voigt, H. H. Brongersma, and R. W. Gymer, " Synth. Met.110, 1, 2000.

[13] H. Kim, A. Pique, J. S. Horwitz, H. Mattoussi, H. Murata, Z. H. Kafafi, and D. B. Chrisey, Appl. Phys. Lett. 74, 3444, 1999.

[14] J. S. Kim, M. Granstrom, R. H. Friend, N. Johansson, W. R. Salaneck, R. Daik, W. J. Feast, and F. Cacialli, J. Appl. Phys.84, 6859, 1998.

[15] K. Lin, R. S. Kumar, C. Peng, S. Lu, C. Soo-Jin, and A. P. Burden, IEEE Photonics Technol.Lett.17, 543, 2005.

[16] G. Gu and S. R. Forrest, IEEE J. Sel. Top. Quantum Electron. 4, 83, 1998.

[17] W. S. Jahng, A. H. Francis, H. Moon, J. I. Nanos, and M. D. Curtis, Appl. Phys. Lett.88, 093504, 2006.

[18] Z. Chen, B. Cotterell, W. Wang, E. Guenther, and S.-J.Chua, Thin Solid Films 394, 202, 2001.

[19] US National Research Council, Comitte on Critical Mineral Impacts of the US Economy, National Academy Press: Washingtion DC 2008.

[20] U.S. Geological Survey, Mineral Commodity Summaries, January 2009.

[21] www.nanomarkets.com

[22] D. S. Ghosh, T. L. Chen, N. Formica, J. Hwang, I. Bruder, V. Pruneri, Sol. Energ. Mat. Sol. C. 107, 338-343, 2012.

[23] B. H. Liao, C. C. Kuo, P. J. Chen, C. C. Lee, Applied Optics 50, C106, 2011.

[24] S. Fern andez, F. B. Naranjo, Sol. Energ. Mat. Sol. C. 94, 157, 2010.

[25] A. Andersson, N. Johansson, P. Bröms, N. Yu, D. Lupo, and W. R. Salaneck, Adv. Mater. 10, 859, 1998.

[26] F. Yang and S. R. Forrest, Adv. Mater. 18, 2018, 2006.

[27] B. O'Regan and M. Grätzel, Nature 353, 737, 1999.

[28] X. Jiang, F. L. Wong, M. K. Fung, and S. T. Lee, Appl. Phys. Lett.83, 1875, 2003.

[29] H. Kim, C. M. Gilmore, J. S. Horwitz, A. Pique, H. Murata, G. P. Kushto, R. Schlaf, Z. H. Kafafi, and D. B. Chrisey, Appl. Phys. Lett.76, 259, 2000.

[30] T. Minami, Semicond. Sci. Technol. 20, S35, 2005.

[31] Z. Wu, Z. Chen, X. Du, J. M. Logan, J. Sippel, M. Nikolou, K. Kamaras, J. R. Reynolds, D. B. Tanner,. A. F. Hebard, Science 305, 1273–1276, 2004.

[32] E. M. Doherty, S. De, P. E. Lyons, A. Shmeliov, P. N. Nirmalraj,V. Scardaci, J. Joimel,W. J. Blau, J. J, Boland, J. N. Coleman, Carbon 47, 2466, 2009.

[33] M. Zhang, S. Fang, A. A. Zakhidov, S. B. Lee, A. E. Aliev, C. D. Williams, K. R. Atkinson, R. H. Baughman, Science 309, 1215, 2005.

[34] L. Hu, D. S. Hecht, G. Grüner, Nano Lett 4, 2513– 2517, 2004.

[35] D. Hecht, G. Grüner, Eds.; Springer Science Business Media, LLC: New York, 2009; pp 297328.

[36] H-Z. Geng, D. S. Lee, K. K. Kim, G. H. Han, H. K. Park,Y. H. Lee, Chem. Phys. Lett. 455, 275, 2008.

[37] H. Shirakawa, E. J. Louis, Alan G. MacDiarmid, Chwan K. Chiang, AlAn J. Heeger, Journal of the Chemical Society, Chemical Communications 16: 578, 1997.

[38] Historical Background (or there is nothing new under the Sun)" in GyörgyInzelt "Conducting Polymers" Springer, 2008, Berlin, Heidelberg.

[39] Noel S. Hush,Annals of the New York Academy of Sciences 1006, 2003.

[40] Terje A. Skotheim, John Reynold, "Handbook of Conducting Polymers" CRC Press, 1998.

[41] B. Pregan, M. Gratzel, Nature 353, 737, 1991.

[42] F. Jonas Groenendaal,, D. Freitag, H. Peilartzik, J. R. Reynolds, Adv. Mater. 2000, 12, 481.

[43] Y. Cao, G. Yu, R. Menon, A. J. Heeger, Synth. Met.1997, 87, 171.

[44] Y. H. Kim, C. Sachse, M. L. Machala, C. May, L. Müller-Meskamp, K. Leo, Adv. Funct. Mater. 2011, 21, 1076.

[45] F. Bonaccorso, Z. Sun, T. Hasan, A. C. Ferrari, Nature Photonics 4, 611, 2010.

[46] X. Li, Y. Zhu, W. Cai, M. Borysiak, B. Han, D. Chen, R. D. Piner, L.Colombo, R. S. Ruoff, Nano Letters 9, 4359, 2009.

[47] S. De,; T. M. Higgins, P. E. Lyons, E. M. Doherty, P. N. Nirmalraj, W. J. Blau, J. J. Boland, J. N. Coleman, ACS Nano 3, 1767, 2009.

[48] Y. Chang , M. L. Lye, H. C. Zeng, Langmuir 21 , 3746, 2005.

[49] D. S. Ghosh, T. L. Chen, V. Mkhitaryan, N. Formica, V. Pruneri, Appl. Phys. Lett. 102, 221111, 2013.

Chapter II

Basics of Ultrathin Metal and Transparent Conductive Oxides Films

2.1 Introduction to thin films

Thin film technology has been developed primarily to meet the needs of the integrated circuit industry, as the demand for smaller and smaller electronic devices with higher speed has required advanced materials and new processing techniques. Here, ultrathin and nanostructured films can play an important role to achieve giga scale integration (GSI) technology.

The fabrication of thin films is carried out by employing conventional physical and chemical vapor deposition techniques (see Sec. 2.2). Their applications include electronic components, electronic displays, optical coatings, magnetic films for data storage, optical data storage devices, antistatic coatings, and hard surface coatings. Because of their large surface to volume ratio (A/V), associated to a nearly two dimensional geometry, the characteristic of thin films can be quite different from those of bulk materials. Basic research on thin films is generally confined to a limited range of thicknesses, between a few Å to 5000 Å, depending on the properties to be investigated, while for technological applications where the main criterium is the reliability, the thickness typically varies from 1000 Å to 10 μm. In general, a thin film can be defined as a solid layer having a thickness varying from a few Å to about 10 μm. One often distinguishes three classes, ultrathin, thin, and thick films, with a typical thickness of 50-100 Å, 100-1000 Å and greater than 1000 Å, respectively. Regardless the film thickness, an ideal thin film can be mathematically defined as an homogeneous solid material between two parallel planes and extended infinitely in two directions (x and y) but restricted along the third direction (z), perpendicular to x-y plane. A real film, however, deviates from the ideal case since the two

surfaces are never exactly parallel, it can be discontinuous, contain dislocations, impurities, and grain boundaries. The resulting physical, electrical, mechanical and optical properties are thus strongly dependent on the deposition parameters, such as rate, substrate temperature, and atmosphere. Control of the film thickness is a must for reproducible electronic, dielectric, and optical properties.

2.2 Deposition techniques of thin films

There are several methods to deposit thin films via physical or chemical processes, above all physical vapor deposition (PVD) and chemical vapor depositions (CVD) [1]. The CVD process includes the following steps: 1) diffusion of reactant to the surface 2) absorption of reactant to the surface 3) chemical reaction 4) desorption of gas by-products 5) out-diffusion of by-products gas. Figure 2.1 depicts a sketch of the fundamental steps involved in this process. The reaction typically begins in the gas phase due to heating. Reaction products are more reactive with substrate than with source gases and it is necessary to control both gas-phase and surface reactions. The deposition reaction can be of several types including pyrolysis, reduction, oxidation, compound formation, disproportionation, etc. The CVD is more conformal compared to the PVD but it involves more safety and contamination issues since most of the gases are poisonous. Another disadvantage is the high cost for compounds with sufficient purity. The PVD process is an environmentally friendly vacuum deposition technique consisting of three fundamental steps: 1) Vaporization of the material from a solid source assisted by high temperature vacuum or gaseous plasma 2) Transportation of the vapor in vacuum or partial vacuum to the substrate surface 3) Condensation onto the substrate to generate thin films.

The two most common PVD methods are: a) evaporation and b) sputtering. Table 2.1 illustrates all the sub-categories for these two methods. Both evaporation and sputtering methods yield polycrystalline films with typical submicron grain size. In PVD processes, the rate of deposition

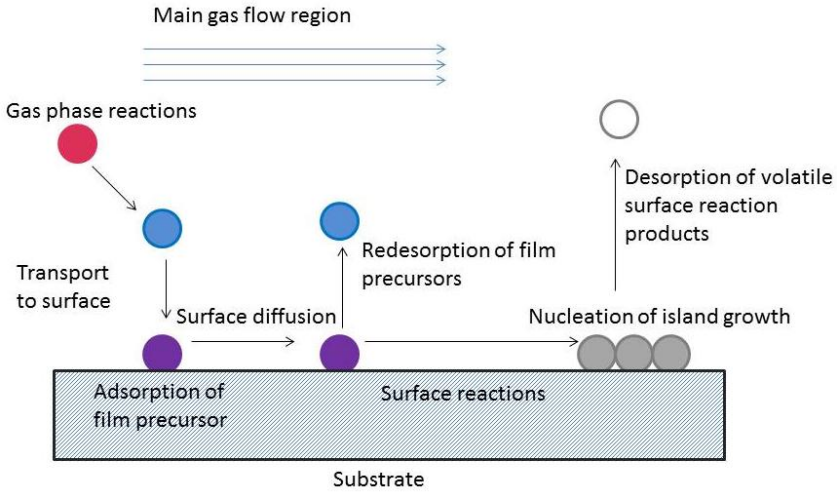

Figure 2.1: *Schematic representation of a PVD process*

depends mainly on chamber pressure, source-substrate distance and substrate temperature. One of the important physical parameters that controls the quality of thin films is the pressure. The lower the pressure (P), the larger the associated mean free path (λ). These two parameters have a simple scaling relation (P ~l/λ). Therefore, in PVD deposition technique, the background pressure must be reduced in order to have a high purity thin film with good quality.

Thus, the quality of the vacuum is very important since gaseous impurities in the deposition chamber can impinge on the growing film resulting in a non-stoichiometric film. Therefore, complete evacuation of a deposition chamber prior to the deposition together with the optimization of growth parameters are necessary to reach high quality thin films.

Due to the importance of contaminants and impurities, the deposition of thin films using PVD relies on ultra-high vacuum systems, i.e. base vacuum levels < 10^{-7} Torr [2-4]. In order to reach film thicknesses below 100 Å (10nm) one must often push process parameters (base vacuum level, gas pressure, power, time of exposure) to extreme limits. Among the different PVD

Table 2.1: *Classification of PVD methods*

Physical Vapor Deposition	
Evaporation	Sputtering
• Thermal	• Direct Current
• Electron Beam	• Radio Frequency
• Ion Plating	• Magnetron
• Laser Ablation	• Reactive
• Molecular Beam Epitaxy	• Bias

processes, sputtering has several advantages including wide-area uniform coverage, ability to coat temperature-sensitive substrate materials, and a virtually unlimited range of materials, from metals to compounds and alloys, can be deposited [5].

Sputtering is a plasma-assisted technique that creates a vapor from the source target through bombardment with accelerated gaseous ions, typically Argon (Ar). The inert gas ions, Ar^+, are generated according to the following ionization process:

$$Ar + e^- \longrightarrow Ar^+ + e^- + e^-$$

The sputtering process can be performed either by gas discharge or ion beam (single or dual as a collimated source). In gas discharge sputtering, the generated ions accelerate within a dark space (sheath) toward the target surface on the cathode side (negative potential), and the substrate for the film deposition is placed at the anode that is usually grounded. The accelerated ions transfer their momentum to the target surface atoms, this collision process resulting in the ejection of atoms. Figure 2.2 illustrates the sputtering dynamics.

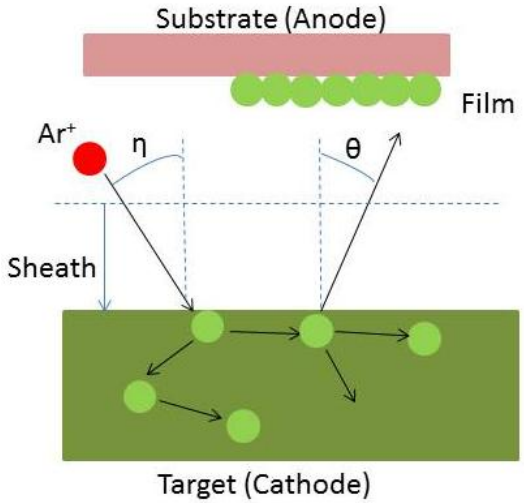

Figure 1.2: *Schematic representation of a sputtering process: 1) acceleration of ion across the cathode sheath 2) atomic collision cascade within the target material and 3) ejection of a target atom(η is the incidence angle and θ is the emission angle).*

The electrical voltage of several 100 volts applied between these plates leads to the ignition of a plasma discharge for typical pressure of 10^{-1}-10^{-3} Torr. The discharge is maintained as the accelerated electrons continuously produce new ions by collisions with the sputtering gas atom (i.e. Ar).

To improve the ionization rate, magnetic fields can be used which force the electrons move to helical paths close to the cathode resulting in a much higher ionization probability and

subsequently yields a higher sputtering rate. In magnetron sputtering, the magnetic field is located parallel to the cathode surface. Secondary electrons, which are emitted from the cathode due to ion bombardment, are constrained by this magnetic field to move in a direction perpendicular to both the electric field (normal to the surface) and magnetic field.

Many variants of sputtering exist today, with Direct Current (DC) sputtering the most appropriate for metals while Radio Frequency (RF) sputtering for dielectrics and special compounds. For insulating films, RF sputtering (instead of DC) must be used to deposit this type of materials due to their high electrical resistivity.

Oxide, nitrides and fluoride compounds can be reactively sputtered starting from metal targets.

In reactive sputtering, the deposited film is formed by chemical reaction between the target material and a gas, which is introduced into the vacuum chamber. Oxide and nitride films are often fabricated using reactive sputtering. The composition of the film can be controlled by varying the relative pressure of the inert and reactive gases. Film stoichiometry is an important parameter for optimizing functional properties like the stress in SiN_x and the index of refraction of SiO_x.

2.3 Growth modes of thin films

The nucleation and the growth of thin films generally occur via condensation of individual atoms or polyatomic species striking the substrate surface. Nucleation steps and the growth mechanisms of films determine the microstructure and morphology of the deposited materials, which ultimately alter physical properties of films such as microhardness, residual stresses, surface roughness, mass density, reflectivity, etc. Therefore, it is important to understand the growth mechanisms of films.

Thin film formation involves basic processes of nucleation and growth. Concerning thin film nucleation on the substrate surface, there are three primary growth types that occur at the earliest stages of film formation. These can be distinguished based on bonding strength between depositing species and the substrate surface atoms. The three growth modes are frequently encountered as: a) Frank-Van der Merwe mode b) Stranski-Krastanov mode, and c) Volmer-Weber mode (see Figure 2.3) [6-8].

- Frank-Van der Merwe mode is defined by the sequential occupation of the atom layers. The growth of the (n+1)th layer starts only after the nth layer has been completed. Therefore this mode is also called two-dimensional layer-by-layer growth. Clearly, two-dimensional nucleation is a prerequisite for layer-by-layer growth. Frequently, imperfect layer-by-layer growth is found in which the growth of (n+1)th layer begins before the nth layer is still completed. In cases where the aim is to produce smooth films, the layer-by-layer growth mode is most favorable.

-Stranski-Krastanov mode identifies an initial layer-by-layer growth that develops into three-dimensional islands above a certain thickness. It can be described in simple terms as a layer-by-layer plus island mode.

-Volmer-Weber mode is defined by the growth of three-dimensional islands on the substrates.

In general, the growth mode is determined by the balance between surface and interfacial free energies of the materials considered. Bauer developed a thermodynamic criterion for the growth mode that neglects the strain energy of the film [9]. This criterion states that under equilibrium conditions, the growth mode is determined by the following energy difference:

(2.1) $$\Delta\sigma = \sigma_f + \sigma_i + \sigma_s$$

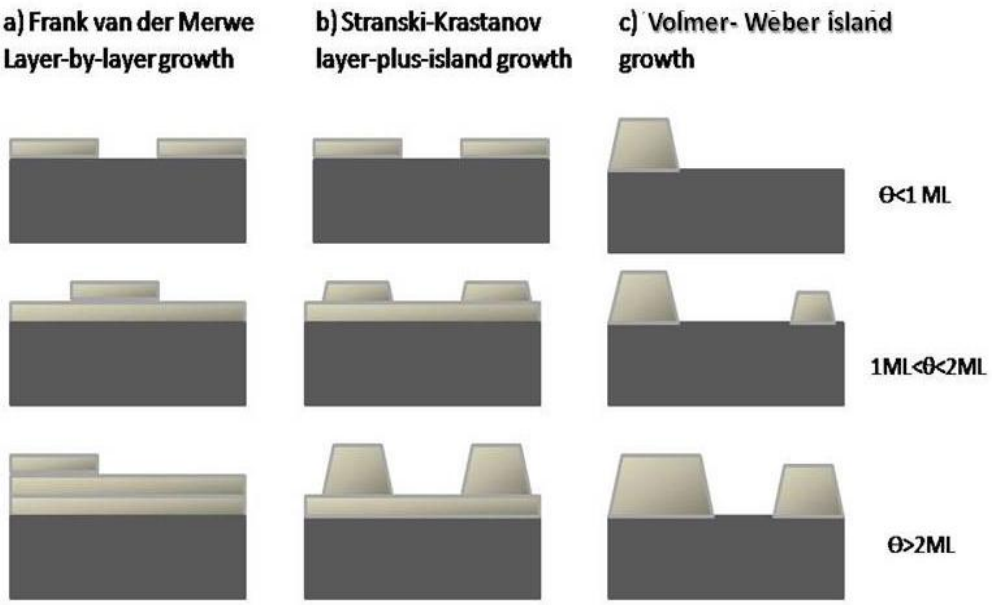

Figure 2.3: *Simplified schematic view of three growth modes of thin film in different θ, where θ is the coverage defined as the number of adsorbed atoms n_a per total surface sites n_o available on the substrate, $\theta = n_a/n_o$ in unit of monolayer ML.*

where σ_s is the surface free energy of the substrate, σ_i is the free energy of the interface, and σ_f the surface free energy of the film.

If the adjacent atoms are more strongly bound to the substrate than to each other, the film tends to extend on (wet) the substrate to minimize the total energy. Under this condition, complete wetting of the substrate is favorable and the Frank-Van der Merwe mode should be observed. The energy difference has the opposite sign when atoms (or molecules) are strongly bound to each other than the substrate. In this case, one usually obtains the Volmer-Weber mode (no wetting of the substrate).

Additionally, the film energy might have a contribution such as the strain energy, which increases linearly with increasing film thickness. After this energy is added, it is possible for $\Delta\sigma$ to be smaller than zero until a certain thickness and larger than zero above this coverage. In this case, the Stranski- Krastanov growth generally occurs.

In our case, it is desirable to achieve the percolation thickness (thickness at which the films becomes continuous of metal films to be as low as possible. Generally, in the case of metal films the adjacent atoms are more bound to each other than to the substrates i.e. $\Delta\sigma \geq 0$, and consequently they grow via the Volmer–Weber (island) mode. To increase the interaction energy with the substrates, we treat the substrates in O_2 or Ar gas plasma inside the sputtering chamber for 15 minutes.

2.4 Electrical conductivity in ultrathin metal films

When the film thickness becomes comparable to the characteristic length scale of a physical phenomenon, the corresponding intrinsic property is affected by the so called finite size-effects. For example, the conductivity is affected by the limitation of size as soon as film thickness becomes comparable to the characteristic length scale of conduction, namely the electron mean free path in the medium. In this section, we will explain the theoretical modeling of thin metal films to interpret properly the experimental data and in particular to understand the relation between the thickness and the electrical resistivity or conductivity in thin metal films.

The theoretical analysis of electrical resistance in thin films has been carried out since the beginning of the last century, with the very first formula due to J. J. Thomson in 1901. Although it already provided a good approximation, the most accepted model, which we describe now, was developed by Fuchs in 1938.

Fuchs model

In the Fuchs model, the film is bounded by two parallel planes separated by a distance equal to the film thickness. This model takes into account the effect of the mean free path of electrons and surface scattering, which is supposed to be entirely diffusive [10]. The main two causes of diffusive scattering are local defects at the surface and surface roughness [11].

Fuchs founds that the conductivity decreased drastically from bulk values for films thinner than the electron mean free path and that the conductivity and the thickness were related via the equation 2.2.

$$\frac{\sigma_\infty}{\sigma_{film}} \approx \frac{4}{3}\frac{1}{(1-p)}\frac{1}{\kappa\, log\frac{1}{\kappa}} \tag{2.2}$$

Here σ_∞ and σ_{film} are the conductivity of the bulk and the thin film, respectively and p is the proportion to the elastic surface scattering. Further, $k = t/l_\infty$ quantifies the ratio of film thickness t and the electron mean free path l_∞. For very thin films, p was found to tend to 0, while for larger thicknesses the proportion of specular reflection was found to grow gradually.

Figure 2.4 shows the fitting between Ni experimental data from Ref. [12] with the Fuchs model of resistivity given by Eq. 2.2. From the fit, we obtain the values of $\rho_\infty = 1/\sigma_\infty$ (bulk resistivity), l_∞ and p.

From Figure 2.4 it is clear that the Fuchs model cannot predict accurately the resistivity of Ultra Thin Metal Films (UTMFs). The values obtained for the coefficients ρ_∞, l_∞ and p are thus not reliable but it is worth noting that $p \approx 0$ is in good agreements with Fuchs prediction of ultrathin

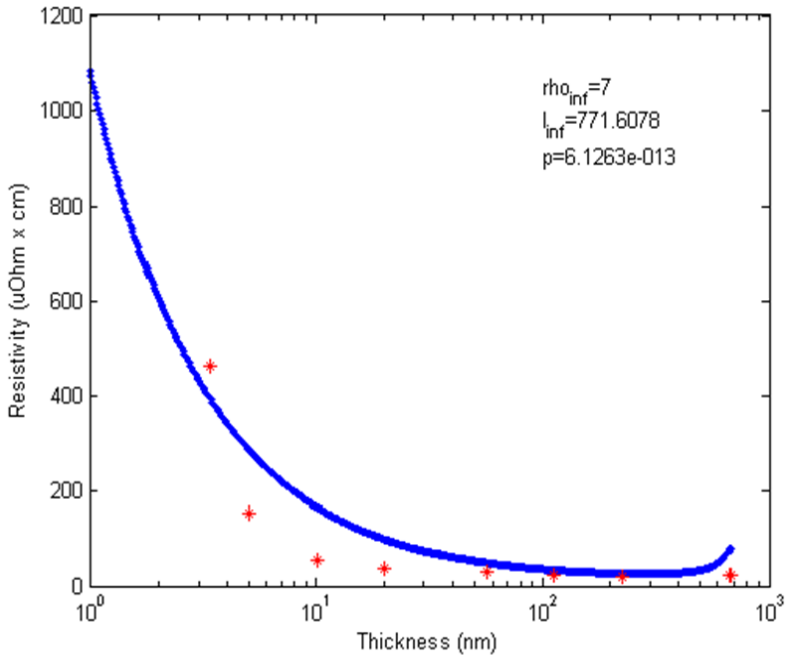

Figure 2.4: *Experimental Ni data (asterisks) fitted with the Fuchs model Eq. 2.2 (solid line). The coefficients obtained with this fitting are also included: ρ_∞= 7 μΩcm, l_∞= 771.60 nm and p≈0 [12].*

metal films and that $\rho = 7\mu\Omega cm$ has the same order of magnitude that Ni bulk resistivity (6.9 μΩcm).

F- Sondheimer model

Fuchs' theory was later reviewed by Sondhemier in 1952. In the so called Fuchs-Sondheimer model (F-S) [13], if a fraction 'p' of electrons is specularly scattered from the two surfaces and the rest of electrons are diffused with complete loss of their velocity, the Fuchs expression assumes the following form:

(2.3) $$\frac{\rho_{film}(t)}{\rho_\infty} = 1/\left[1 - \frac{3}{2k}\int_1^\infty \left(\frac{1}{u^3} - \frac{1}{u^5}\right)\frac{\left(1-e^{-k.u}\right)}{\left(1-pe^{-k.u}\right)}du\right]$$

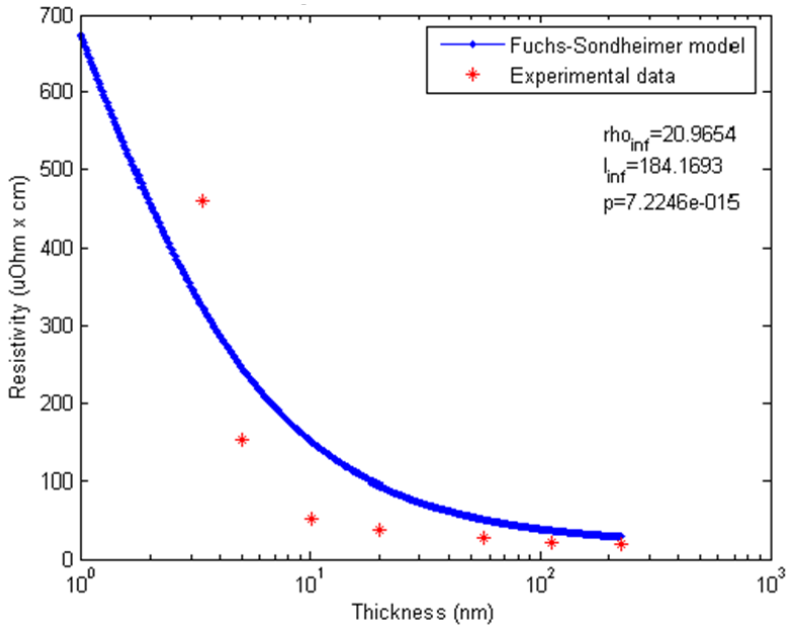

Figure 2.5: *Experimental data (asterisks) fitted with Fuchs-Sondheimer model (solid line). The coefficients obtained with this fitting are also included:* ρ_∞ *= 20. 9654 μΩcm,* l_∞ *= 184.1693 nm and p≈0 [12].*

Although the aforementioned models are adequate to explain the electrical behavior of thin films, they might not be very accurate in the case of UTMFs given their very low thickness (<10nm). For this reason, several new approaches have been developed in the last decades. However, the F-S model remains the most accurate model to predict the electrical behavior of UTMFs as depicted in Figure 2.5.

Besides the geometrical limitation that enhances surface scattering, there are other sources of resistivity that are not due to a size effect but that may be important to thin samples as well:

- Impurities and volume defects
- Lattice vibrations
- Strain, voids and discontinuities, including grain boundaries

All of these are “volume” sources of scattering and are, therefore, are not included in Fuchs’ expressions.

The presence of grain boundaries may reduce significantly the conductivity of metallic materials. When the grain size is of the order of the electron mean free path or lower, grain boundary scattering may become comparable or even more important than external surfaces scattering. Our UTMFs are polycrystalline in nature and are composed of single crystal grains, so this can become an important effect.

Mayadas and Schatzkes (MS) [14] were the first to provide a complete model that takes into account scattering at external surfaces (size effect) and scattering due to grain boundaries. They showed how a reduction of the grain size can induce a significant increase of resistivity. To obtain high conductivity samples, it becomes, therefore, essential to optimize the deposition process to obtain large grain sizes. Another source of large resistivity appears in island growth, since it results in a discontinuous film due to the presence of macroscopic voids between the islands. UTMFs grow usually in an island mode, and for this reason show an electrical resistivity orders of magnitude higher than that of a uniform metal film, grown by a layer-by-layer mode.

2.5 Optical properties of UTMFs

In metals, the optical properties are mainly associated to conduction band electrons, i.e. the metal free electrons gas, and in some cases to intraband transitions. As long as the relaxation time of free electrons is much shorter than the period of the electromagnetic wave, the metal will exhibit a strong absorption and high reflectivity. Indeed, the extinction coefficient k of metals has very high values at low frequency while it becomes negligible for frequencies beyond the plasma frequency, which is generally in the UV or visible region. At larger frequencies, shorter

wavelengths, intraband transitions cause strong absorption reducing the transmission to negligible values.

Due to the reduction of thickness, thin metal films can present small optical absorption and enhanced transmission when the film thickness is less than the penetration depth at optical frequencies. This is usually achievable for thicknesses less than 10 nm.

Figure 2.6 shows the comparison of the optical constants of bulk and 10 nm Ni films. UTMFs have refractive index and extinction coefficients smaller than those of the bulk counterparts. The refractive index and the extinction coefficient of UTMFs can be inferred from the transmittance and the reflectance measurements through the following equations:

(2.4) $$R \cong \frac{(n-1)^2+k^2}{(n+1)^2+k^2}$$

(2.5) $$T \cong \frac{4n}{(n+1)^2+k^2} \cdot \frac{4n\, n_s}{(n+n_s)^2+k^2} \cdot \frac{4n_s}{(n_s+1)^2} \cdot e^{-t\frac{4\pi k_s}{\lambda}} e^{-t_s\frac{4\pi k_s}{\lambda}}$$

where R and T are the reflectivity and transmittance respectively, n_s and t_s are the substrate's refractive index and thickness, n, k, and t refer to the UTMFs' refractive index, extinction coefficient, and thickness respectively.

Optical properties of UTMFs are also affected by the size effect since the dielectric function of metals depends mainly on the conductivity and the number of free electrons. For instance, a shift of the plasma frequency is expected when the resistivity starts increasing due to surface scatterings. Moreover, the polycrystalline nature of the films may affect more the UTMFs than their bulk counterparts.

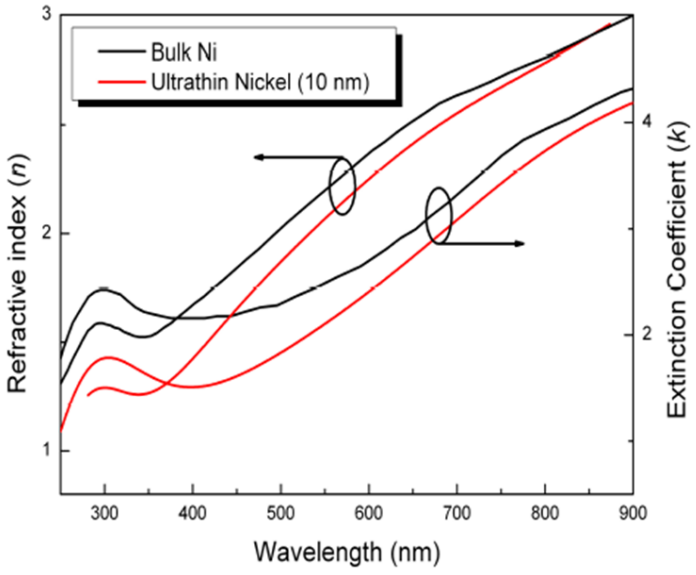

Figure 2.6: *Comparison of optical constants of bulk and 10 nm nickel film. The measurements on UTMFs are carried out using Sopra GES 5E ellipsometer while bulk values are taken from Reference [15]. UTMFs have lower refractive index and extinction coefficient compared to their bulk counterpart.*

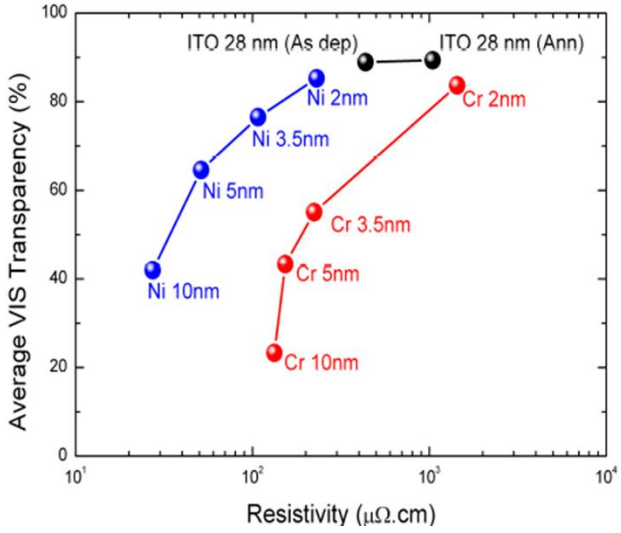

Figure 2.7: *Average optical transparency across the visible wavelengths against electrical resistivity for Cr and Ni films compared to ITO annealed and not annealed from ref. [16].*

Grain and macroscopic surface roughness may induce the presence of voids and discontinuities in the volume of the metal film and give rise to a non uniform distribution of matter.

Figure 2.7 shows the average optical transparency in the visible range and the electrical resistivity for Cr and Ni films of different thickness compared also with ITO layers, both as deposited and annealed from Ref. [16]. In the visible range Ni films present an optical transparency similar to ITO with a significantly lower electrical resistivity. However, the real advantage of UTMFs over ITO in terms of optical transparency is in the IR and UV region. Figure 2.8 shows the IR transparency of Cr and Ni films, both compared with 28 nm thick ITO films, where both metal thin films present larger and flatter transparency in comparison with a standard ITO. Even more in the UV range ITO films exhibit reduced transparency and enhanced

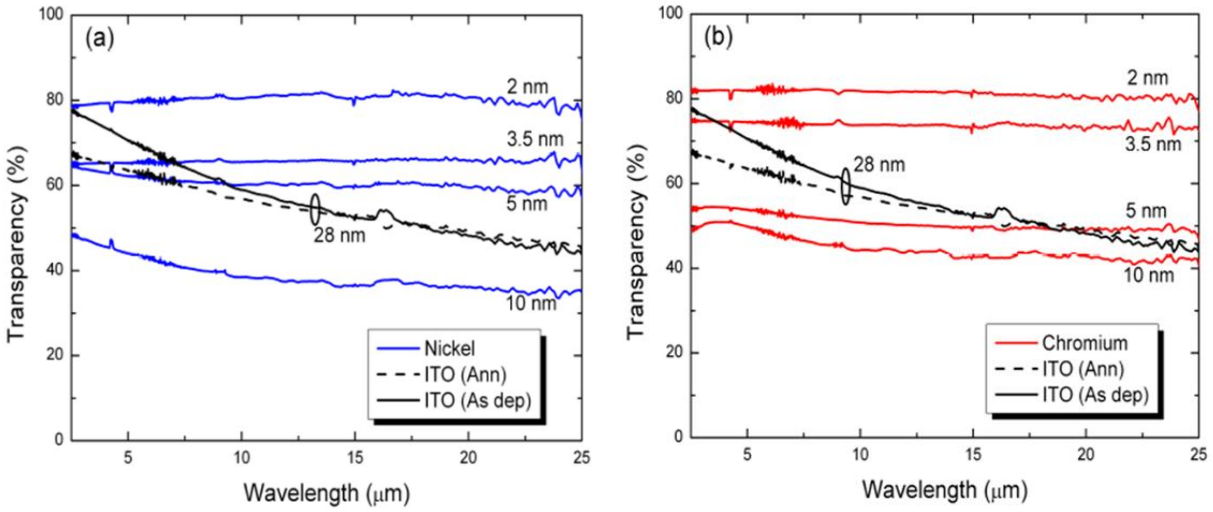

Figure 2.8: *Optical transparency in the mid-IR region of (a) Ni and (b) Cr thin films compared to ITO annealed and as deposited [16].*

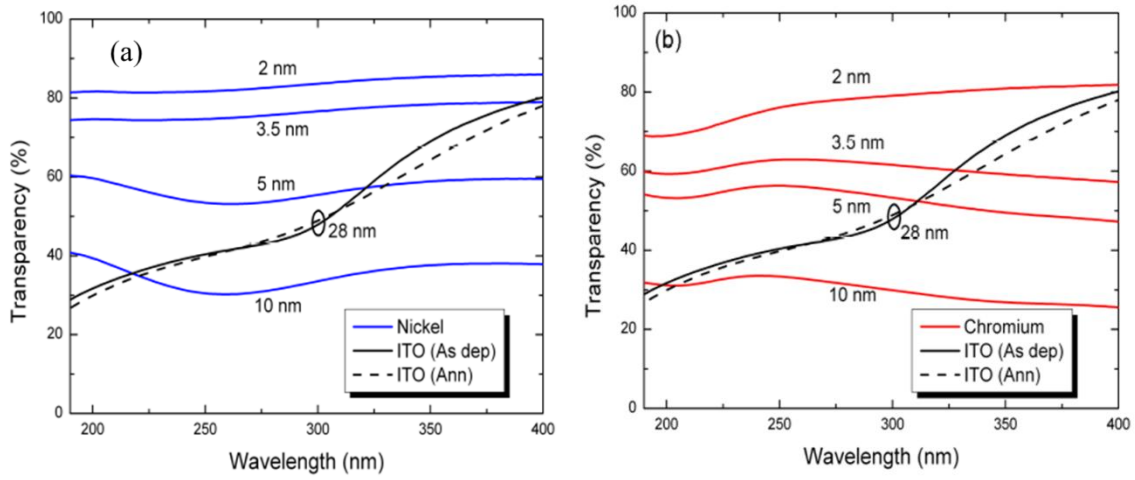

Figure 2.9: *Optical transparency in the UV region of a) Ni and b) Cr UTMFs compared to ITO annealed and as deposited from ref. [16].*

absorption due to material band gap, as we will discuss discussed in Section 2.7. On the contrary, Cr and Ni films possess flatter optical transparency with levels comparable to those in the visible range, as shown in Figure 2.9.

2.6 Electrical conductivity of TCO materials

TCOs are wide band gap semiconducting oxides, with resistivity ρ in the range 10^{-2} – 1.2 ×10^{-6}Ω cm. In the absence of doping, these oxides become very good insulators, with ρ > 10^{10}Ωcm. The conductivity is due to doping either by oxygen vacancies or by extrinsic dopants. Most of the common TCOs are n-type semiconductors. The electrical conductivity of n-type TCO thin films depends on the density of the electrons in the conduction band and on their mobility: $\sigma=\mu n e$ where μ is the electron mobility, n is its density, and e is the electron charge. The mobility is given by:

(2.6) $$\mu = \frac{e\tau}{m^*}$$

where τ is the mean time between collisions, and m^* is the effective electron mass. However, because n-type doping increases n but at the same time decreases τ, the magnitude of μ is limited. Due to the large energy band gap, Eg, (Eg> 3 eV), separating the valence band from the conducting band, the conduction band cannot be thermally populated at room temperature (k_BT~0.025eV, where k_B is Boltzmann's constant). Hence, stoichiometric crystalline TCOs are good insulators [17]. To explain the TCO characteristics, various population mechanisms and several models describing the electron mobility were proposed. For example, via electronic structure studies [18], certain characteristics of the mobility and the processes by which the conduction band is populated with electrons were shown to be interconnected, e.g., that the mobility is proportional to the magnitude of the band gap.

In the case of intrinsic materials, the density of conducting electrons has often been attributed to the presence of unintentionally introduced donor centers, usually identified as metallic interstitials or oxygen vacancies that produced shallow donor or impurity states located close to the conduction band. The excess or donor electrons are thermally ionized at room temperature, and move into the host conduction band. However, experiments have been inconclusive as to which of the possible dopants was the predominant donor [19]. Extrinsic dopants have an important role in populating the conduction band, and some of them have been unintentionally introduced. Thus, it has been conjectured in the case of ZnO that interstitial hydrogen, in the H^+ donor state, could be responsible for the presence of carrier electrons [20]. In the case of SnO_2, the important role of interstitial Sn in populating the conducting band, in addition to that of oxygen vacancies, was conclusively supported by first-principle calculations carried out by Kiliç and Zunger [21]. They showed that Sn interstitials and O vacancies, which dominated the defect structure of SnO_2 due to the multivalence of Sn, explained the natural nonstoichiometry of this

material and produced shallow donor levels, turning the material into an intrinsic n-type semiconductor [20]. The electrons released by these defects were not compensated because acceptor-like intrinsic defects consisting of Sn voids and O interstitials did not form spontaneously. Furthermore, the released electrons did not make direct optical transitions in the visible range due to the large gap between the Fermi level and the energy level of the first unoccupied states. Thus, SnO_2 could have a carrier density with minor effects on its transparency [20].

The conductivity σ is intrinsically limited for two reasons. First, n and μ cannot be independently increased for practical TCOs with relatively high carrier concentrations. At high conducting electron density, carrier transport is limited primarily by ionized impurity scattering, i.e., the Coulomb interactions between electrons and the dopants. Higher doping concentration reduces carrier mobility to such a degree that the conductivity is not increased, and it decreases the optical transmission at the near-infrared edge. With increasing dopant concentration, the resistivity reaches a lower limit, and does not decrease beyond it, whereas the optical window becomes narrower. Bellingham et al. [22] were the first to report that the mobility and hence the resistivity of TCOs (ITO, SnO_2, ZnO) are limited by ionized impurity scattering for carrier concentrations above 10^{20} cm^{-3}. Ellmer also showed that in ZnO films deposited by various methods, the resistivity and mobility were nearly independent of the deposition method and limited to about 2×10^{-4}Ωcm and 50 cm^2/Vs, respectively [23,24]. In ITO films, the maximum carrier concentration was about 1.5×10^{21} cm^{-3}, and the same conductivity and mobility limits also held [25]. This phenomenon is a universal property of other semiconductors [26-27]. Scattering by the ionized dopant atoms that are homogeneously distributed in the semiconductor is only one of the possible effects that reduces the mobility. More recently developed TCO

materials, including doped and undoped binary, ternary, and quaternary compounds, also suffer from the same limitations. Only some exceptional samples had a resistivity of $\leq 1 \times 10^{-4}\Omega$cm.In addition to the above mentioned effects that limit the conductivity, high dopant concentration could lead to clustering of the dopant ions [28], which increases significantly the scattering rate, and it could also produce non parabolicity of the conduction band, which has to be taken into account for degenerately doped semiconductors with filled conduction bands [29].

2.7 Optical Properties of TCO materials

As mentioned above, besides low resistivity, effective TCO thin films should have a very low absorption coefficient in the near-UV,VIS and near-IR region. The transmission in the near UV is limited by the energy band gap (Eg), as photons with energy larger than Eg are absorbed. A second transmission edge exists in the near IR region, mainly due to reflection for frequencies below the plasma frequency. Ideally, a wide band gap TCO should not absorb photons in the transmission "window" in the near-UV,VIS, near-IR region. However, there are no "ideal" TCO thin films, and even if such films could be deposited, reflection and associated interference effects would still affect significantly the transmission [30].

The optical properties of TCOs' transmission (T), reflection (R), and absorption (A), are determined by their refractive index (n), extinction coefficient (k), band gap (Eg), and geometry. Geometry includes film thickness, thickness uniformity, and film surface roughness. T, R and A are intrinsic parameters, depending on the chemical composition and solid structure of the material, whereas the geometry can be considered extrinsic. There is an opposite trend (negative correlation) between the carrier density and the position of the IR absorption edge, while the correlation is positive between the carrier density and the UV absorption edge, as Eg increases at

larger carrier density (Moss-Burstein effect) [31]. As a result, the TCO transmission boundaries and conductivity are strongly connected to each other.

The width of the VIS transmission window of a TCO film with any thickness deposited on a transparent substrate is affected not only by the optical parameters of the TCO film but also by the optical properties of the substrate. The n_s of the most common substrates are: ~1.45 for fused silica and ~1.6 for various doped glasses. The k_s is generally negligible (< 10^{-7}), so that any light absorption would take place in the film, where generally k_{film}>k_s. For films thicker than 100 nm, several interference bands could be formed, producing maximal and minimal values of T when either the wavelength or thickness is varied. When $k_{film} \approx 0$, the peak transmission (T_{max}) is equal to the transmission of the substrate. Hence, assuming that the sample is in air, T_{max} = 90% and 93% for films deposited on glass and fused silica, respectively. The minimum sample transmission (T_{min}) in air is expressed by:

(2.7) $$T_{min} = \frac{4\,n^2 n_{sub}}{(1+n^2)(n^2+n_{sub}^2)}$$

As most TCO films have values of n in the VIS in the range 1.8 – 2.8, T_{min} will be in the range 0.8 – 0.52. T_{min} is closely approximated by the relation: T_{min} = 0.051 n^2-0.545 n+1.654. As n in the VIS decreases with wavelength, T_{min} increases with wavelength, but will not exceed ~0.8. When the film extinction coefficient is not negligible and affects the transmission, T_{max}<T_{sub}, and T_{min} also decreases. By decreasing the TCO film thickness, T is increased but the sheet resistance decreases. Combining together the optical and electrical properties of the film, the fraction of the flux absorbed in a film (A) is given by the expression:

(2.9) $$A \cong 1 - e^{-\frac{\alpha}{\sigma R}}$$

where α is the absorption coefficient. For a given σ, low values of R_S necessitate thick films, and lower conductivity requires the use of even thicker films, resulting in an increase in the loss of radiative power.

Using the same film conductivity, applications requiring the lowest R_s will be thicker and, and the absorbed fraction will be larger. At present, only high quality ITO is compatible with the condition that the absorbed power fraction be lower than 10% and R_s= 10 Ω/sq. At lower k films with lower conductivities can be used, e.g., when k = 0.002 instead of 0.02, the absorbed power A is lower by a factor of ~8, and allows the use of thicker films.

References

[1] K. Seshan, Handbook of Thin film Deposition Techniques, Principles, Methods, Equipment and Applications, CRC Press, 2002.

[2] R. Messier, Journal of Vacuum Science and Technology A 4, 3059, 1986.

[3] J. A. Thornton, Journal of Vacuum Science and Technology 11, 666, 1974.

[4] J. A. Thornton, Thin Solid Films 40, 335, 1977.

[5] B. Dieny, V. S. Speriosu, S. S. P. Parkin, B.A. Gurney, Phys. Rev. B 43, 1297, 1991.

[6] F. C. Frank and J. H. van der Merwe: Proc. Roy. Soc. A 198, 205, 6, 1949.

[7] M. Volmer and A. Weber: Z. Phys. Chem. 119, 6274, 1981.

[8] J. N. Stranski and L. Krastanov: Ber. Akad.Wiss.Wien 146, 797, 6, 1938.

[9] E. Bauer: Zeitschr. f. Kristallographie 110, 372, 1958.

[10] K. Fuchs, H. H. Willis,Proc Cambridge Philos. Soc. 34: 100, 1937.

[11] G. Fischer, H. Hoffman, J. Vancea, Physical Review B 22, 12: 6065, 1980.

[12] Master Thesis, L. Martinez, Transparent metal electrodes, ICFO.

[13] E. H. Sondheimer,Advances in Physics 1:1, 1952.

[14] A. F. Mayadas, M. Schatzkes, Physics Review B 1:1382, 1970.

[15] E. D. Palik, Handbook of Optical Constants of Solids, Academic Press, 1985.

[16] D. S. Ghosh, L. Martinez, S. Giurgola, P. Vergani, and V. Pruneri Optics Letters, 34, 3, 325, 2009.

[17] P. P. Edwards, A. Porch, M. O. Jones, D. V. Morgan, and R. M. Perks, Dalton Trans. 19, 2995, 2004.

[18] H. Mizoguchi and P.M. Woodward, Chem. Mater., 16, 5233, 2004.

[19] D.C. Look, B. Claflin, in: G.J. Brown, M.O. Manasreh, C. Gmachl, R.M. Biefeld, K. Unterrainer (Eds.), Materials Research Society Symposium Proceedings, 829, 2005, B8.6.1.

[20] C.G. Van de Walle, Phys. Rev. Lett.85**,** 1012, 2000.

[21] C. Kiliç and A. Zunger, Phys. Rev. Lett. 88, 095501-1, 2002.

[22] B. Thangaraju, Thin Solid Films, 402, 71, 2002.

[23] K. Ellmer, J. Phys., D, Appl. Phys.33, R17, 2000.

[24] K. Ellmer, J. Phys., D, Appl. Phys.34, 3097, 2001.

[25] G. Frank, H. Köstlin, Appl. Phys. A 27, 197, 1982.

[26] G. Masetti, M. Severi, S. Solmi, IEEE Trans. Electron Devices, ED30, 764, 1983.

[27] D. Chattopadhyay, H.J. Queisser, Rev. Mod. Phys.53, 745, 1981.

[28] P. Ebert, Z. Zhang, F. Kluge, M. Simon, Z. Zhang, K. Urban, Phys. Rev.Lett.83**,** 757, 1999.

[29] T. Pisarkiewicz, K. Zakrzewska, E. Leja, Thin Solid Films, 174, 217, 1989.

[30] Jorge I. Cisneros, Applied Optics, 37, 5262, 1998.

[31] Marius Grundmann, The Physics of Semiconductors, Springer Berlin Heidelberg New York: Springer (2006).

Chapter III

Growth and optimization of ultrathin metal and Al doped ZnO (AZO) based transparent conductors

Very recently, semitransparent Ultra Thin Metal Films (UTMFs) have been used as transparent conductors (TCs) in several devices, e.g. organic lighting [1-2] and organic solar cells (OSCs) [3-4]. UTMFs have cost and processing advantages over the most widely used transparent conductive oxide (TCO), indium tin oxide (ITO).

Among UTMFs, Ag and Cu have been extensively studied since they show high electrical conductivity and relatively high transparency in the visible wavelength range. There are various reports on using different forms of Ag and Cu as stand-alone layer or in conjunction with other materials as TCs for OSCs [5-8].

In this chapter we show that Ag and Cu films can be effective TCs over the visible range and that, when combined with an indium-free TCO like Al: ZnO (AZO), they can show improved electro-optical performance, thus making them a competitive replacement to ITO.

Before presenting the experimental results obtained, we first introduce the equipment which has been used for the deposition and characterization of the investigated thin films.

3.1 Deposition and characterization of UTMFs and AZO thin films

Sputtering equipment

At ICFO, we have two different kinds of sputtering system for deposition of UTMFs, ATC Orion 3 HV and, a more recent, advanced ATC Orion 8 HV. Both of them are magnetron sputterers having different configurations and were manufactured by AJA International Incorporation [9]. Orion 3 HV is a single target, low throughput R&D engine, allowing both

Figure 3.1: *The ATC Orion 3 HV sputtering installed in the Nanophotonics Lab, ICFO.*

DC and RF magnetron sputtering in pure Ar atmosphere. Its set-up is planar, with a fixed target (and magnetic field) and a pendulum oscillating platform for the substrate. No degas chamber is available and depositions can only be made at room temperature. Orion 3 HV's pumping system is composed of dry rotary vane pump which allows to reach a base vacuum pressure level of 10^{-7} Torr (4 hours stand-by) in the deposition chamber. Each target has a diameter of 2 inches allowing good deposition uniformity (<2.5%) over a maximum area of ~ 4 inches. The ATC Orion 8 HV sputtering system instead is a computer controlled fully automatic RF/DC deposition system with co-planar configuration and can have 7 different target materials installed at the same time. The target size diameter is 2 inch and the system reaches thickness uniformity of 2.5% over 4 inch diameter substrates. It has an integrated load lock system for sample transfer without breaking the vacuum of the main chamber. The ATC Orion 8 HV has 2 radio frequency and 2 direct current power sources which allows co-sputtering as well. The system also allows deposition at higher temperature, up to 800 ºC and has an O_2 reactive gas line, apart from an Ar line (process gas). Substrates are placed on a

rotating sample holder that can spin around the axis of the chamber up to a maximum rotation frequency of 40 revolutions/min. The main chamber is connected to a turbo pump which can reach a base vacuum level of 5 x 10^{-8} Torr in just 3 hours of standby time while the load lock is pumped by a smaller rotary pump. The system is also fitted with a quartz crystal thickness monitoring unit by which the deposition rates can be deduced.

Once the UTMFs have been sputtered, their main properties are measured and analysed. The continuity and uniformity of the films were first determined by surface roughness and then verified through electrical conductivity measurements. As discussed before, TCs require high levels of transparency and electrical conductivity.

Surface and morphological analysis

Studies concerning the structure and the roughness of the substrates as well as the sputtered films were carried out by using Atomic Force microscopy (AFM), a technique especially suitable for surface roughness measurements with atomic resolution.

In an AFM, the z-position information is obtained by measuring the deflection of a laser beam reflected on the cantilever where the tip is located. When the tip is brought in contact with the film's surface the interaction forces between them, such as Van der Waals, capillary or electrostatic forces, bend the cantilever thus deflecting the laser beam. The instrument used to perform surface roughness analysis at ICFO is a Digital Instrument D3100 AFM. The images obtained using the AFM techniques were processed using the associated WSxM software. They were first flattened to correct the different behaviour of the instrument in different positions of the scanned area. A progressive filtering on the image was performed to reduce the electrical noise. Surface roughness was finally obtained according to the following formula:

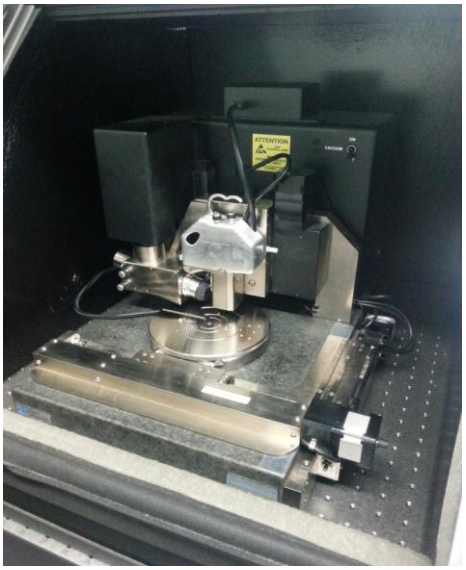

Figure 3.2: *Atomic Force Microscope at ICFO used for the surface topography characterization.*

(3.1) $$Roughness_{RMS} = \sqrt{\frac{1}{n_1 n_2}\sum_{i=0}^{n_1}\sum_{j=0}^{n_2}(z_{ij} - z_{average})^2}$$

where n_1 and n_2 are the numbers of pixels in the vertical and horizontal directions, respectively, z_{ij} is the z level of the (i,j) pixel and $z_{average}$ is the average of all the pixels' heights.

Electrical characterization

As mentioned before, the UTMFs electrical resistivity (ρ_t) depends on the thickness. It is very common to measure the electrical surface properties of a film through the sheet resistance (R_s) in Ω/square units:

(3.2) $$\rho = R_s \times t$$

where t is the film's thickness. R_s can be measured directly using a Four-point probe set up connected to a multimeter. The schematic set-up is shown in Figure 3.3.

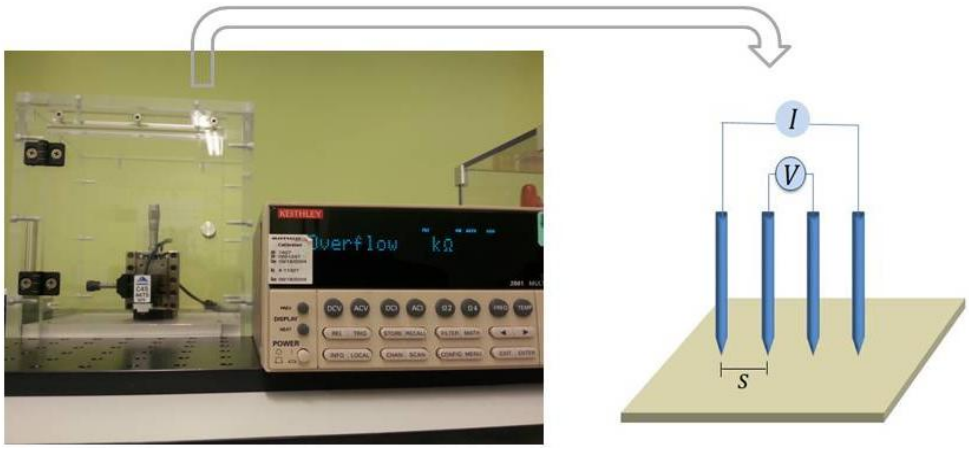

Figure 3.3: *Four Probe Point set-up in ICFO used for the sheet resistance measurements (left) and pictorial representation of the four probes on the sample (right).*

To obtain the electrical resistivity of the UTMFs, R_s was measured using a Cascade Microtech 44/7S 2791 Four-Point Probe and Keithley 2001 Multimeter. The four tips installed in the Four-Point probe were brought in contact with the layer. A test current is injected through the two outer tips while the two inner probe tips collect the voltage drop.

Typically 6 measurements were taken, each at different position in the film and the mean value of R_s is calculated as:

(3.3) $$R_s = C_1 \times C_2 \times R$$

where R_s is the average electrical resistance obtained by the multimeter and the two corrective coefficients C_1 and C_2 take into account the separation between the tips in the Four-probe Head and the substrate's dimensions. In our case the separation between the tips is 1 mm and the diameter of the samples is usually 2.5 cm (1 inch). As the UTMF thickness is usually lower than the spacing between the tips, the first coefficient C_1 is kept at a constant value (C_1=1) while the second corrective coefficient C_2 is calculated to be 4.4364 for 1 inch

substrates. The electrical resistivity of the films is finally inferred using the definition of R_s given by the eq. (3.3).

Transparency analysis was performed using a Fourier Transform Infrared Spectrometer, while optical constants (refractive index and extinction coefficient) were determined by ellipsometry.

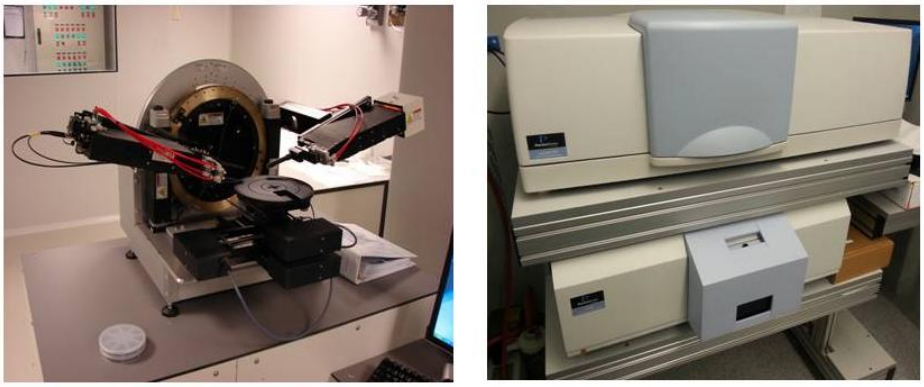

***Figure 3.4**: Pictures of the ellipsometer set up (left) and the Fourier Transform Infrared Spectrometer (right) used for the experiments at ICFO.*

3.2 Optimization of ultrathin silver films growth by copper seed layer

Innovative applications with UTMFs often rely on Ag films. However, when deposited with conventional methods, such as electron beam evaporation, chemical vapor deposition, electroless plating, and sputtering, Ag films tend to grow on dielectrics or oxidized surfaces in island-like mode (Volmer-Weber growth mode) [7] and, consequently, exhibit a rough surface morphology with a large grain size and high electrical resistivity [10-12].

Therefore, it is of great importance for numerous practical applications to fabricate ultra-smooth Ag films with a sub-nanometer scale roughness, low resistivity and a high degree of

thickness uniformity. A recent work [13] has demonstrated that by a combination of template stripping and patterning on silicon substrates, a 30 nm thick thermally evaporated Ag film with 0.34 nm root mean square (RMS) roughness can be obtained. Further studies [14-15] showed that the use of transition metal seed layers also improves the quality of Ag surface morphology, giving rise to a semitransparent, homogeneous, spike free, conductive and adherent layer. Logeeswaran et al. [16] reported a simple method to create ultra-smooth Ag films by electron beam evaporation of a germanium (Ge) seed layer with a thickness of 0.5-15 nm atop of SiO_2/Si(100) substrates. A dramatic reduction of surface roughness down to about 0.6 nm (RMS) was achieved. Although deposition of Ge on silicon or oxidized substrates leads to a Volmer-Weber growth mode, the density of Ge nuclei was much larger and the islands were significantly smaller than those for Ag deposited directly on the substrate, allowing a very smooth and planar surface similar in smoothness to a layer-by-layer growth mode (Frank-Van der Merwe) [6].

In this thesis we have proposed to use a sputtered 1 nm thick or even thinner Cu seed layer as an effective approach to produce atomically smooth Ag films with thicknesses less than 10 nm and greater electrical conductivity in comparison to monolayer Ag films. Cu was chosen since it is an inexpensive material with excellent electrical and optical properties and is already used widely in microelectronics industry. More importantly, due to its higher surface energy in comparison to Ag and Ge, it acts as a perfect seed layer for the growth of Ag films. Coalescence of Ag films induced by the Cu seed layer lead to the formation of a continuous film with a percolation thickness as low as 3 nm was achieved together with sub-nanometer surface roughness (RMS). Cu seed layer also reduced the RMS roughness of Ag films, measured over a large area, leading to a concomitant reduction factor of two in the electrical resistivity when compared with previous reports on Ge/Ag films [16]. In addition, due to the lower percolation thickness, we were able to reduce the minimum thickness required to obtain

a continuous Ag film down to 3 nm, which is substantially lower than that reported in literature for Ag films, thus paving a way for the deposition of smooth, ultra-thin continuous Ag films. As a result of the improved uniformity, the oxidation of the Ag layer is strongly reduced to negligible values even after 4 months of exposure to ambient atmospheric conditions.

In the following sections, we describe in more details the deposition of the Cu seeded Ag layers, its characterization and discuss the performance results.

3.2.1 Samples fabrication and characterization

The films were fabricated on optically polished 1 mm thick UV grade fused silica substrates using the ATC Orion 8 HV sputtering in an Ar atmosphere. The Cu and Ag layers were deposited sequentially without breaking the deposition chamber vacuum by DC sputter deposition from Cu and Ag targets of 3 inch diameter. The main chamber was typically evacuated to a base pressure below 1×10^{-7} Torr and deposition was performed under the following conditions: DC power 100 W, a pure Ar working pressure of $2x10^{-3}$ Torr and the target - substrate separation was 300 mm. The deposition rates, which are 25.6 Å/s for Ag and 15 Å/s for Cu, were determined using a MCM-160 quartz crystal and cross sectional Scanning Electron Microscopy (SEM) measurements of thick metal layers. Prior to the deposition, the substrates were ultrasonically cleaned with acetone and ethanol for 10 min, dried under flowing nitrogen, heated in oven at 100 ºC for 30 min and finally transferred to the deposition chamber where they underwent a 15 min Ar plasma cleaning treatment at 40 W RF power and a pressure of 8×10^{-3} Torr. The depositions were performed at room temperature (22 ºC) although a marginal increase of temperature (<4ºC) was observed due to the sputtering process.

The electrical resistivity measurements of the deposited films were carried out by a Cascade Microtech 44// S 2749 four-point probe system with a Keithley 2001 multimeter while transmittance and reflectance spectra were measured by a PerkinElmer Lambda 950 UV-Vis-NIR spectrophotometer.

Surface morphology was investigated by a digital instrument D3100 (AFM) and FEI-SEM. The AFM image analysis was carried out with Nanoscope 7.30 software.

High resolution X-ray reflectivity (XRR) and grazing incidence X-ray diffraction (GIXRD) measurements were performed using Cu K-alpha radiation and a Philips MRD goniometer equipped with a four-crystal Bartels Ge 220 monochromator. The Motofit code was used to fit the X-ray reflectivity data for scattering vectors greater than 0.15 $Å^{-1}$, which corresponds to incident angles where the X-ray beam's projection does not spill off the sample. The specular reflectivity is calculated using Parratt`s recursion formula (1954) for stratified thin films, as a function of the perpendicular momentum transfer. The Motofit reflectivity analysis module employs a genetic algorithm to simultaneously fit the real and imaginary parts of the scattering length densities, the film thickness and the interfacial roughness to all layers of a multilayer stack. The code was developed by Nelson [17] and is described in the reference.

3.2.2 Experimental results

Several samples consisting of 6 nm thick Ag films with different seed layers, i.e. Si, Cu and Ti, were prepared under the same deposition conditions on double side polished UV grade fused silica substrates. The substrates had a very low RMS surface roughness; measured to be <5 Å. Figure 3.5 shows the two dimensional AFM images for the following ultra-thin film

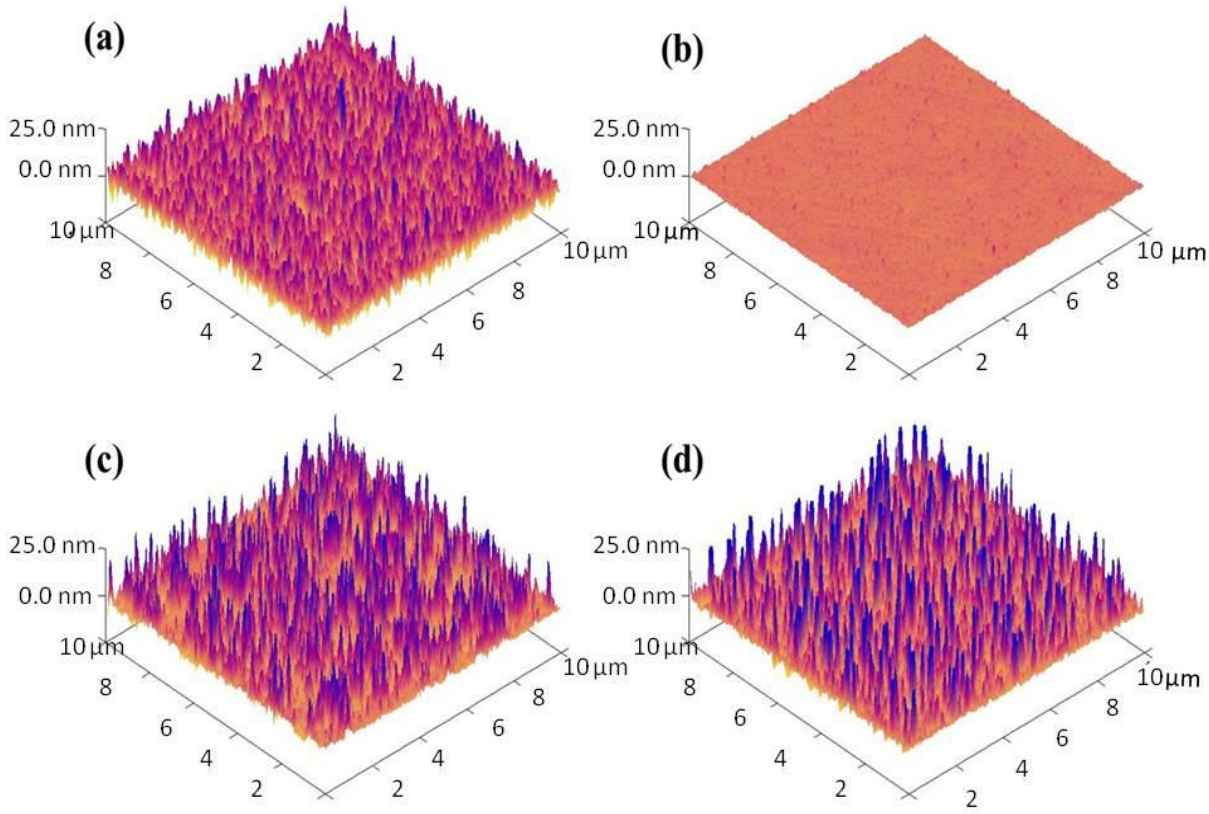

Figure 3.5: *Three dimensional AFM images of* ***(a)*** *6nm Ag,* ***(b)*** *1 nm Cu/6 nm Ag,* ***(c)*** *1 nm Si/6 nm Ag and* ***(d)*** *1 nm Ti/6 nm Ag. The scanning area was 10 µm x 10 µm.*

Table 3.1*: Summary of surface morphology parameters from AFM image analysis. The 3rd column quantifies the percentage increase of surface area of the real surface when compared to a flat surface of the same dimensions. A film with zero image surface area difference represents a perfect sample with zero surface roughness.*

	RMS roughness (nm)	**Peak-to-Valley Roughness (nm)**	**Image Surface area difference (%)**	**Resistivity (10^{-7} Ωm)**
6 nm Ag	4.7	39.5	0.987	2.9
1 nm Cu/6 nm Ag	0.4	7.21	0.0144	0.80
1 nm Si/6 nm Ag	4.4	44.5	0.974	2.79
1 nm Ti/6 nm Ag	5.1	62.9	0.923	2.58

structures: 6 nm Ag, 1 nm Cu/6 nm Ag, 1 nm Si/6 nm Ag and 1 nm Ti/6 nm Ag samples, which respectively had a measured RMS surface roughness of 4.7 nm, 0.4 nm, 4.4 nm, and 5.1 nm over a 10 µm × 10 µm area. As can be seen, the use of Cu as a seed layer lead to

exceptionally smooth Ag films with a RMS roughness less than 0.5 nm, thus reducing the roughness by a factor of 10 and suggesting a layer-by-layer growth mode. Table 3.1 summarizes the different surface morphology parameters for the deposited films. The obtained RMS roughness is much lower than Ge/Ag films (0.6-0.8 nm) reported by Logeeswaran et al. [16]. The 1 nm Cu seed layer forms energetically favourable nucleation sites for the incoming Ag atoms, thus leading to smoother films. The representative surface energies (γ) of Ag, Cu and SiO_2 are about 1.2 - 1.42 Jm^{-2}, 1.96 Jm^{-2} and 0.26 Jm^{-2}, respectively [18, 19]. Due to its relatively high surface energy the Cu seed layer produces a favorable wetting effect for the subsequent Ag growth [20]. Consequently, Ag films grown atop of a Cu seed layer tend to be smoother and exhibit a lower percolation threshold than Ag films grown directly on top of SiO_2, as it is shown in the reported experiments. This phenomenon can also be explained in terms of bond dissociation energies (H, enthalpy) of Ag-Ag and Ag-Cu, which are H_{Ag-Ag} =162.9±2.9 $kJ.mol^{-1}$ and H_{Ag-Cu} =176 $kJ.mol^{-1}$, respectively [21]. The higher Ag-Cu bond energy (as compared to the Ag-Ag bond energy) indicates that the Ag atoms tend to be more tightly bound to the Cu surface than they are to their neighboring Ag atoms, which is a situation that is not prevalent in Ag-SiO_2 interfaces. Hence Ag islands on a Cu layer tend to be smoother than Ag films on SiO_2. The Si and Ti seed layers produced rougher Ag films indicating island growth mode where from a nucleation dot the film grows in three dimensional islands till coalescence is reached. The histograms of surface-height values for 6 nm Ag and 1 nm Cu/6 nm Ag are shown in Figure 3.6.

The Ag film with a 1 nm Cu seed layer has a smoother surface compared with that of a single Ag film; the peak-to-valley height (R_Z) is of only ~7 nm and it has a narrow and symmetric height distribution (Skewness ~ -1.32, Kurtosis ~7.26. Skewness measures the symmetry of surface data about a mean data profile. It is a nondimensional quantity which is typically

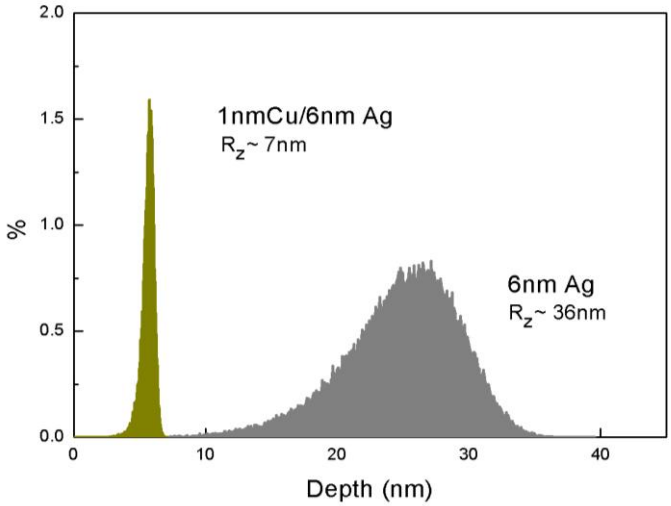

Figure 3.6: *Histogram of the surface-height values for 6 nm Ag and 1 nm Cu/6 nm Ag. The peak-to-valley roughness is also shown for the coatings. The Skewness and Kurtosis corresponding to 6 nm Ag and 1 nm Cu /6 nm Ag films are -1.32, 7.26 and 0.65, 3.69 respectively.*

evaluated in term if positve and negative. Where skewness is zero, an even distribution of data around the mean data plane is suggested. Where skewness is strongly nonzero, an asymmetric, one tailed distribution is suggested. Kurtosis is a nondimesional quantity used to evaluate the shape if data about a central mean. Graphically it indicates whether data are arranged flatly or sharply about the mean). The Ag film without any Cu seed layer is characterized by a more populated and broader distribution (Skewness ~0.65, Kurtosis ~3.69) with a total R_Z difference of ~36 nm. The variation of surface morphology of Ag films with different seed layer thickness was also investigated. It has been observed that the minimum RMS roughness is achieved for a Cu seed layer thickness of 1 nm.

Figure 3.7 shows the RMS roughness as a function of Cu seed layer thickness for a constant Ag thickness of 6 nm. An improvement in the RMS surface roughness from 4.7 nm to 0.7 nm

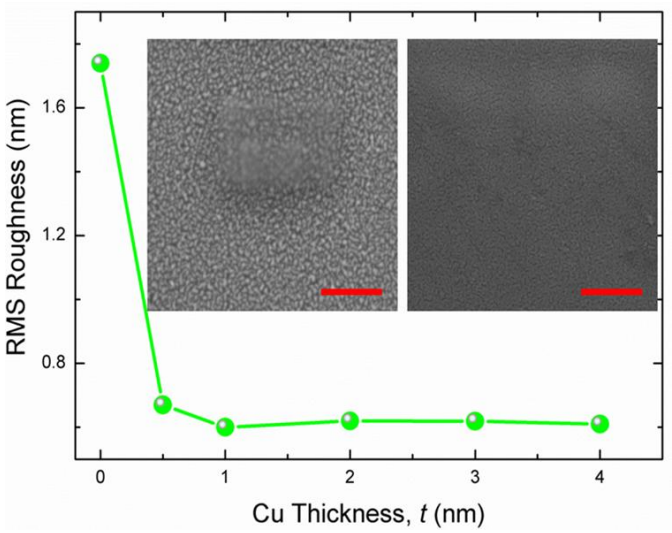

Figure 3.7: *Variation of RMS roughness for 6 nm Ag film with seed layer thickness. For seed layer thicknesses greater than 4 nm the RMS roughness has roughly the same values of about 0.6nm. The inset shows the SEM pictures without (left) and with a Cu seed layer (right). The scale bars are 500 nm.*

was obtained for the first 0.5 nm of Cu deposited. For seed layer thicknesses greater than 1 nm the roughness remains the same at approximately 0.5 nm. The collected SEM surface

micrographs of 6 nm thick Ag films with and without a 1 nm thick Cu layer are depicted in the inset of Figure 3.7.

Without the Cu seed layer, the Ag film consists of metallic islands with an irregular shape and voids while denser and uniform planer morphology is observed in case of Ag film grown on Cu seed layer. The SEM images (inset Figure 3.7) provide further evidence of a discontinuous and coalescent structure together with a rough surface for the Ag film without any seed layer whereas the 1 nm Cu/6 nm Ag film is continuous with a homogeneous surface morphology due to a different growth mechanism altogether. This significant difference demonstrates the potential of the Cu seed layer for fabricating smooth Ag films.

In addition, high resolution X-ray reflectivity (XRR) measurements were acquired in order to confirm the smoothing effect of the Cu seed over a relatively large area. Figure 3.8 shows the

experimental reflectivity curves for 6 nm Ag and 1 nm Cu/6 nm Ag samples. The oscillations in the reflected X-ray intensity showed sharper features, higher modulation, and were more pronounced in reciprocal space for the Cu/Ag structure in comparison with single Ag layer. The reflected X-ray intensity decreases more rapidly in reciprocal space for greater interfacial roughnesses, the interference fringes/oscillations present in the case of Cu/Ag structure clearly indicate much smoother films with lower surface and interface-roughness compared to a single Ag layer. A quantitative measurement of the film interface roughness was obtained by fitting thickness, the real and imaginary scattering length densities and interfacial roughness for all three layers of a slab model using genetic algorithm within the Motofit code [17]. The XRR analysis confirmed that the roughness, over an area of approximately 10 mm × 10 mm, was reduced by a factor of 2 when a Cu seeding layer was used to intermediate the Ag film.

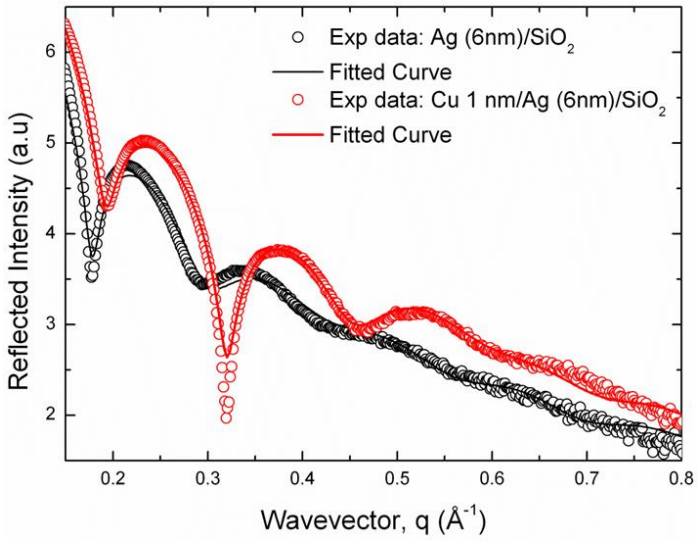

***Figure 3.8**: X-Ray Reflectivity (XRR) spectra for 6 nm Ag and 1nm Cu/6 nm Ag films on silica substrates. The interference fringes/oscillations present in the case of Cu/Ag structure clearly indicates much smoother films with lower surface and interface-roughness.*

Optical reflectance spectra of thin films are indicative of the wetting condition and mode of growth [22, 23]. We investigated the influence of a Cu wetting layer on Ag growth through

the reflectance spectrum in the 300-800 nm range. Figure 3.9 shows the reflectance spectra for Ag films of different thickness with and without Cu seed layer. As can be seen, the films without seed layer are characterized by a different trend with respect to the other set of samples having the additional seed layer. The peaks in the reflectance spectra shift to shorter wavelengths with increasing thickness; observed for films up to 8 nm Ag. This optical behavior is caused by a localized plasmon resonance in the metal particles [24].

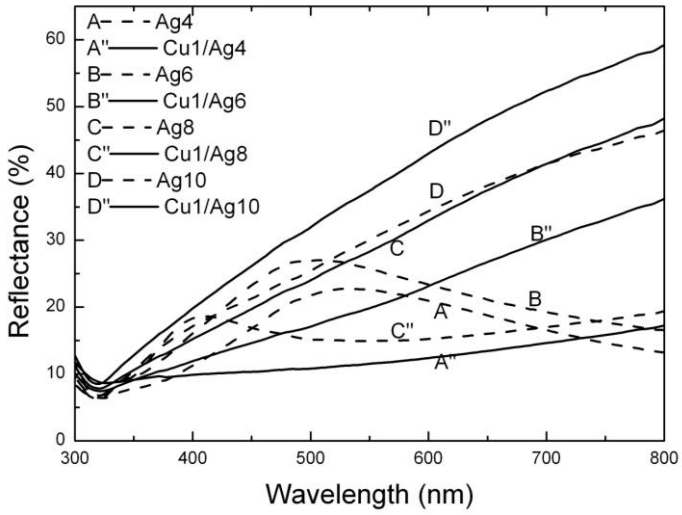

Figure 3.9: *Comparison between the reflectance spectra of ultrathin Ag layers deposited with Cu 1nm layer (continuous lines) and without seed layer (dashed lines). The localized plasmonic resonance behavior is clearly visible in the case films without the seed layer. The reflectance was measured at near-to-normal angle of incidence of about 15^o.*

The localized plasmon resonance in the earlier stages of film growth is induced by collective oscillations of conduction electrons, which are confined within the Ag grains [25]. This plasmon resonant character disappears when the nano-structuring of the Ag film disappears. This difference between the curves is due to changes in the morphology of the metal and indicates a discontinuous and a continuous Ag layer without and with Cu seed layer respectively. From these measurements it emerges that the 4 nm thick Ag film is already continuous on a Cu seed layer, while without the Cu seed layer a continuous film occurs at a higher thickness. Once the optimum seed layer and thickness were determined, thin Ag films

with a nominal thickness between 3 and 10 nm were sputtered with and without a 1 nm thick Cu seed layer. Four point probe electrical measurements, shown in Figure 3.10, reveal that when the thickness of the single layer Ag film reaches a threshold value of 6 nm, a sharp drop in the electrical resistivity by several orders of magnitude can be observed, indicating the coalescence of islands.

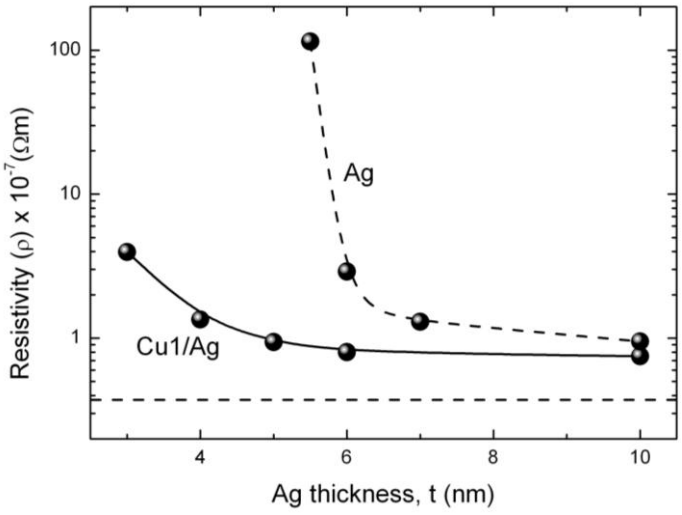

Figure 3.10: *Comparison of electrical resistivity variation for Ag films with and without a Cu seed layer. The dashed line represents the resistivity of bulk Ag film of about 300 nm thickness deposited using the same sputtering process. Both types of films shown here approaches bulk behaviour with thickness > 100nm.*

In contrast, when a 1 nm thick Cu layer is used to aid the coalescence of the Ag film, the increase in electrical conductivity is less pronounced and the threshold thickness is much thinner. The results in Figure 3.10 demonstrate that the Ag film on a Cu seed layer exhibits a lower percolation threshold than a pure Ag film on silica substrates. By employing the Cu seed layer the percolation thickness of Ag films was lowered to about 3-4 nm which is much lower than the 11 nm percolation threshold of e-beam evaporated Ag films on Si/glass substrates reported elsewhere [26]. According to the scattering hypothesis based on the

assumption of Matthiessen's rule, the resistivity (ρ) of a non-ideal metal film can be expressed as:

(3.4) $$\rho = \rho_0 + \rho_{GB} + \rho_{SS} + \rho_{SR}$$

where the contributions of grain-boundary ρ_{GB}, surface scattering ρ_{SS}, and surface roughness ρ_{SR} are added to the bulk resistivity value ρ_0. Finzel and Wissmann [27] extensively studied

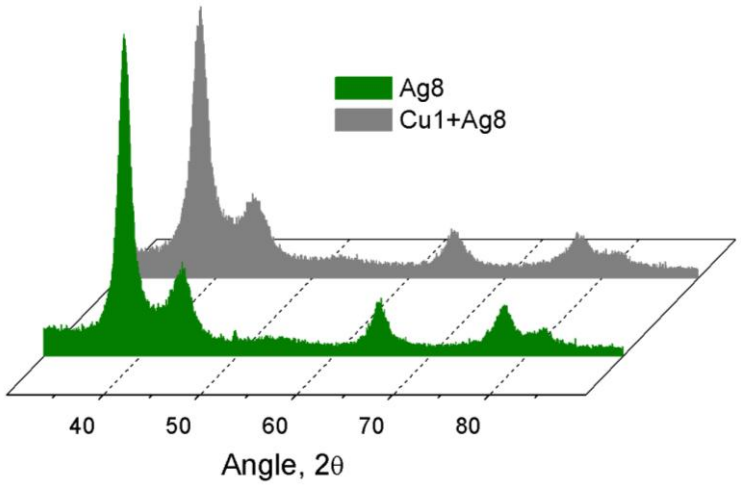

Figure 1.11: *GIXRD spectra of 8 nm Ag films with and without seed layer. The y-axis represents the intensity in arbitrary units. The calculated grain size for the Ag films with seed layer was found to be 1.5 times smaller compared to Ag films without the seed layer.*

the effect of surface roughness on the electrical resistivity of metal films and found that the roughness term in Eqn. (3.4) varies proportional to inverse of third power of film thickness i.e. t^{-3} which implies that the surface roughness plays a major role in UTMFs when $t < l$ where l is the mean free path of the bulk metal. In our case, for example 6 nm Ag and 1 nm Cu/6 nm Ag having roughness 4.7 nm and 0.4 nm, the resistivity of the former was about 3.5 times of the latter.

As evident from the roughness and resistivity values, the decrease in resistivity might also be attributed to improved crystallinity of the Ag film grown on the Cu seed layer. To validate this assumption grazing incidence X-ray diffraction GIXRD was measured for both sets of samples. The average grain size can be deduced by using Scherrer formula: $D=0.9\ \lambda/(B\cos\theta\ B)$ where D is the grain size, B is the full width at half maximum (FWHM), and θ is the Bragg angle. For the samples 6 nm Ag and 1 nm Cu/6 nm Ag the angular FWHMs calculated from the GIXRD experimental curves, shown in Figure 3.11, are 1.5° and 2.248° respectively. Taking into account those values from GIXRD spectra analysis the average grain size of the rough Ag film is 1.5 times larger than for the smooth film. Another advantage associated with the seed layer assisted growth of Ag films is that unlike the pure Ag film the Cu/Ag films offer much more resistance to corrosion in ambient conditions. This is due to the fact that rougher Ag films present larger surface area to the O_2/H_2O present in the atmosphere leading to their oxidation within few hours after their preparation while the smoother Cu/Ag films remain stable even after 4 months of fabrication.

Figure 3.12 shows the picture of 6 nm Ag film with (4 months after the deposition) and without Cu seed layer (24 hours after deposition) stored in air ambient.

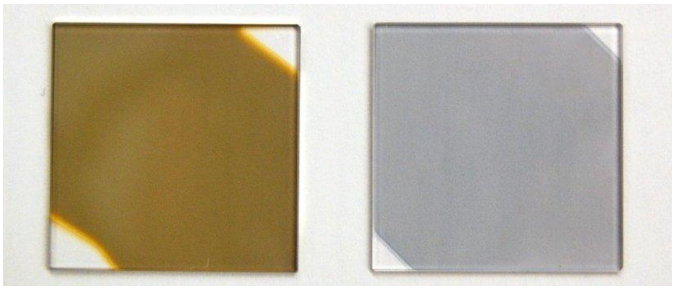

Figure 3.12: *Pictures of 6 nm Ag film without (left) and with seed layer (right) 24 hours and 4 months after deposition respectively. Freshly deposited Ag films without seed layer look exactly the same as the Ag film with seed layer 4 months after deposition as shown in the picture.*

For the pure Ag film, a change of color from grey to reddish-brown together with infinite electrical resistivity clearly indicates the oxidation of the sample. On the contrary, the Cu seeded Ag film showed the same electrical behavior over 4 month's period of time.

3.3 Cu-Ag alloy based Transparent Conductors

Although UTMFs can present a wide transparency spectrum from UV to mid-IR [28], the spectrum within the visible range is non-uniform due to long wavelength reflection associated to electronic plasma formation at a characteristic frequency ($\omega_p = (4\pi n^2 e/m)^{1/2}$) as well as short wavelength absorption due to intraband electronic transitions. The peak transmittance of UTMFs, which also provide sufficiently large electrical conduction, is usually as high as 80% and decreases as one moves from that wavelength. This translates into both a lower average optical transmission as well as a non-uniform wavelength response. One solution to counteract the transmission decrease, associated to reflection above the plasma frequency, is to use antireflection thin film oxides, such as ZnO, ITO, and TiO_2. The resulting multilayer TC structures can present high optical transparency and low sheet electrical resistance [29].

In this section, we show that by combining UTMFs, which present transmission peaks at different wavelengths in the visible region, in an alloy form, one can achieve TCs with a flat wavelength response, still maintaining low Rs values. UTMFs of Ag and Cu show peak transmittance at around 335 nm and 630 nm, respectively (see Figure 3.14). The Ag/Cu (50%/50% composition) alloy presents a transmission spectrum flatter than those of the individual Cu and Ag layers. In addition, since both Ag and Cu UTMFs exhibit very high electrical conductivity, their alloys show low sheet resistance. Among other Ag/Cu compositions we have investigated, such as 75%/25% and 25%/75%, the 50%/50% was the best performing one. When incorporated in devices the alloy films can be further coated with a Ni layer to enhance both their stability and work function as it is demonstrated in Chapters

IV and V. The resulting transparent conductors are exceptionally smooth, truly flexible, and remarkably resistant at elevated temperatures, in addition to a high work function.

3.3.1 Optical spectra predictions

To predict and assess the potential of alloy films as semi-transparent conductors, we analysed the optical behaviour of the alloy films by using the Fresnel′s matrix formalism [30]. Assuming that we have Z layers and $Z-1$ interfaces, in each layer we have an incoming and a reflected wave, x and y respectively, one can then obtain the following equation:

(3.5)
$$\begin{pmatrix} x_1 \\ y_1 \end{pmatrix} = \begin{pmatrix} m_{11} m_{12} \\ m_{21} m_{22} \end{pmatrix} \begin{pmatrix} x_z \\ y_z \end{pmatrix}$$

where m is a matrix related to the Fresnel coefficients ($N=n+ik$). Therefore, if we assume the final reflectance of y_z at the interface of substrate and air media equal to zero, we can obtain the total transmission of the multilayer (Z-layers) structure as:

(3.6)
$$T = \left(\frac{N_z}{N_1}\right) tt^* = \left(\frac{N_z}{N_1}\right)\left(\frac{x_z}{x_1}\right)\left(\frac{x_z}{x_1}\right)^* = \left(\frac{N_z}{N_1}\right)\left(\frac{1}{m_{11}}\right)\left(\frac{1}{m_1}\right)^*$$

The n, k parameters used for transmission calculation of alloy films were average weighted values of the constituent metal films at any wavelength (Eq 3.7, 3.8).

(3.7)
$$n_{Alloy,\lambda} = (n_{1,\lambda} + n_{2,\lambda})/2$$

(3.8)
$$\kappa_{Alloy,\lambda} = (\kappa_{1,\lambda} + \kappa_{2,\lambda})/2$$

where (n_1, κ_1) and (n_2, κ_2,) are the optical constants for the two constituent metals. The n and κ values used for calculation in the work are standard values for bulk material which can be found in literature [31].

Figure 3.13 (a) shows the theoretical prediction of optical transparency for different alloy films of 50%-50% composition in the visible range. For all the curves, 10 nm-thick films were considered. As it can be seen in the figure, Ag-Cu alloy films have the highest and flattest optical transmission among all alloy films and therefore we have chosen them for this study.

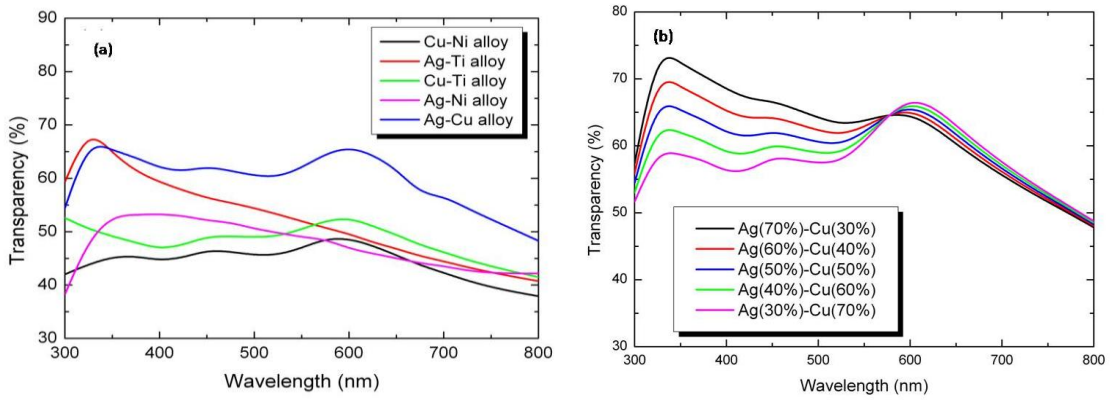

Figure 3.13: *Optical Transparency in the visible spectrum for different* ***a)*** *alloy films with 50 %50% composition for the two constituent metals* ***b)*** *percentage composition of Cu-Ag alloy films.*

We have also calculated the optical response of Cu-Ag alloy films for different percentage compositions. As it can be seen in Figure 3.13 b) the amount of Ag content dominates the optical behaviour of the alloy. When the Ag composition is greater than 50%, the alloy film starts showing higher average transmission in the VIS range.

The approximately 50%-50% composition alloy film shows the flattest optical response among all other compositions considered and remains the subject of our study.

3.3.2 Experimental details

The films were prepared onto 1 mm-thick UV grade optically polished silica substrates by magnetron sputtering in pure argon atmosphere. The substrates were cleaned in acetone and ethanol for 10 minutes each in ultrasonic bath, followed by 15 minutes plasma in-situ

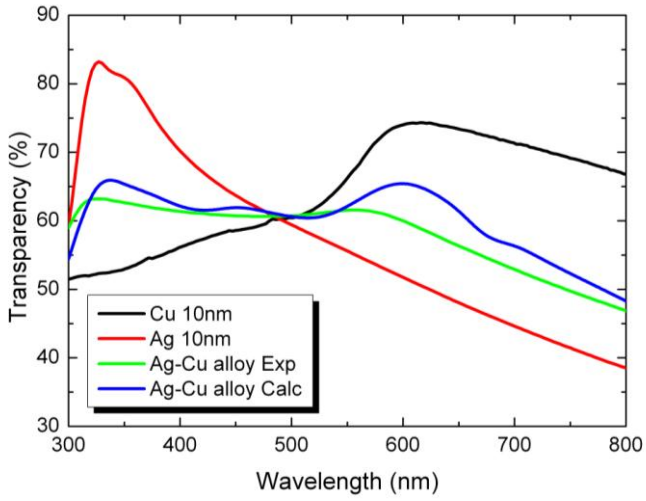

Figure 3.14: *Experimental comparison of optical spectra between Ag-Cu (50%-50%) alloy and single component Ag and Cu metal films. The graph also shows the theoretical optical prediction for the alloy film.*

cleaning in Ar atmosphere inside the sputtering chamber. To prepare alloy films by co-sputtering, deposition rate of pure Cu and Ag targets were calculated and a condition was determined at which both metal show the same deposition rate. The thickness of the alloy films was assumed to be the sum of individual metal thickness when they were sputtered alone. Single component Cu and Ag films were also prepared under the same conditions to compare with the alloy films. Alternatively, alloy films can also be prepared by an alloy target (50%-50% composition of Cu and Ag) rather than co-sputtering. However we have observed target degradation after few depositions due to different depositional rate of the constituent metals of the target. This is why co-sputtering from different single metal targets was preferred.

3.3.3 Optical, morphological and electrical performances

As it can be seen in Figure 3.14, there is good agreement between experimental and theoretical curves for the alloy film, despite the fact that we have considered bulk values for n, k of Cu and Ag, which can be different from the actual values when the thickness of the film is smaller than 10 nm [32]. As it was expected, the alloy film shows a quite flat behaviour compared to single component Cu and Ag films, with the peaks due to Ag and Cu strongly reduced. As it will be shown in chapter VI this makes the alloy films particularly suitable for application-specific devices, such as OSCs.

Generally, alloy films are usually harder and less conductive than their constituent metals [33]. Metals when deposited as single materials show uniform density while alloys can vary their density across the substrate, thus leading to enhanced scattering of conduction electrons, in turn larger electrical resistivity. This is confirmed by the fact that the R_S of the deposited alloy films is slightly larger than those of single component metal films. The R_S of 10 nm alloy film is about 15 Ω/sq while same thicknesses of Cu and Ag films gave 12 Ω/sq and 8 Ω/sq, respectively.

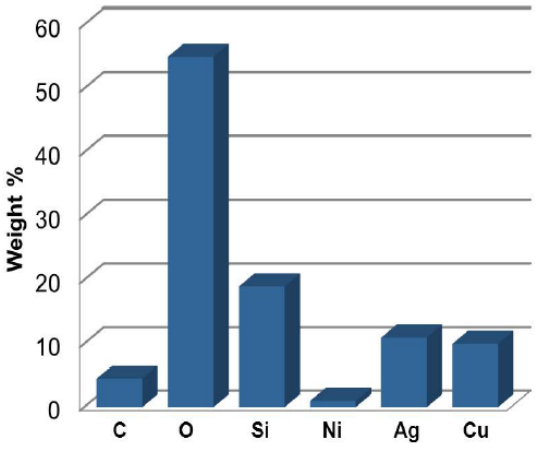

Figure 3.15: *Energy Dispersive X-ray analysis of the Ni 1nm capped alloy films.*

Energy dispersive X-ray spectroscopy (EDX) was also carried out to determine the elemental composition of the deposited alloy films (see figure 3.15). The films, as expected, showed nearly equal composition of Cu and Ag**.**

The AFM analysis of the deposited alloy films and 1 nm Ni capped films reveals RMS values for the roughness lower than 1 nm, which demonstrates an exceptionally smooth surface morphology.

3.4 Uultrathin Al:ZnO/Ag bilayer Transparent Conductor

In this section we propose a novel TC consisting of Ag/AZO deposited at room temperature on glass and PET substrates. The TC combines the high electrical conductivity and mechanical ductility of Ag and the transparency and antireflection of AZO.

The electrical and optical properties of a bilayer structure Ag/AZO were theoretically and experimentally studied with varying Ag thickness. The figure-of-merit (FOM) was also determined for the bilayer structure and the best geometry of the bilayer was also applied to the plastic PET substrates, in order to investigate its mechanical flexibility and compare it with that of ITO.

3.4.1 Implementation

The bilayer structure of AZO capped Ag nano-thick film (Ag/AZO) was prepared onto 1 mm-thick SiO_2 substrates by means of magnetron sputtering. Ag was deposited in pure Ar atmosphere while AZO (aluminum 3 at% doped) was deposited in a mixture of Ar/O_2 (flux ratio 9:1) at room temperature. Deposition rates were determined from the MCM thickness monitor and cross-sectional SEM observation. The deposition of Ag and AZO was carried out in a single run without breaking the vacuum.

3.4.2 Theoretical, experimental results and discussion

In order to obtain the optimal thickness for the AZO capping layer in the bilayer structure, we carried out calculations based on multiple reflection and refraction (MFMR) model [34-35]. According to the MFMR model, the total transparency is closely correlated with interfacial

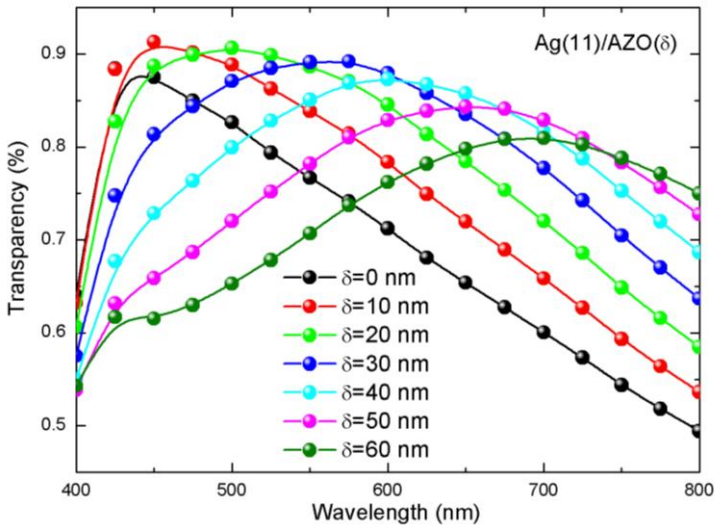

Figure 3.16: *Transparency spectra of Ag(11)/AZO(δ) bilayer structure with different thicknesses (δ) of AZO capping layer, which indicates that the optimal thickness for AZO is in the range of 30nm to 40 nm.*

reflectance and layer thickness. Figure 3.16 shows the calculated optical transparency of the Ag/AZO bilayer structure, in which the thickness of Ag layer is fixed as 11 nm. It is seen that the optical transparency of the Ag layer can be greatly improved by a thin AZO capping layer. The maximum transparency peak shows an apparent red-shift with the thickness variation in the capping AZO layers. It is observed that the optimal thickness for the AZO capping layer is in the range of 30-40 nm, in which the average visible optical transparency exhibits the maximum value. Figure 3.17 a) compares the performance of Ag/AZO bilayer structure alongside ITO (100 nm) (bought from Universitat Stuttgart) which is commercially available. It is observed that the conductivity behavior of the Ag/AZO bilayer structure is mainly dominated by the underlying ultrathin Ag layer when it becomes continuous

(thickness >7 nm). For example, if we take a look at the sample properties of Ag(11) (denoted as the orange point in Figure 3.17 a) and Ag(11)/AZO(30), the sheet resistance for the two samples shows very close values, but for the latter sample, the average visible-optical-

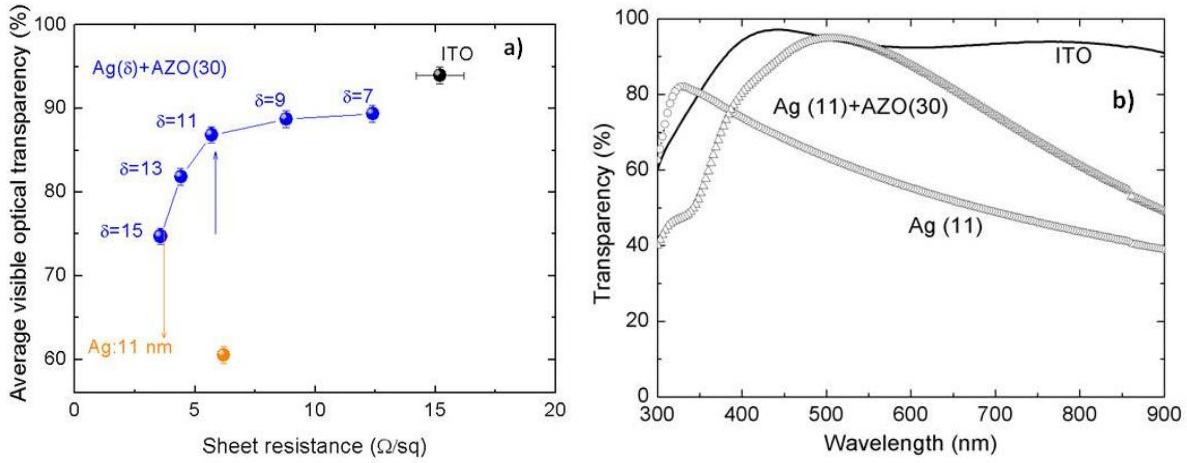

Figure 3.17: a) *Visible optical transparency, averaged over the 375-700 nm range, as a function of sheet resistance for Ag(δ)/AZO(30) and Ag(11). The value of Ag thickness (δ) identifies each point in the curves.* ***b)*** *The spectrum of ITO, is also shown to be compared with the transparency spectra of Ag (11)/AZO(30) and Ag(11) in the visible light region.*

transparency is noticeably enhanced from previously 60.5% to 86.83%. The transparency spectra for Ag (11)/AZO(30) and Ag(11) in the visible light region is shown in Figure 3.17 b). It is seen that the spectrum of Ag (11)/AZO(30) shows a broaden bandwidth and an apparent red-shift with respect to that of Ag(11), which exhibits reasonable consistent with the above theoretical calculation.

The Figure of Merit (FoM) is conventionally used to evaluate the performance of transparent conductors, where the sheet resistance and optical transparency are both considered and evaluated. The ratio of DC conductivity and optical conductivity (σ_{DC}/σ_{OP}) is an effective way to compare the various TCs in terms of their performance and therefore can be used as FoM [36]. The ratio is related to transparency and sheet resistance as $T= (1+(Z_0/2R_S)(\sigma_{DC}/\sigma_{OP}))^{-2}$, where Z_0 is the impedance of the free space and has the value of 376.8 Ω. High values of

σ_{DC}/σ_{OP} implies high transparency and low sheet resistance. We took the average transparency in visible range (375 nm-700 nm) rather than taking it for a particular wavelength for all samples for better evaluation of FoM. For a TC having an average transparency > 90 % and sheet resistance <10 Ω/sq, the value of FoM is ≈ 350, which can be viewed as the benchmark for TC applications.

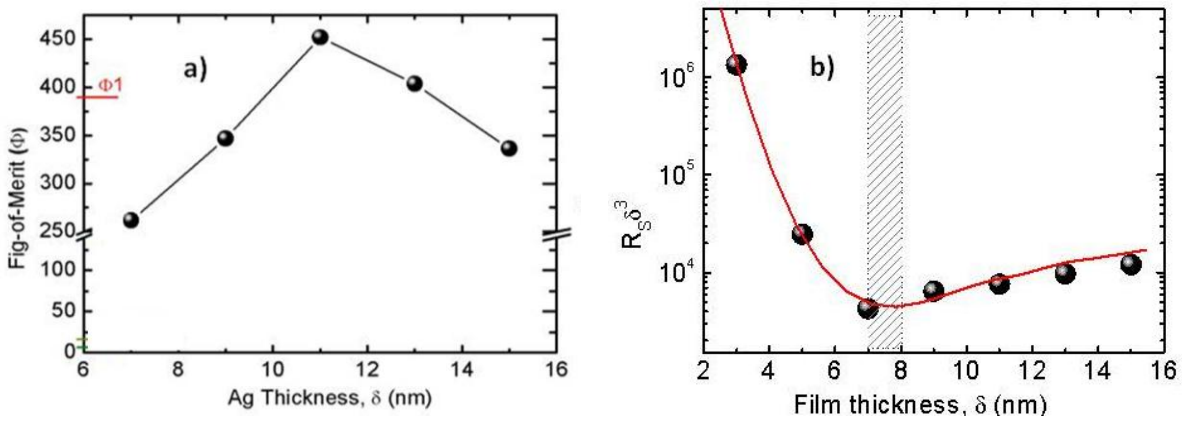

Figure 3.18: a) *Figure-of-merit (FoM, Φ) for Ag(δ)/AZO(30).* ***b)*** *$Rs\delta^3$ versus δ for determination of percolation threshold. Φ_1 identifies the FoM value for commercially available 100 nm ITO.*

Figure 3.18 a) shows the calculated FoM values for Ag/AZO bilayer structure alongside 100 nm ITO film. It is seen that the Ag(11)/AZO(30) exhibits the maximum FoM value of about 450, which is much better than ITO. Guillen et al [37] achieved the highest FoM in a sandwich ITO/Ag/ITO structure by using Ag film thickness of 10 nm, which gives a good agreement with our experimental result. Sahu et al. [38] estimated the coalescence thickness of Ag layers to be around 11 nm, below the threshold, Ag islands were formed rather than a continuous film. As reported in a previous work, the percolation threshold for Ag films, i.e. the thickness corresponding to which the film changes from an island distribution to a continuous layer, was estimated by plotting $R_S\delta^3_{tot}$ versus δ_{tot} (where δ_{tot} stands for the Ag film thickness) [39]. As shown in the Figure 3.18 b, the percolation thickness for the Ag films

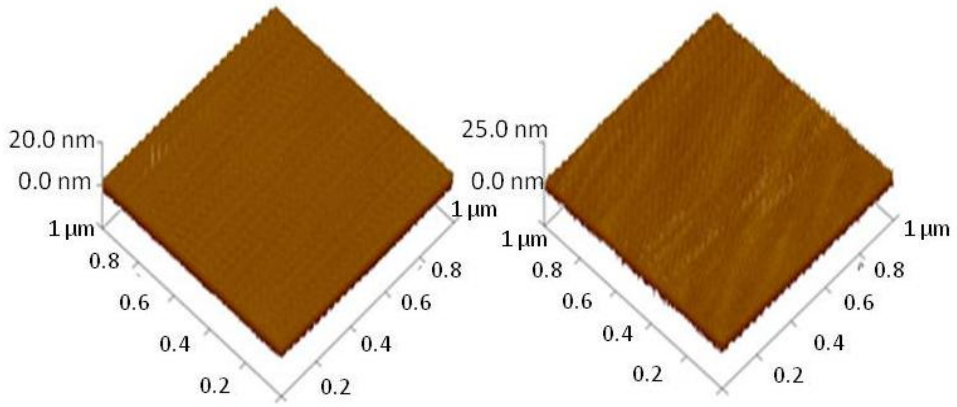

Figure 3.19: *AFM images for Ag(11)/AZO(30) samples on glass (left) and PET (right). The scanning area was 1 µm x 1 µm.*

is found to be in the thickness range of 7 nm to 8 nm. The peak-to-valley value measured by AFM for the Ag samples with a thickness less than 7 nm is higher than the film

thickness, which implies that the films are discontinuous over the microscopic dimension. It is believed that the percolation thickness is related to the growth mode of thin films, in which

the layer-by-layer growth mode favours a small percolation thickness and results in a flat surface morphology. As TC in device application, the transparent conducting layer should have a flat and uniform surface morphology. We characterized the samples prepared on glass and PET with the help of AFM. Ag(11)/AZO(30) samples on glass and PET shows RMS roughness of 2.47 nm and 2.68 nm respectively over an area of 1 µm square (Figure 3.19), which evidences the flatness and uniformity of the surface.

References

[1] S. Cheylan, D. S. Ghosh, T. L. Chen, D. Krautz, V. Pruneri, Organic Electronics 12, 818, 2011.

[2] M. G. Helander, Z. B. Wang, M. T. Greiner, Z. W. Liu, J. Qiu, Z. H. Lu, Advanced Materials 22, 2037, 2010.

[3] H. M. Stec, R. J. Williams, T. S. Jones, R. A. Hatton, Advanced Materials 21, 1709, 2011.

[4] D. S. Ghosh, R. Betancur, T. L. Chen, V. Pruneri, J. Martorell, Solar Energy Materials and Solar cells 95, 1228,2011.

[5] C.G. Granqvist, Solar Energy Materials and Solar Cells 91, 1529, 2007.

[6] O. Inganas, Nature Photonics 5,201, 2011.

[7] D.S. Ghosh, L. Martinez, S. Giurgola, P. Vergani, V. Pruneri, Optics Letters 34, 325, 2009.

[8] K. Sivaramakrishnan, T.L. Alford, Applied Physics Letters 96, 201109, 2010.

[9] www.ajaint.com

[10] N. Marechal, E. Quesnel, Y. J. Pauleau, Vac. Sci. Technol. A 12, 707, 1995.

[11] H. C. Kim, N. D. Theodore, T. L. J. Alford, Appl. Phys. 95, 5180, 2004.

[12] M. S. Islam, Chang Liz., D. A. A. Ohlberg, D. R. Stewart, S. Y. Wang, R. S. Williams, In Proceedings the th IEEE Conference on Nanotechnology; IEEE: Nagoya, Japan, 80, 83, 2005.

[13] P. Nagpal, N. C. Lindquist, S. H. Oh, D. J. Norris, Science 325, 594, 2009.

[14] K. Fukuda, S. H. N. Lim, A. Anders, Thin Solid Films 516, 4546, 2008.

[15] A. Anders, E. Byon, D. H. Kim, K. Fukuda, S. H. N. Lim, Solid State Commun. 140, 225, 2006.

[16] V. J. Logeeswaran, N. P. Kobayashi, M. S. Islam, W. Wu, P. Chaturvedi, N. Fang, S. Y. Wang, R. S. Williams, Nano Lett. 9, 178, 2009 .

[17] A. J. Nelson, Appl. Crystallogr. 39, 273, 2006.

[18] K. J. Kendall, Phys. D: Appl. Phys. 23, 1329, 1990.

[19] R. J. J. Jaccodine, Electrochem. Soc. 110, 524, 1963.

[20] J. N. Israelachvili, Intermolecular and Surface Forces; Academic Press: London, pp 196, 275, 280, 415, 1992.

[21] D. R. Lide, In C.R.C Handbook of Chemistry and Physics, 87th ed.; CRC Press: Devon U.K, 2007; p. 9−54.

[22] O. S. Heavens, Rep. Prog. Phys. 23, 1960.

[23] P. Taneja, P. Ayub, R. Chandra, Phys. Rev. B 65, 245412, 2002.

[24] J. Bulíř, M.Novotný, A. Lynnykova, J. J. Lančok, Nanophotonics 5, 1, 2011.

[25] U. Kreibig, M.Vollmer, Optical Properties of Metal Clusters; Springer Series in Material Sciences; Springer-Verlag: Berlin, 1995; p 25.

[26] P. Nyga, V. P. Drachev, M. D. Thoreson, V. M. Shalaev, Appl. Phys. B: Laser Opt. 93, 59, 2008.

[27] P. W. Hans, U. Finzel, Electrical Resistivity of Thin Metal Films; Springer Tracts in Modern Physics; Springer-Verlag: Berlin, 2007; p 223.

[28] D. S. Ghosh, L. Martinez, S. Giurgola, P. Vergani and V. Pruneri, Optics Letters 34, 325 2009

[29] J. Lewis, S. Grego, B. Chalamala, E. Vick, D. Temple, Applied Physics Letters 85, 3450, 2004.

[30] O. S. Heavens, Reports on Progress in Physics 23, 1, 1960.

[31] E.D. Palik, Handbook of Optical Constant of Solids, Academic Press, 1998.

[32] S . Giurgola, P. Vergani, V. Pruneri, Nuovo Cimento B121, 2006 887, 2006.

[33] L. W. Barron, J. Neidrich, S.K. Kurinec, Thin Solid Films 515, 3363, 2007.

[34] O. S. Heavens, Optical properties of thin films, Reports on Progress on Physics 23, 1, 1960.

[35] H. Hirayama, K. Kaneda, H. Yamashita, Y. Monden, The Visual Computer 17, 106, 2001.

[36] G. Haacke, Journal of Applied Physics 47, 4086, 1976.

[37] C. Guillen, J. Herrero,Solar Energy Materials and Solar Cells 92, 938, 2008.

[38] D. R. Sahu, S. Y. Lin, J. Y. Huang, Solar Energy Materials and Solar Cells 91, 851, 2007.

[39] A. I. Maaroof, B. L. Evans, Journal of Applied Physics 76, 1047, 1994.

CHAPTER IV

Stability of ultrathin metal and AZO based Transparent Conductors

Due to their metallic nature, ultrathin metal films (UTMFs) can easily degrade through oxidation when exposed to environmental agents such as air and moisture, especially at elevated temperature. This can occur also during fabrication processes, such as wet etching and deposition of other materials (oxides) containing reactive elements (oxygen). As a consequence of chemical and morphological changes, the electrical and optical properties of UTMFs worsen. In particular this is the case of Ag, Cu, Al, and to a less extent of Cr, Ni, and Ti. It is also widely known that AZO thin films tend to degrade at elevated temperature in the presence of humidity, the effect being correlated with hydrolysis-induced corrosion process at the grain boundaries [1-3]. It is thus crucial to design and develop new TC structures with increased stability.

In this chapter we investigate the thermal and environmental stability of UTMFs and AZO based TCs and propose different solutions to overcome instability, by capping with UTMFs, oxidized UTMFs or graphene to protect the underlined sensitive layer, in particular Ag, Cu and AZO.

4.1 Cu–Ag alloy capped with Ni transparent conductors

It has already been demonstrated that UTMFs themselves can be protected though oxidation. Stable films are achieved by an appropriate temperature cycle in presence of oxygen which produces a protective oxide layer on top of the metallic film preventing further oxidation [4]. Inspired by this, in the thesis we propose simple and effective approaches in order to obtain stable UTMF based TCs. A more specific structure consists in a Cu-Ag alloy layer capped with

an ultrathin (1nm) Ni layer. Such alloy film had been introduced as TC in **Chapter III** and here we investigate its thermal stability and the improvements associated to Ni capping. Ni is chosen as capping metal layer since it has high resistance to oxidation and high work function, the latter being a crucial aspect for many devices, including OLEDs and OSCs [5]. We extensively optimized the magnetron sputtering deposition parameters including power, pressure and target-substrate distance to achieve a continuous 1 nm Ni film. The AFM images of Ni 1nm (figure 4.1) show a planar morphology which confirms the continuity of the film. In addition, we were also able to measure a sheet resistance (R_s) of about 3 kΩ/sq by Four Point probe and Van der Pau methods, in agreement with the fact that the films are electrically continuous.

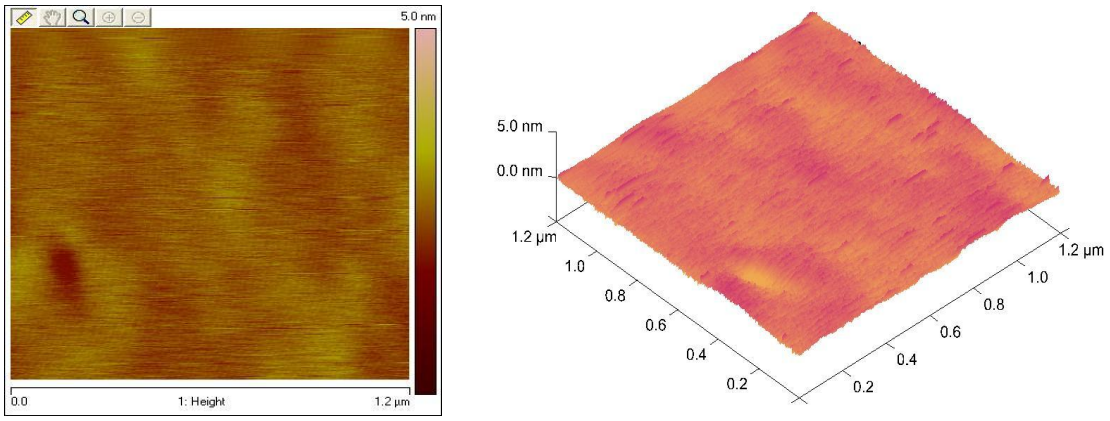

Figure 4.1: *2D and 3D AFM images of 1nm Ni capping layer. The planar morphology with low RMS confirms the continuity of the film. The scanned size area is 1.2 µm x 1.2 µm.*

Two sets of samples consisting of Cu-Ag alloy with and without 1nm Ni capping layer were deposited and tested at high temperature, in the presence of atmospheric oxygen.

The films were kept in ambient air for a dwell time of 45 min at temperatures (*T*) as high as 200 °C and the corresponding R_s was measured after each thermal cycle once the sample was cooled down to room temperature.

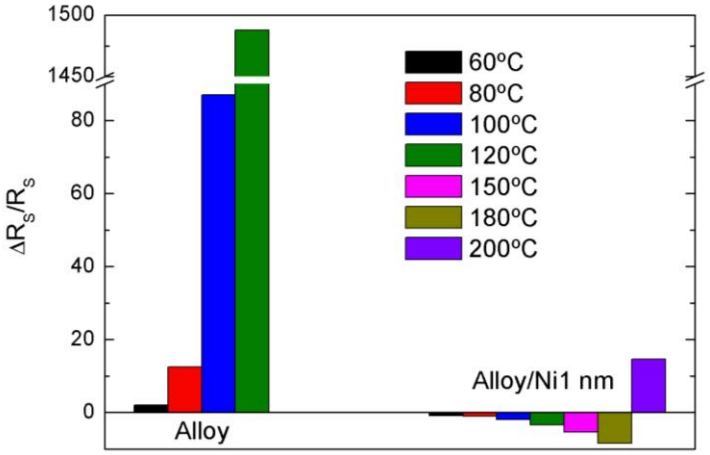

Figure 4.2: *Stability of both the alloy and 1nm Ni capped alloy film upon temperature treatments.* $\Delta R_s/R_s$ *represents the electrical sheet resistance variation.*

Figure 4.2 shows the variation of R_s with different temperatures cycles. The pure alloy film started degrading in performance at 60 °C due to oxidation while the 1 nm Ni capped alloy film improved its electrical and optical properties up to elevated temperatures of about 180 °C. The AFM analysis of the deposited alloy films and 1 nm-Ni capped films reveals RMS roughness values lower than 1 nm, which demonstrates an exceptionally smooth surface morphology (Figure 4.3 top and bottom). The stability of the Ni capped alloy film can be explained in terms of formation of self-induced thin oxide layer formed at its surface when exposed to air [4]. This oxide layer mainly composed of NiO_x prevents the underneath remaining metal from further oxidation and thereby protects it. On the other hand, the process of oxidation in the case of alloy film without any capping layer occurs much faster and in an uncontrolled way leading to the

degradation of the film. The changes due to oxidation are enhanced by the temperature and are irreversible. A typical ITO film does not show any such degradation at elevated temperature being itself deposited at temperatures higher than 250 °C.

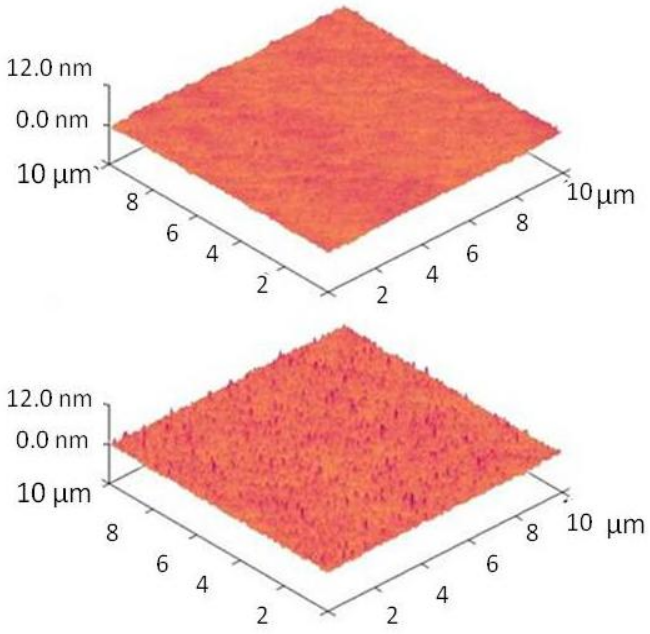

Figure 4.3: *Three-dimensional AFM image of the Cu-Ag alloy film. The RMS roughness of the film was found to be 0.52 nm which is similar to single component Cu and Ag films (top) and the RMS roughness increases to 0.87 nm after coating with 1 nm Ni capping layer (bottom).*

In conclusion, an ultrathin Ni capping layer enhances the stability of Cu-Ag based TCs against temperature in ambient atmosphere maintaining unchanged its electrical and morphological characteristics, in particular the Ni capped alloy film exhibits excellent thermal stability up to > 180 ºC.

4.2 Stability of Ag/AZO based TCs

Transparent conducting non-doped thin films consisting of ZnO, as well as AZO and GZO exhibit a lower stability than those of In_2O_3 and ITO: they increase their electrical resistivity in

oxidizing environments at a high temperature and they can be subjected to chemical modifications on the surface, that increase etching rates in acid and alkaline solutions [6,7].

In particular, the thermal stability of AZO films is known to depend on the deposition conditions of the films [8,9].

Post annealing treatments in various atmospheres, such as oxygen, air, nitrogen, and hydrogen on doped ZnO film have been carried out by various groups to modify intrinsic defects and change its electrical and optical properties [10-12]. As found by Lin et al. [11] and Ahn et al. [12] annealing of AZO films under oxygen or nitrogen cause a considerable reduction in conductivity due to the chemisorption of N_2 or O_2, that are trapped at grain boundaries and form AlN_x or AlO_x. This reduces both the density of donor-like defects and the Al interstitial atoms, resulting in a decrease of carrier concentration [10]. Moreover, the adsorbed species present at grain boundaries increase the barrier potential, which can lead to a trapping of carriers, thereby additionally reducing the carrier mobility. In the case of annealing under hydrogen atmosphere, however, the conductivity of AZO films increases, due to both increased mobility and concentration of carriers. This is attributed to the desorption of adsorbed oxygen from the grain boundaries. First, this desorption lowers the barrier potential, thus increasing the mobility of carriers. Additionally it activates inactive Al ions, thus leading a production of additional oxygen vacancies accompanied by an increased carrier concentration.

Moreover, several groups have reported that even the optical band-gap energies varied depending on the annealing conditions [14-16]. This variation was attributed to Burstein–Moss effect, caused by a shift of the Fermi level in the conduction band due to the modified carrier concentration and consistent with the changes in electrical properties.

As found by J. F. Chang and coworkers, annealing of AZO films in air increases grain size and crystallinity, resulting in lower grain boundary scattering. However, similarly to annealing in oxygen atmosphere, it causes the oxygen to diffuse into the film, eliminating oxygen vacancies, thus reducing carrier concentration [17]. With regard to the environmental degradation, long-term stability tests performed with AZO films in high-humidity environment (relative humidity of 90% and a temperature of 60 °C) for 1000 h, have demonstrated that the resistivity of doped ZnO thin films with a thickness below approximately 50 nm increased when exposed to only air at room temperature (without humidity), while thicker (>50nm) films were clearly electrically more stable. The advantage of thick films with relatively large grain is that they can form dense surface and compact structure that delay corrosion due to oxygen and water molecules [18].

During the thesis, the stability of TCs based on Ag(δ)/AZO(30) (δ is the Ag thickness) described in **Chapter III**, was evaluated, using either furnace annealing at elevated temperature (500 °C) or a humidity chamber, Vötsch VCL 7003 for a 7-day Damp Heat (DH) test at standard conditions (85 °C and 85% relative humidity).

In Figure 4.4 it is clearly observed that the annealing process can lead to slight improvement in both electrical and optical properties, which can be explained in terms of crystallinity and microstructure enhancement with increasing temperature [19]. It is found that R_s improvement shows saturation above about 300 °C, as it is evident for the Ag(11)/AZO(30) sample (Figure 4.4 inset).

The standard DH test results show stability of the annealed TC structures over a relative short (less than one week) period. The samples in DH were measured every 24 h. The stability can be evaluated by the relative slope variation in sheet resistance as follows:

(4.1) $$\tan\theta = \frac{\left|R_s(T-\Delta T) - R_s(T)\right|}{\Delta T}$$

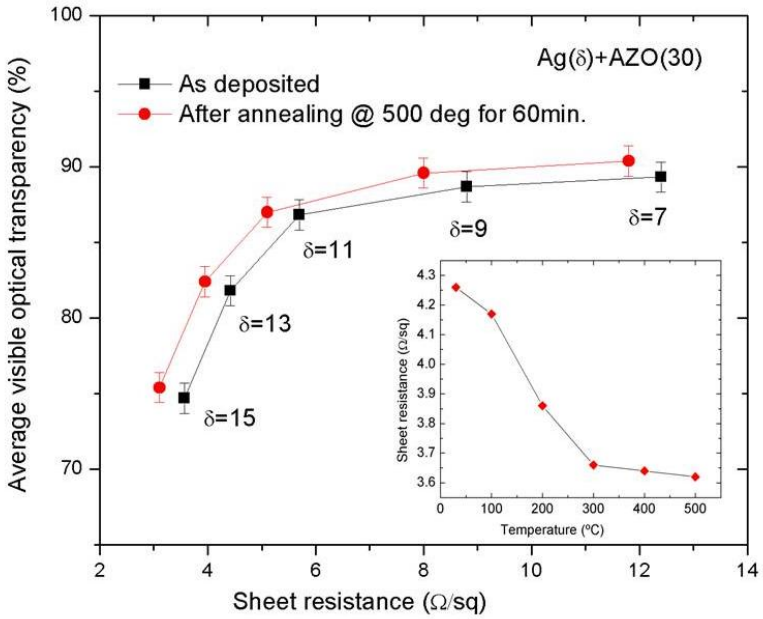

Figure 4.4: *Opto-electrical improvement of Ag(δ)/AZO(30) samples after furnace annealing at an elevated temperature of 500 °C for a dwelling time of 60 min. The inset shows the sheet resistance evolution with the furnace annealing.*

By polar plotting θ versus T (temperature), as it is showing in Figue 4.5, the stability can be readily identified by the relative position in the figure. The ideal stability corresponds to the horizontal axis $\theta = 0$ which implies R_s essentially independent of temperature. From the figure one can readily assess a high stability of the annealed Ag(11)/AZO(30) sample over 1 week. After this period, the sample's surface morphology deteriorates, spots with random distribution appear, especially at the edges. This is due to the penetration of water vapor at elevated temperatures, since it is well known that the pure Ag ultrathin films are very sensitive to atmosphere, and even degrade rapidly when just exposed to ambient atmosphere.

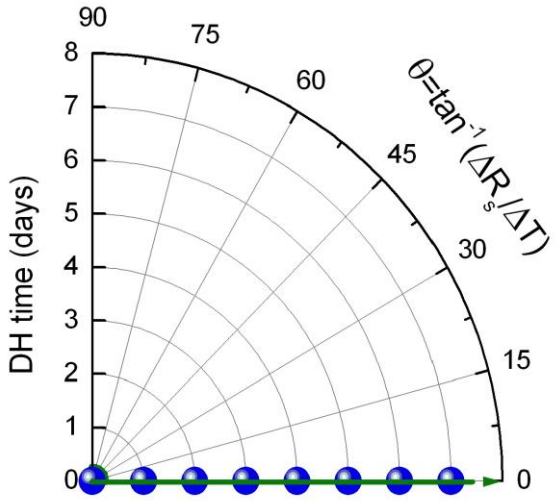

Figure 4.5: *Polar graph of electrical sheet resistance change in standard DH conditions for the Ag(11)/AZO(30) sample.*

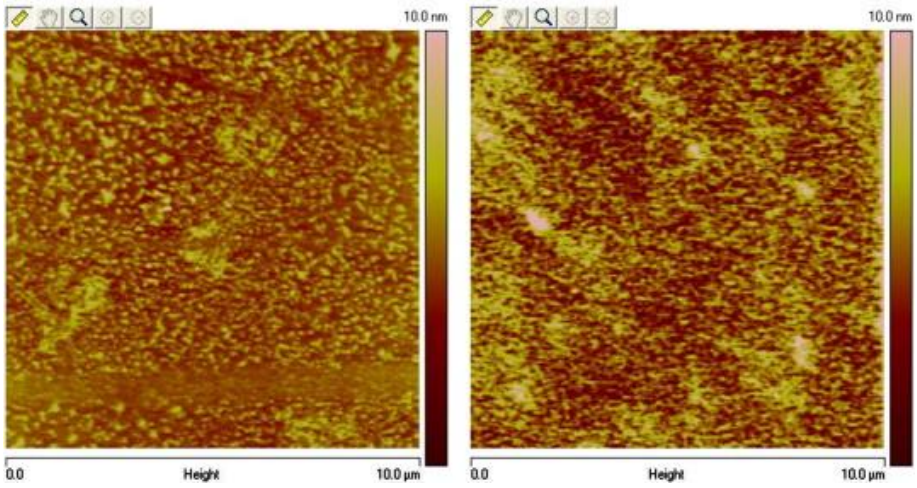

Figure 4.6: *Two-dimensional AFM images of Ag(11)/AZO(30) samples on glass (left) and PET (right).*

As for device applications, the TC layer should have a flat and uniform surface morphology. We characterized the samples prepared on glass and PET using AFM. Ag(11)/AZO(30) samples on

both substrates, glass and PET, show an RMS roughness of 2.47 and 2.68 nm, respectively, over an area of 10 μm^2 (Figure 4.6).

One can conclude that the Ag(11)/AZO(30) TC structure is stable against elevated temperature (500 °C) and can withstand one week DH (85 °C and 85% relative humidity), before starting degradation.

4.3 Ultrathin oxidized Ti capping layer for highly stable AZO based Transparent Conductors

The degradation of AZO films during annealing or when exposed to air ambient, as described before, restricts the use of these films for solar cells. Up to now the majority of the research has focussed on the control of the composition and crystallinity in order to improve the AZO stability.

In this thesis we investigate the use of barrier layers placed on top of the AZO film to prevent its instability. In particular we demonstrate that an ultrathin (5 nm) oxidized Ti capping layer on AZO (AZO/TiO_x) can improve the thermal, environmental stability and surface morphology of the underlying AZO.

AZO films were deposited on UV fused silica substrates by RF magnetron sputtering from a 98 wt. % ZnO and 2wt. % Al target in a pure Ar atmosphere at 1.5 mTorr, 150 W RF power while maintaining the substrate at 200 °C.

The 5 nm Ti layer was deposited at room temperature using RF magnetron sputtering (50 W RF power and 1.5 mTorr base pressure) from a target with a purity level of 99.99%.

Without breaking the vacuum, the subsequent oxidation of Ti was obtained by Oxygen plasma treatment in the same sputtering chamber at 8 mTorr and 40 W DC power for 15 min.

We first optimized the deposition conditions of the AZO film to achieve the lowest electrical sheet resistance for a given optical transmittance. Figure 4.7 shows in the 300–800 nm wavelength range the optical transmittance spectra of AZO and AZO/TiO_x films compared with a commercial ITO-coated glass substrate, which has an average visible optical transmittance (T_{vis}) of about 86% and an electrical sheet resistance (R_s) of 21 Ω/sq. AZO and AZO/TiO_x films have a T_{vis} of 85% and 82%, respectively, and both R_s of about 20 Ω/sq.

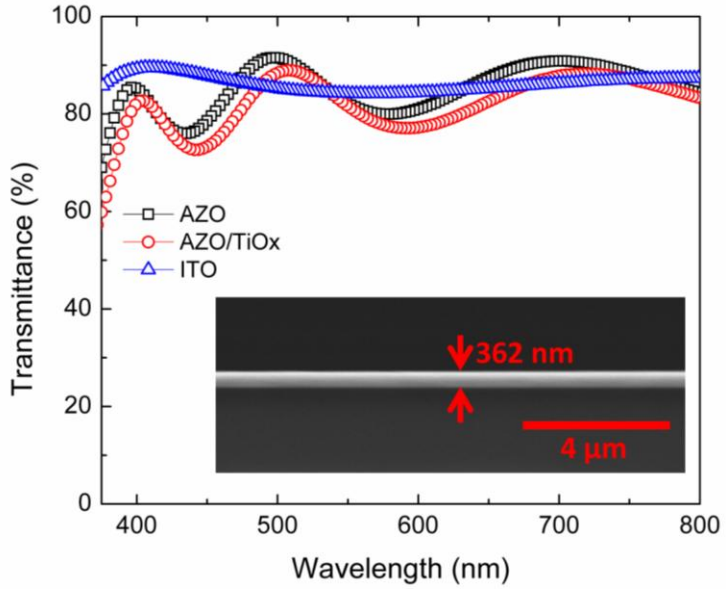

Figure 4.7: *Optical transmittance spectra of AZO, AZO/TiO_x and ITO films in the visible range. The average transmission (T_{vis}) values are 85%, 82%, and 86%, respectively. The inset is the cross section SEM image of the AZO film showing a thickness of 362 nm. The sheet resistance of 100 nm ITO is 21 Ω/sq while those of AZO and AZO/TiO_x films are both 20 Ω/sq.*

Note that capping AZO with an oxidized Ti layer does not change significantly the R_s of the TC. The transmittance in the near-infrared region is reduced due to the absorption of free carriers, and the oscillations are associated to Fabry-Perot interference effects. The SEM cross section

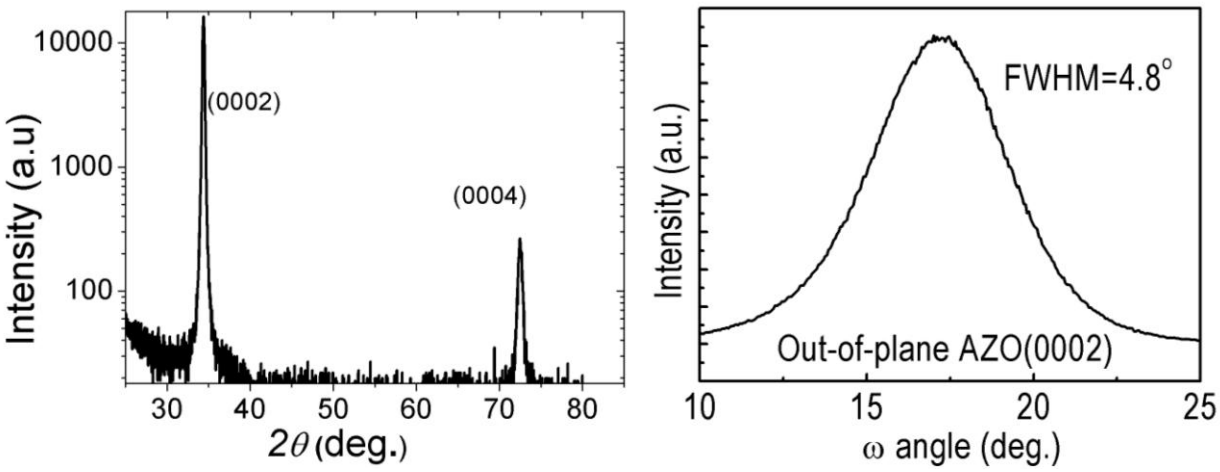

Figure 4.8: *(left) X ray diffraction pattern for AZO grown on glass, (right) w scan for the AZO 0002 peak*.

micrograph included as inset in Figure 4.7 shows a 362 nm thick AZO film deposited on the silica substrate.

The textured structure of the AZO film deposited plays a decisive role in enhancing its environmental stability. Figure 4.8 shows a polycrystalline structure for the AZO film grown on glass with a preferred 0002 orientation. The full width at half maximum (FWHM) for AZO 0002 is 0.34°. The degree of out-of-plane alignment is evaluated by a w scan-rocking curve for the AZO 0002 peak, the FWHM for it being 4.8°. In order to obtain a rocking curve scan, one first performs a θ-2θ scan. Note that this w scan-rocking can be carried out in either symmetric, asymmetric or skew-symmetric geometry. In the next step, the angle θ, and the detector position 2θ, is fixed at the Bragg angle of the corresponding reflection. A rocking curve scan is then

acquired by varying the orientation of the sample by an angle Δω around its equilibrium position, while keeping the detector position fixed.

There are already some reports on the combination of UTMFs and TCOs as TCs. Recently, Bernede et al. deposited a very thin metal layer (0.5–1.5 nm), preferably 0.5 nm, on the top of TCOs to improve their functionality [20].

It was found that the insertion of a UTMF between the TCO anode and the organic layer improves the solar cell performance because of a greater carrier injection and better energy levels matching. On one hand, capping the TCO with such thin metal layers, which tend to have a discrete island-like morphology, results in an incomplete protection of the underlying AZO against the environment or detrimental interaction with other layers forming the device. On the other hand, a thick metal layer reduces significantly the optical transmission. Therefore, there exists an optimum thickness of the metal capping layer corresponding to which the layer morphology changes from an island distribution to a continuous layer (percolation threshold).

Previous work [21] has demonstrated that the percolation thickness of titanium is in the range 2.7 nm–3.1 nm. We opted to use 5 nm thick sputtered Ti layer which is continuous, covering completely the AZO surface, thus ensuring chemical and environmental stability. Since this thickness reduces the transmittance of AZO by about 20%, in-situ oxygen plasma treatment was carried out to reduce absorption and, most importantly, produce an antireflective oxide (TiO_x) on the top of the Ti layer. In such a way the optical transmission is almost fully recovered and brought back to the AZO values. The surface topography of the 5 nm Ti sputtered directly on the glass substrate (Figure 4.9 (a)) together with the line profile (Figure 4.9 (b)) reveals a uniform and continuous smooth film with a Root Mean Square (RMS) roughness of 0.67 nm.

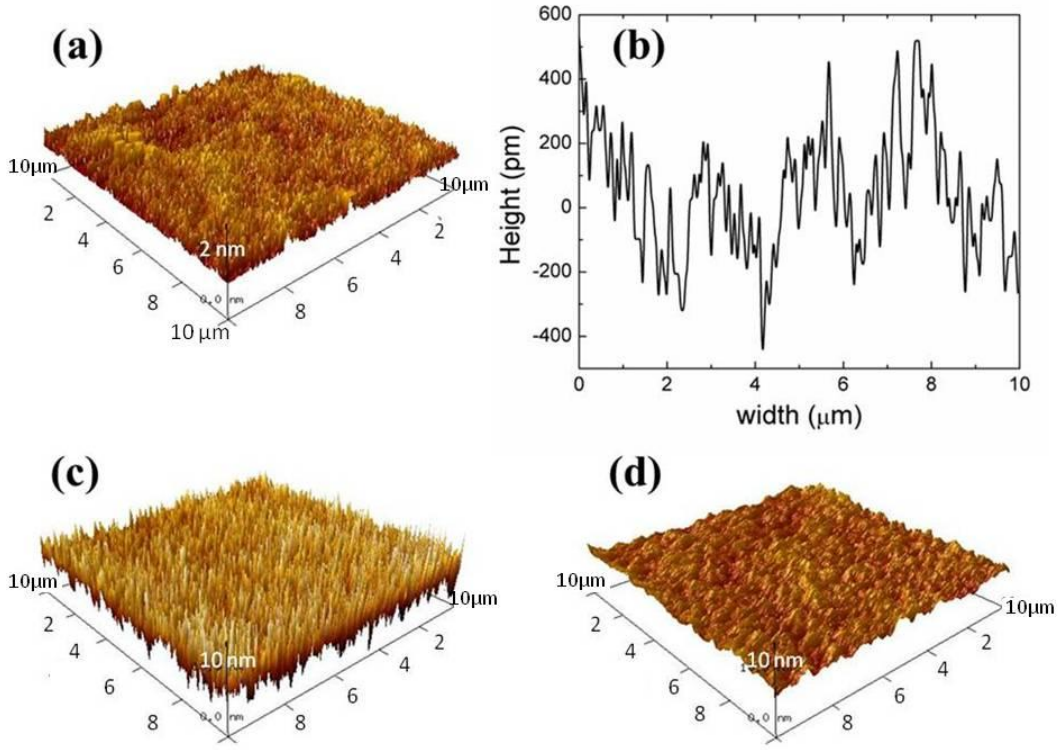

Figure 4.9: *Three dimensional AFM image of* ***(a)*** *5nm Ti film deposited UV fused silica substrate and* ***(b)*** *its corresponding line profile* ***(c)*** *AZO and* ***(d)*** *AZO/TiO_x films. The vertical scale is 2 nm for (a) and 10 nm for (c) and (d).The scanned size area is 10 µm x 10 µm.*

When deposited on the AZO layer the Ti had the very important effect to smoothen its surface (Figure 4.9 (c) and 4.9 (d)), reducing the roughness of a factor of 3, from 2.33 nm (AZO only) to 0.78 nm (AZO with oxidized Ti) RMS values. Such smoothening effect increases the quality of subsequent layers grown on the TE and reduces fringe fields, preventing leakage current and formation of morphological defects [22].

It is well known that Ti oxide (titania) has a substantial oxygen/water protection and scavenging effect originating from the combination of photocatalysis and inherent oxygen deficiency [23]. To explore these effects, AZO films with and without a TiO_x layer were made and underwent

subsequent thermal treatments, each 45 min long, in ambient atmosphere in the 30–400 ºC temperature range.

By capping the AZO film with the oxidized Ti layer, the resulting structure becomes more stable. It can be seen in Figure 4.10 that the electrical properties of both samples remain practically unchanged as temperature varies from 30 ºC to 300 ºC. However, when temperature increases from 300 °C to 400 °C, the R_s of the AZO sample increases whereas the change is negligible for the AZO capped with oxidised Ti sample. This indicates that the TiO_x capping prevents effectively the oxidation of the AZO film at high temperature and improves its properties. In addition, T_{vis} of AZO decreases while that of capped AZO increases during the thermal annealing process, most likely due to further oxidation and associated increase of antireflection effect (inset Figure 4.10).

DH tests were carried out for more than one month at 85 ºC and 85% relative humidity to demonstrate the higher stability of the AZO/TiO_x based electrode compared to AZO. It was found that the oxidized ultrathin Ti greatly stabilizes the electrical as well as optical properties of AZO, also under these severe conditions. As it is shown in Figure 4.11, a large increase in Rs after 500 h was observed for AZO while for AZO/TiO_x the degradation remains negligible up to 1000 h. The DH treatment had no strong effect even on the optical properties of these films. The morphological degradation of AZO is likely to be intimately correlated with hydrolysis-induced corrosion processes that may have occurred at the grain boundaries. However, the use of the TiO_x interlayer reduces the sensitivity to oxygen and water vapor and hinders their intrusion into the active polymers.

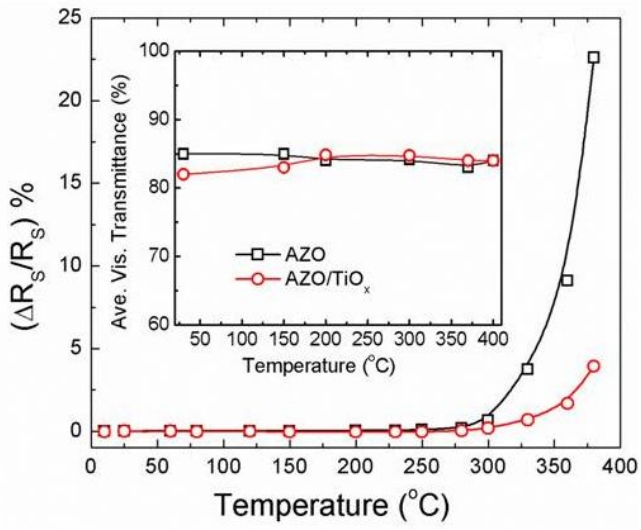

Figure 4.10: *Electrical sheet reistance as a function of temperature for AZO films without and with 5 nm oxidized Ti capping layer. The inset is the average visible transmittance as a function of temperature.*

One can conclude that an ultrathin (~5 nm) oxidized Ti film can considerably improve the stability in ambient atmosphere and harsh environmental conditions of the underlying AZO as well as its surface morphology.

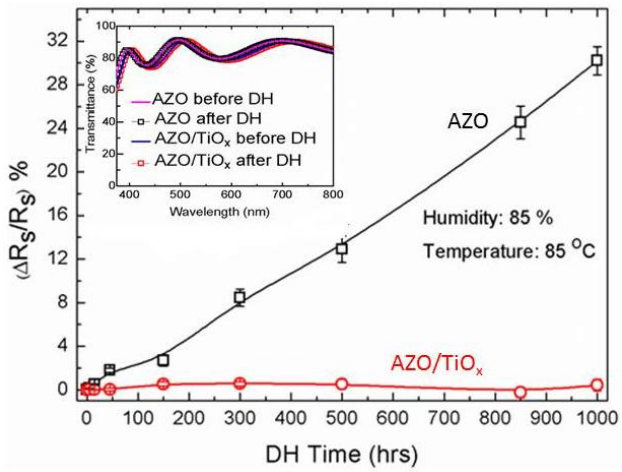

Figure 4.11: *Electrical sheet resistance as a function of time for damp heat test performed at 85 °C and 85% relative humidity. The inset shows the optical transmittion of the samples before and after DH test.*

4.4 Graphene as an anti-permeation and protective layer for UTMFs and AZO TCs

Recently, Bunch et al showed that a monolayer of graphene can be impermeable to standard gases like helium [24] and it can function as a corrosion-inhibiting coating for underlying bulk metals [25, 26]. The high transparency combined with its mechanical flexibility and structural stiffness makes thus graphene an ideal corrosion resistant and anti-permeation layer. Furthermore, monolayer graphene on glass substrate without doping still yields sheet resistance values of more than 1 kΩ/sq [27, 28], so it could be a viable way to combine monolayer graphene with other TC to scale down its sheet resistance.

In this section, we show that monolayer of graphene can be utilized as an anti-permeation layer for indium-free TCs. In particular, it is capable to protect AZO and ultrathin Cu films in severe environmental conditions of high temperature and humidity, while maintaining their low sheet-resistance.

4.4.1 Methods

Indium-free TCs of 250 nm-thick AZO films and 8 nm-thick Cu ultrathin metal layers were deposited on fused-silica glass and polyethylene terephthalate (PET) substrates by sputtering. A DH test in harsh conditions of 95ºC and 95% relative humidity was performed. Note that we have chosen to go beyond the standard 85 ºC and 85 % relative humidity test to better show the effectiveness of the graphene layer against heat and moisture. The quality of the transferred graphene films was assessed using Raman spectroscopy (Renishaw InVia Raman microscope, 532 nm laser and 100× objective lens).

CVD grown graphene on Cu foils (purchased from Graphenea) was transferred by spin coating a thin layer of poly(methyl-methacrylate) (PMMA) on top of graphene/Cu foil. The underneath Cu

foil was dissolved by floating the PMMA/graphene/Cu foil structure in a concentrated $FeCl_3$ solution under constant heating at 80 °C. The PMMA/graphene was transferred by direct contact onto AZO, Cu films on glass substrates, and Cu films on flexible PET substrates. Finally, the PMMA layer was dissolved with acetone, leaving the graphene as a protective layer for our TE structures. We label the graphene capped AZO and Cu layers on glass substrate as G/AZO and G/Cu respectively, while the graphene capped Cu layer on flexible PET substrates is labeled as f-G/Cu.

4.4.2 Results and discussion

When AZO thin films are exposed to either temperature in ambient air or particularly humid environments, its surface starts degrading, thus affecting its use in devices that require long term reliability. Figure 4.12 shows clear differences between G/AZO and AZO. With a single-sheet graphene as an anti-permeation layer, AZO shows no observable change in optical transmission during DH test up to 30 days, while in the case of pure AZO, there in an evident degradation

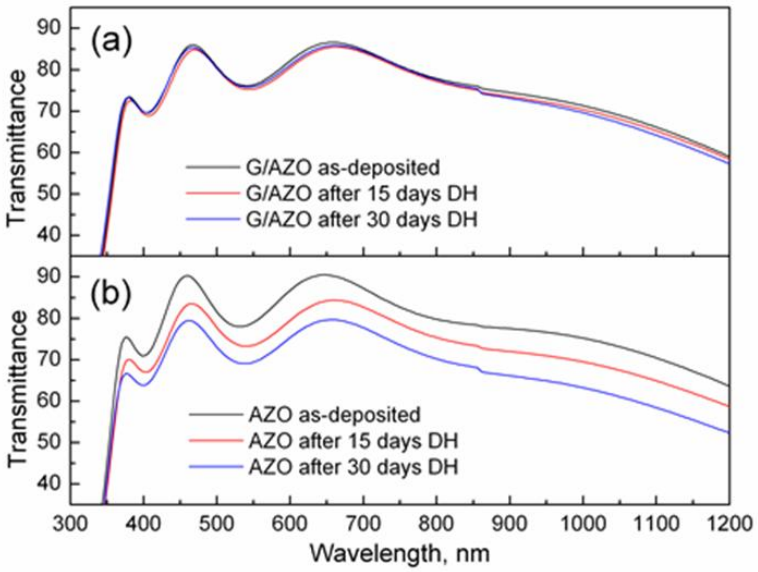

Figure 4.12: *Transmittance Spectra for* ***(a)*** *graphene capped AZO (G/AZO) and* ***(b)*** *AZO only after 95 °C and 95% relative humidity DH*

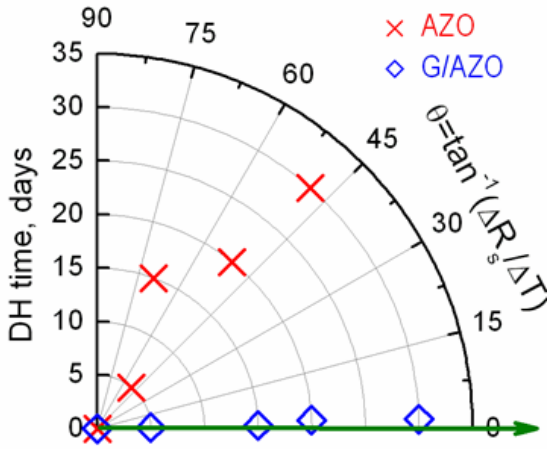

Figure 4.13: *Polar graph of electrical sheet resistance change during DH for AZO and G/AZO samples. The green horizzontal line (x) axis corresponds to perfect stability.*

with time. The difference is also evident in the change of electrical sheet resistance during DH. From Figure 4.13 one can see that G/AZO is much more electrically stable than AZO only. The optical and electrical measurements indicate that the graphene capping layer covers the entire surface and serves as a protective layer against the penetration of oxygen and water into the AZO's grain boundaries.

The surface morphology of G/AZO and AZO samples was characterized by an optical microscopic image (×5 magnitude) before and after the DH test. Note that the optical intensity for each microscopic image is kept as the same for the measurements. Before the DH test, typical images for both samples are featureless (Figure 4.14a and 4.14b). After 30-day DH, the surface morphology of G/AZO remains almost unchanged (Figure 4.14c) while that of AZO shows spikes and droplet-like spots distributed in a random manner, in which the dark contrast is due to large loss of light reflection from rough surface (Figure 4.14d).

The quality of the transferred graphene on AZO surface after 30-day of DH was also determined by Raman spectra.

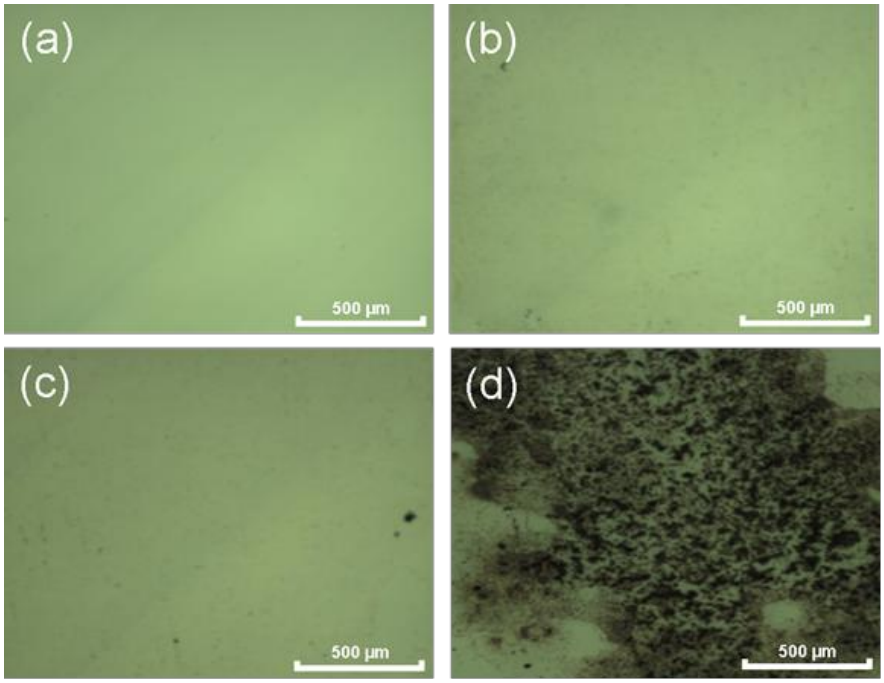

Fig.4.14: *Optical microscope image (5x magnitude) for the surface morphology of G/AZOand AZO samples before and after the 30 days DH test a) AZO before DH b) G/AZO before DH c) G/AZO after DH d) AZO after DH*.

The Raman spectrum shows two distinctive features (Figure 4.15): a relatively small G/2D peak ratio ~ 0.4 which is indicative of high quality single layer graphene [29], and almost negligible peak intensity of D and D' bands which are closely related to defects in graphene (such as disordered carbon, edges or wrinkles) [30]. The inset of Figure 4.15 also gives the Raman spectrum of the transferred graphene on AZO before the DH test, which giving almost the same interpretation about the quality. This confirms that the graphene has essentially maintained its structure and quality after the DH test.

We further characterized the surface morphology of AZO and G/AZO samples before and after DH by AFM. Figure 4.16 shows that AZO presents a very rough surface with a RMS value after the DH test greater than 100 nm while G/AZO exhibits an almost unchanged

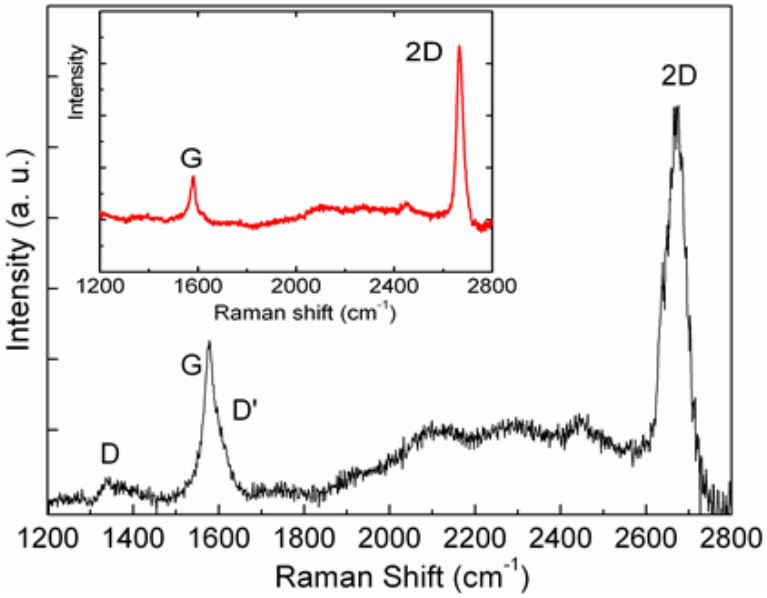

Figure 4.15: *Raman spectrum of the GAZO sample after 30 day DH test. The inset is the spectrum before DH.*

surface roughness compared to the values before DH (the RMS values before DH for AZO and G/AZO are 1.9 nm and 2.1 nm, respectively).

The Raman spectrum, optical and AFM images are further indications that graphene can provide a dense, uniform and smooth protective in harsh humidity and temperature conditions.

Also Cu UTMFs are strongly susceptible to oxidation, especially at elevated temperature, which alters significantly their electrical and optical properties. For this reason we performed a DH test for the G/Cu and only Cu samples, which indicates that the former one can sustain more than 12 hours with a relative electrical sheet resistance change of 10 %, while the latter one degrades in less than 3 hours when subjected to the similar harsh environment.

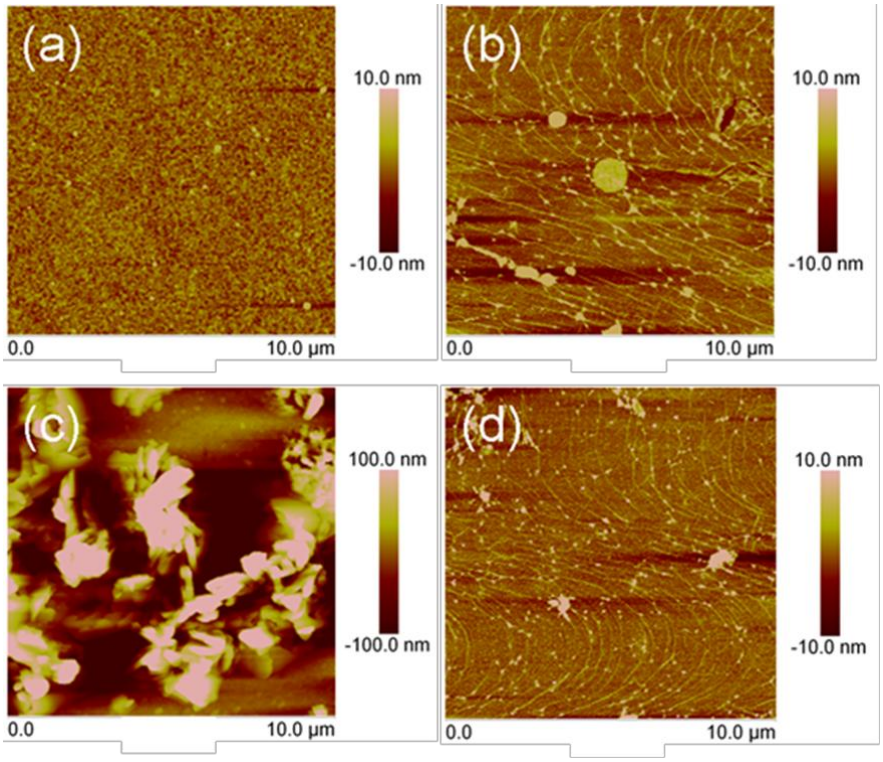

Figure 4.16: *AFM images for as deposited (a) AZO and (b) G/ AZO; for (c) AZO and (d) G/AZO after 30 day DH tests*.

To better evaluate the stability, we opted for a temperature treatment in ambient air. A dwell time of 30 mins at several fixed temperatures was applied and the electrical sheet resistance after each thermal cycle was measured when the sample was cooled down to room temperature. Figure 4.17 shows the stability improvement of the Cu UTMF when a capping graphene layer is used. The change in electrical sheet resistance reaches high values for temperatures beyond 100 ºC for the only Cu layer, while for the G/Cu it remains relatively small up to 180 ºC. The abrupt increase in sheet resistance for f-G/Cu (Figure 4.17 right), in particular with respect to the G/Cu on glass substrate, resulted from the corresponding temperature degradation of the underlying PET substrate. Note that the temperature dependence of the electrical sheet resistance of G/Cu can be well fitted by an Arrhenius Eqn. (4.2):

(4.2) $$\ln(\psi) = (-E_a / R)T + \ln(A)$$

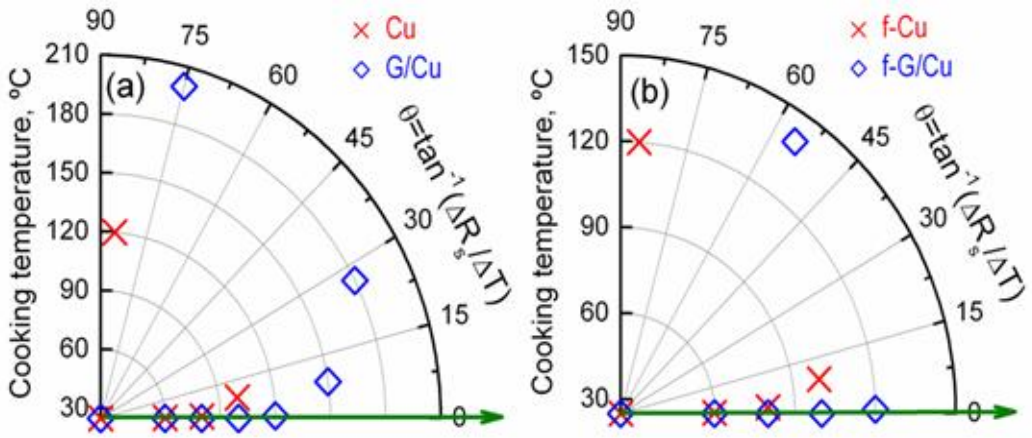

Figure 4.17: *Polar graph of electrical sheet resistance change with temperature for Cu and G/Cu* ***(a);*** *and f -Cu and f- G/ Cu samples* ***(b).*** *The green horizontal line axis corresponds to perfect stability.*

where $\ln(\psi)$ is the natural logarithm of the sheet resistance change ratio as $100\Delta(R_T - R_0)/R_0$, T is the absolute temperature in Kelvin, A is a pre-exponential factor, R is the universal gas constant and E_a the activation energy. From the fitting E_a can be estimated to be 71.06 kJ/mol, as shown in Figure 4.18. It was reported that Cu oxidation at low temperature regime obeys the parabolic law and the grain boundary diffusion would contribute more to Cu oxidation, as a consequence, the activation energy gives a relatively low value of 40 kJ/mol [31]. The increase in the measured activation energy could ascribe to the inhibiting oxygen diffusion and possible effect that the graphene film itself may have on the measured heat resistance. It is thus concluded that graphene capping layer can improve the oxidation resistance for Cu ultrathin layer. Considering also its low cost and the room temperature processing, the developed f-G/Cu TCs have great potential for the flexible optoelectronics industry. It can be expected that the proposed

approach for overcoming the instability is applicable not only to AZO and UTMFs, but to any other transparent conductor materials which suffer from changes in damp heat and elevated temperature environments.

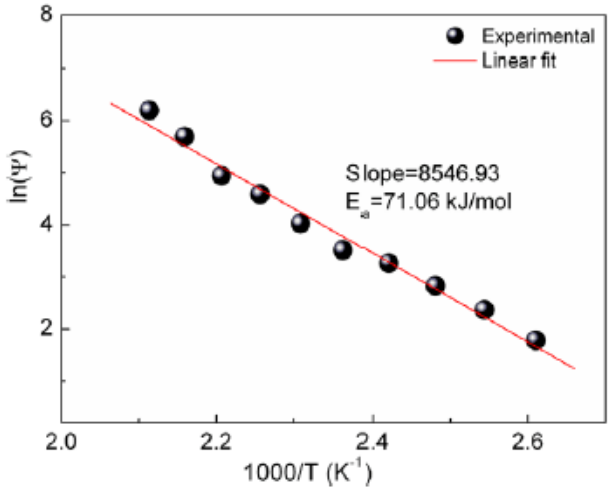

Figure 4.18: *Temperature dependence of the electrical sheet resistance change ratio ($\Psi=100\Delta R/R_0$ of G/Cu sample, which shows a clear Arrehenius behavior.*

In conclusion we have demonstrated that single-sheet graphene is an effective material to improve the stability of transparent conductors, thanks to its impermeability to water, oxygen and temperature resistance. In particular AZO and Cu film, both on glass and PET substrates capped with graphene show enhanced stability in damp heat (95 ºC and 95 % relative humidity) and high temperature conditions, with very little changes in optical transmission, sheet resistance and surface morphology.

References

[1] T. L. Chen, D. S. Ghosh, D. Krautz, S. Cheylan and V. Pruneri, Appl. Phys. Lett. 99 093302, 2011.

[2] F. Ruske, M. Roczen, K. Lee, M. Wimmer, S. Gall, J. Hupkes, D. Hrunski and B. Rech, J. Appl. Phys. 107 013708, 2010.

[3] F. J. Pern, S. H. Glick, X. Li, C. DeHart, T. Gennett, M. Contreras and T. Gessert, Proc. SPIE 7412 74120K, 2009.

[4] L. Martinez, D.S. Ghosh, , S. Giurgola, P. Vergani, V. Pruneri, Opt. Materials 31, 8, 2009.

[5] S. Cheylan, D. S. Ghosh, T. L. Chen, D. Krautz, V. Pruneri, Organic Electronics 12, 818, 2011.

[6] S. Major et al., Appl. Phys. Lett. 49, 394, 1986.

[7] T. Minami et al., Thin Solid Films 176, 277, 1989.

[8] F. Haug, Z. Geller, H. Zogg, A N Tiwari, C. Vignali, J. Vac. Sci. Technol. A: 19 : 171, 2001.

[9] C. Guillen, J. Herrero, Vacuum 84 924, 2010.

[10] H. Tong, Z. Dong, Z. Liu, C Huang, J.Huang, H. Lan, C. Wang, Y. Cao Applied Surface Science 257, 4906, 2011.

[11] S.S. Lin, J.L. Huang, P. Sajgaik, Surf. Coat. Technol. 185, 254, 2004.

[12] B.D. Ahn, S. H. Oh, C.H. Lee, G.H. Kim, H. J. Kim, S.Y. Lee, J. Cryst. Growth 309, 128, 2007.

[13] W. Yang, Z. Wu, Z. Liu, A. Pang, Y-L. Tu, Z. C. Feng, Thin Solid Film 519, 31, 2010.

[14] E. Burstein, Phys. Rev. 93, 632, 1954.

[15] P.A. Wolff, Phys. Rev. 126, 405, 1962.

[16] B.E. Sernelius, K. F. Berggren, Z.C. Jin, I. Hamberg, C. G. Granqvist, Phys.Rev. B 37 10244, 1988.

[17] J.F. Chang, W.C. Lin, M.H. Hon, Applied Surface Science 183, 1, 12, 18, 2001

[18] T. Miyata, Y. Honma Y, T. Minami, J. Vac. Sci. Technol. A 25, 1193, 2007.

[19] M. Neghabi, A. Behjat, S.M.B. Ghorashi, S.M.A. Salehi, Thin Solid Films 519, 16, 1, 5662, 2011.

[20] J.C. Bernède, Y. Berredjem, L. Cattin, M. Morsli, Appl. Phys. Lett. 92, 083304, 2008.

[21] T.W. H. Oates, D.R. McKenzie, M.M.M. Bilek, Phys. Rev. B 70, 195406, 2004.

[22] G.Liu, J. B. Kerr, S. Johnson, Synthetic Met. 144, 2004.

[23] A. Fujishima and K. Honda, Nature, 238, 37, 1972.

[24] B. J. Scott, S. Verbridge, J. S. Alden, A. M. Zande, J. M. Parpia, H. G. Craighead and P. L. McEuen, Nano Lett. 8 2458, 2008.

[25] D. Prasa, J. C. Tuberquia, R. Harl, G. K. Jennings and K.I. Bolotin, ACS Nano 6 1102, 2012.

[26] S. Chen et al, ACS Nano 5 1321, 2011.

[27] C. Mattevi, H. Kim and M. Manish Chhowalla, J. Mater. Chem. 21 3324, 2011.

[28] X. Li, Y. Zhu, W. Cai, M. Borysiak, B. Han, D. Chen, R. D. Piner, L. Colombo and R. S. Ruoff, Nano Lett. 9 4359, 2009.

[29] A. C. Ferrari et al, Phys. Rev. Lett. 97 187401, 2006.

[30] A. C. Ferrari, Solid State Commun. 143 47, 2007.

[31] Y. Zhu, K. Mimura and M. Isshiki, Mater. Trans. 43 2173, 2002.

Chapter V

Transparent Conductors on flexible substrates

The development of flexible substrates that are based on organic polymers is of critical importance for a wide range of applications, including light emitting diodes, photovoltaic cells, tactile displays, etc. Mechanical flexibility is needed for making foldable devices and, most importantly, for producing those using inexpensive roll-to-roll techniques. At the same time optical transparency, low weight and cost effectiveness are maintained.

TCO/metal/TCO multilayer structures have emerged as competitive alternative transparent conductors (TCs) because they provide optical and electrical characteristics globally superior to those attainable with a single-layer TCO or metal electrode and can be deposited at low temperatures onto inexpensive plastic substrates [1-8]. The implementation of roll-to-roll deposition processes can significantly reduce the production costs of TCs' films. In this chapter we present new TC structures deposited on flexible thin glass (Corning Inc. Willow glass) and PET substrates. Compared to plastic PET substrate, besides mechanical flexibility, Willow offers superior surface finishing, impermeability to water, chemical and thermal resistance.

5.1 Flexible substrates

When mechanical flexibility is not a requirement, the most widely used substrate material for TCs is glass as it is transparent, smooth, impermeable to water and oxygen, chemically and thermally stable.

For applications where a transparent flexible substrate is required, plastic films are usually employed. Polymer foil substrates can be inexpensive and allow roll-to-roll processing. However, a disadvantage is that they absorb water moisture, which eventually penetrates through

the film and potentially leads to TC degradation. This is a challenging problem to be solved and substantial efforts are needed to develop effective barrier layers, which can enhance the stability as well as the adhesion of the TCs without compromising their flexibility.

When dealing with TCs on polymeric substrates, key parameters to be taken into account are:

- Barrier against permeation of water and oxygen
- High optical transmission
- Mechanical stability against bending
- Thermal stability

In choosing an appropriate plastic (polymer) film, it is useful to categorize the available options by the glass transition temperature (Tg) as this defines the range of accessible processing temperatures and time during which material and devices can be processed. Another key distinction is whether the underlying structure is amorphous or semi-crystalline as this leads to different thermo-mechanical film properties.

Thermoplastic semi-crystalline polymers include polyethylene therephtalate (PET) and polyethylene naphtalate (PEN). PET has a relatively low Tg, around 78 °C, while PEN has Tg around 120 °C. Due to their semi-crystallinity, PET and PEN have relatively low coefficient of thermal expansion (CTE) which is around 15 ppm/°C and higher solvent resistance when compared with amorphous polymeric films.

The dimensional stability of PET and PEN films can be enhanced by heat, which releases the internal stress in the film while it is under minimum line tension. The heat stabilization process dramatically reduces the shrinkage rate of PET and PEN films at temperatures above their glass

transition and thereby extends the accessible process temperature range. For instance, even though PET has a Tg of 78° C, when thermally stabilized it can be processed at temperatures above 100 °C [9-10].

Examples of thermoplastic amorphous polymers include polycarbonates (PCs) and polythersulfones (PES). New engineered PCs are now commercially available with Tg around 220 °C. PES materials also offer Tg around 220°C. Both PC and PES have relatively high CTE (50-70 ppm/°C) due to their amorphous structure.

Most of the plastic films described above deliver optical transparency over the visible light range. Polymeric films tend to undergo undesirable change in dimension when heated to high temperatures due to the molecular relaxation associated with the increased mobility of polymer chains and relaxation of residual strain within the film. The effect is in general less pronounced for semicrystalline polymers than for amorphous polymers [11].

All these substrates choices have advantages and disadvantages and they most often require additional coatings that can provide function of barrier layer to moisture and oxygen.

Although all materials listed above are potential candidates, not all of them are commonly used. Polyetheretherketone (PEEK) for instance is a high performance plastic used in applications where mechanical strength, high temperature and chemical resistance are of great importance. However, the price can be up to 100 times that of PET and it is only frequently used in the automotive and aerospace industry. On the other hand PET, PC and Poly Methyl Methacrylate (PMMA) are used in a broad range of applications as plating or packaging. Despite of this, PMMA is quite brittle, which can become a potential problem during material processing. The optical properties of PC on the other hand were found to be of less quality. The onset of

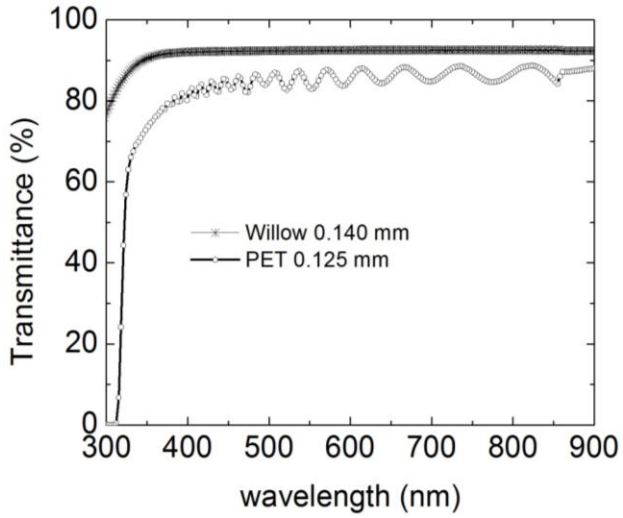

***Figure 5.1**: Transmission spectra of optical transparent polymer PET and willow glass substrates. The thicknesses of willow and PET substrates are 0.140 mm and 0.125 mm, respectively.*

***Table 5.1**: Main properties of the PET substrate selected [13].*

PET	
Thickness (mm)	0.125
Density (g/cm^3)	1.4
Tensile strength (MPa)	196
Elongation to break (%)	80-125
Young Module (MPa)	2000-4000
Melting point (°C)	255-260
Glass transition temperature (°C)	79
Thermal shrinkage (%) (190°C,5 min)	3
Coefficient of thermal expansion (10^{-6}/K)	16-19
Upper Temperature for Processing (°C)	120
Water Vapor Transmission Rate (WVTR) (g.mm/m^2/day)	11 @ 85 °C
Refractive index	1.58-1.64
Roughness R_a(nm)	0.59

***Figure 5.2**: Picture of Willow Glass*

***Table 5.2**: Main properties of Willow glass [14]*

Corning Inc. Willow Glass	
Density (g/cc)	2.3-2.5
Coefficient of thermal expansion (0 to 300) (ppm/°C)	3-5
Young Module (GPa)	70-80
Poisson Ratio	0.20-0.25
Strain point (°C)	650-700
Maximum Temperature (°C)	700
Dielectric Constant ($k=E_0/E$)	5-6
Surface Roughness R_a (nm)	0.5
Refractive index	1.523
Water Vapor Transmission Rate (WVTR)(g.mm/m2/day)	$<5 \times 10^{-5}$ @85 °C
Thickness (mm)	0.140

adsorption at higher wavelength may obstruct the measurements of the thin film optical properties.

From these materials, PET was selected for the experiments since it is optically clear with a transmission > 85% in the visible, it is resistant to most of chemical solvents and can be delivered with a low average surface roughness and has low price. Its process temperature is around 150 °C after pre-stabilization by annealing. Additionally, the adhesion of common sputtered barrier layers is good. PET exhibits high value of water vapour permeability rate, around 10^2 g/m^2 day [12].

Glass sheets, when sufficiently thin (thickness < 200 μm), become flexible. This is the case of Corning Incorporated's Willow glass, which has been used in this thesis. It has the clear advantage of impermeability against oxygen and water. Some of the main properties of both substrates are listed in Tables 5.1 and 5.2. Figure 5.1 shows the spectra of PET and Willow glass in the 300-900 nm range.

5.2 Barrier Layers

Lack of impermeability to moisture and oxygen is a serious deficiency of all the plastic substrates for flexible applications. Different devices including LCDs and OLEDs degrade when exposed to oxygen and moisture in the ambient, even though at different rates with OLED having the most sensitivity to moisture and oxygen. For example, for the protection of an OLED display the substrate must have a permeability of less than 10^{-6}gm/m^2/day for moisture and 10^{-5} mL/m^2/day for oxygen. In comparison, LCD displays have a barrier requirement of 10^{-2}gm/m^2/day for both oxygen and moisture, which is significantly less stringent compared to

OLEDs. The base plastic substrates typically have about 10 gm/m^2/day transmission rates for both oxygen and moisture, implying the need of incorporating an additional barrier layer**.** In principle, a thin layer of an inorganic film such as SiO_2, SiN_x, or Al_2O_3 deposited on the flexible plastic substrate can serve as a barrier layer with the required impermeability to oxygen and moisture [15, 17]. However, in practice multilayer barrier film structures are used to counter the effects of the pinholes/cracks of single layers. Optically transparent multilayer barrier coatings have been developed for flexible OLED displays. For example a barrier film called BarixTM employs alternating layers of polymer and ceramic inorganic barrier coatings applied in vacuum [18]. The inorganic films serve as barrier layer for oxygen and moisture, organic layers serve the planarization/smoothing function, and multilayers provide redundancy against pinhole defects in the barrier films. The BarixTM layer is found to be an effective barrier layer, by minimizing the detrimental effects of pinholes and diffusion at grain boundaries. The film is about 3 μm thick and consists of about 50 nm thick Al_2O_3 ceramic films sandwiched between UV-cured acrylate films.

5.3 Mechanical properties of TCOs and thin metal films on polymer substrates

Adhesion is a fundamental surface property, often governed by a layer of molecular dimensions [19]. It is therefore useful to modify the polymer surfaces to enhance their adhesion to other materials. For this purpose several methods have been developed including mechanical treatments, wet-chemical treatments, exposure to flames, corona discharges, UV and plasma treatments [20-22]. It has been shown that pre-treatment of the PET substrates improves the adhesion and it is even beneficial for the mechanical properties [23-25]. Indeed, besides adhesion, another important issue while dealing with polymers is the stress build-up during

deposition of thin films onto them, which can lead to crack onset or delamination of the thin film.

The resultant stress in a thin film is the summation of the intrinsic, thermal and external stress [26]. As the coefficient of thermal expansion and compliance of the plastic substrates are larger than those of TCOs, some compressive internal stress is usually induced during deposition of TCOs. The resulting compressive strain is released upon cracking and sometimes the large difference in shrink rate between film and substrate leads to delamination of the thin film. Mechanical failure of the thin film due to thermal stresses is a commonly known problem in the coating of plastics above room temperature [27].

Polymer substrates cannot sustain high temperatures normally required (300-500 ºC) to grow ITO films with excellent properties, i.e. low resistivity and high optical transmittance. A precise control of the ITO process parameters during growth is therefore required in order to obtain high quality films at low substrate temperatures, allowing deposition on polymer substrates.

In fact, in order to obtain crack-free ITO films on polymers, the thin film growth is restricted to room temperature. Unless the resulting lower crystalline nature of ITO, other deposition parameters have to be tuned, so that growth of high performance coatings remains possible. In order to grow ITO at room temperature with a high transmittance and low resistivity, an optimum oxygen pressure has to be sought. Sputtering at a low working pressure on PET substrates produces ITO films with large compressive stress, which becomes tensile at a higher pressure with a gradual transition through a zero-stress condition occurring at an intermediate value [28]. Similar decrease in the compressive stress by increasing the sputtering working pressure has been obtained for ZnO and Al:ZnO thin films. The internal stress of ITO and AZO

samples deposited on PET also decreases when the sputtering power is decreased or the target-to-substrate distance increased [29, 30].

One way to overcome the mechanical fragility of TCO based TCs is to add a ductile material like UTMF, in a UTMF/TCO or TCO/UTMF/TCO configuration, which has better electrical performance with a significant TCO thickness reduction. For example, PET/Al/ITO structures show superior mechanical stability compared to PET/ITO samples [31, 32]. A recent analysis of the influence of the Ag layer thickness on the mechanical reliability of PET/Ag/ITO structures, with 150-nm-thick ITO films, indicates that both the crack and delamination resistance is significantly improved only above a certain metal thickness. For 5-nm-thick Ag film, weak adhesion at the interfaces was observed, but the adhesion improved as the Ag film thickness was increased to 10 and 15 nm. The tensile stress at cracking was higher for the 15-nm-thick Ag layer. The improved crystallinity of the ITO film by the metal layer was thought to be the primary factor for enhancing crack resistance since significant grain growth was detected in the 15-nm-thick Ag film. The same effect is observed even for ITO/Au/ITO and AZO/Ag/AZO samples onto bare PET substrates [37-39], where the enhanced crystallinity is beneficial for the mechanical stability. Standard bending tests performed for samples deposited on flexible substrates [33-36] demonstrate the superior mechanical reliability of the TCO/Ag/TCO TCs in comparison with single-layer TCOs. TCs consisting of PET/ITO/Ag/ITO with at least 8 nm thick Ag interlayer show improved performance even after many cycles of bending with respect to ITO only. This indicates that the ductility of the Ag layer can provide effective electrical conductivity even after the ITO films are beyond their failure strain.

Also the rupture strain of a metal film is sensitive to its adhesion to the polymer substrate. Ductility of a thin metal film depends on its adhesion to the substrate. A well-bonded substrate

brings the film to large tensile strain without rupture by delocalizing deformation in the film. A poorly bonded substrate allows the film to form channel cracks at relatively small macroscopic strains by facilitating the co-evolution of strain localization and delamination. The ductility of metal film is also limited by inter-grain fracture. The geometric constraint of the substrate is effective in retarding strain localization but it is less effective in retarding inter-grain fracture, because the latter requires little additional space to proceed. If the granular fracture does not intervene, a metal film well-bonded to a substrate can sustain strain far beyond 30% [40].

In the following paragraphs we demonstrate the importance of the preheating process of PET substrates to improve the stability of the TC deposited on top of them and the achievement of low sheet resistance and high transmittance values with reduced film thicknesses by a multilayer structure consisting of TCO/metal/TCO onto willow glass and PET, which offers superior performances compared to single-layer TC. The flexibility of the obtained TCs was tested for demonstrating a mechanical stability better than that of ITO single layers**.**

5.4 Ag-Ni bilayer TC on PET substrate

The combination of Ag and Ni UTMFs can lead to stable and highly performing TCs on flexible substrate. In this section we describe the electrical, optical characteristics and surface morphology of a thin Ag–Ni bilayer sputtered on a flexible PET substrate and demonstrate its high stability. The results also show that cleaning procedures and pre-treatments of the PET substrates are of crucial importance to obtain a stable TC on a polymer substrate. In fact, if it is properly treated, the proposed Ag–Ni/PET structure can withstand high temperature and damp heat conditions, even without any additional barrier layer.

5.4.1 Experimental details

The ultrathin Ag–Ni bilayers were deposited on a PET substrate (125 μm thickness, Melinex ST504 Dupont) by DC magnetron sputtering using Ag and Ni targets. Ag and Ni depositions were carried out sequentially on the PET substrate without breaking the vacuum in the main chamber, at a base pressure of 10^{-7}–10^{-8} Torr, room temperature, DC-power 100 W and pure Ar working pressure of 2×10^{-3} Torr. The deposition rates of Ag and Ni were 0.252 nm/s and 0.573 nm/s, respectively, and the target-substrate distance was 30 cm.

5.4.2 Results and discussion

The cleaning procedure and other pretreatments are always a critical step for polymer substrates and influence the stability of the films deposited on them, more specifically UTMFs for OSCs in our case. Prior to any UTMFs' deposition, the PET substrates were ultrasonically cleaned in acetone and ethanol for 10 min, respectively, and subsequently dried by using nitrogen gas.

Ag–Ni UTMFs on PET substrates with different pretreatments were prepared in order to determine those with highest stability properties. Considering that Ag nanolayers easily degrade when exposed to the environment, we covered the thin Ag films by a 1 nm Ni top layer. In our previous work, it was shown that Ni capped Cu UTMFs exhibit excellent stability against temperature and oxidation and when used as an anode in OLEDs or OSCs, the devices show similar efficiency as ITO based devices, with satisfactory operation stability over time [41]. The Ni capping layer protects the underlying ultrathin metal layer from oxidation, without affecting significantly its optical and electrical characteristics, and at the same time increases the work function which is an important parameter for OLEDs and solar cells.

Several samples [SX, X=1–7] consisting of Ag 9 nm–Ni 1 nm bilayer UTMFs were deposited onto PET substrates with different pretreatment to assess their stability properties. S1 was without any pretreatment, S2 was pretreated in-situ by Ar plasma for 15 min at a pressure of 8 mTorr and 40 W RF power, S3 was kept at 120 °C in ambient atmosphere for a dwell time of 10 min prior to the loading into the sputtering machine, S4 was pretreated by a combination of heat (120 °C) and Ar plasma treatment, S5 was covered by a blocking layer of 20 nm TiO_2 layer on the back side of the PET substrate, S6 was covered by a blocking layer of 20 nm TiO_2 layer on the side of the PET substrate where the UTMF was deposited, and S7 was the sample which was covered with a blocking layer of 20 nm TiO_2 layer on both sides of the PET substrate. The TiO_2 blocking layer was deposited directly from a titanium dioxide target in the same chamber prior to the deposition of Ag9–Ni1 layer. Except for the sample S5 all other samples were prepared without breaking the vacuum. Details of the different pretreatments performed for the fabricated samples are summarized in Table 5.3.

Table 5.3*: Summary of pretreatments for SX samples.*

Sample	Pretreatments
S1	Without pretreatment
S2	Ar Plasma (15 min, 8 mTorr 40 W RF power)
S3	Heat (10 min at 120 °C, ambient atmosphere)
S4	Ar Plasma+Heat
S5	TiO_2 Blocking layer (back side)
S6	TiO_2 Blocking layer (in contact with UTMF)
S7	TiO_2 Blocking layer (both sides)

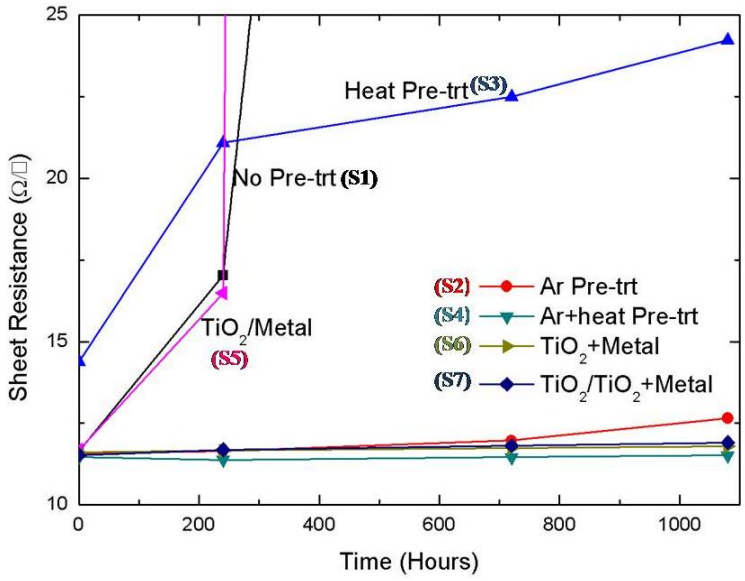

***Figure 5.3**: Change over time of the electrical sheet resistance for different pretreated samples of Ag9nm–Ni1nm UTMFs on PET.*

Figure 5.3 summarizes the results on the change of sheet resistance for all samples as a function of time. From the graph one can see that without any pre-treatment the samples degrade in about 10 days. Depositing a moisture blocking layer on the front side (where the metals are deposited) certainly helps in increasing the stability of the samples, at the expense of the simplicity of the structure. In addition, it was found that heat treatment and Ar plasma treatment increases the stability. S4 does not show any change in sheet resistance even after 1080 h (45 days), making evident the need of Ar plasma to achieve the stability of the samples. In fact a combination of heat and Ar plasma treatments is demonstrated to be the best possible pretreatment of those studied in this work to achieve stability (S4).

The preheating treatment is expected to remove water, moisture and impurities gases present in the PET substrate which deteriorate the electrical properties of Ag–Ni thin films. Together with

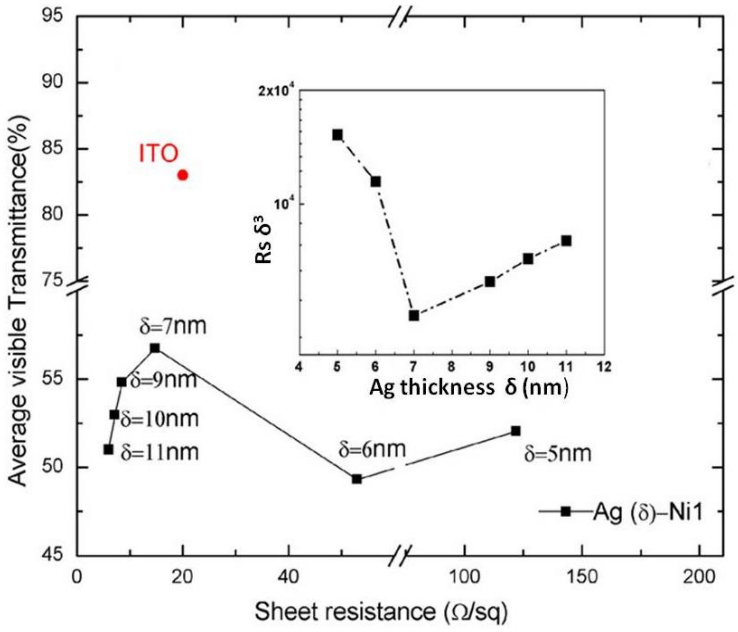

Figure 5.4*: Average of VIS Transmittance as a function of electrical sheet resistance of Ag–Ni thin films for different Ag thicknesses (δ) and same 1 nm Ni capping layer for all samples, compared with that of standard ITO. The inset shows* $R_s \delta^3$ *vs. δ for determining the percolation threshold.*

the outgassing of moisture, pre-annealing of PET before any deposition can also prevent or minimize the stress induced during the device fabrication and effect of shrinkage due the thermal expansion mismatch between the polymer substrate and the metal film. This indeed generates cracks which can affect the integrity of the metal electrode on top leading to the failure of the device. The Ar plasma treatment increases the PET surface energy enhancing the wettability of the metal film over the plastic substrate and thus the adhesion of thin film deposited immediately after the plasma treatment. PET substrates with an improved adhesion to the metal film can tolerate higher stress retarding the cracking and delamination processes and preventing changes in the conductive properties of the metal film.

Therefore, the preheating and plasma treatments can enhance the long term stability of the TC and thus of the OSC device.

Once the pretreatment for the PET substrate had been determined, we optimized the deposition conditions to achieve a good trade-off between sheet resistance and optical transmittance for our Ag–Ni films. Figure 5.4 shows the average-visible transmittance versus sheet resistance (R_s) for Ag(δ)–Ni1 samples with different Ag thickness (δ). Both optical and electrical parameters show an abrupt change when the Ag film thickness changes from 6 nm to 7 nm. As it is evident from the graph, the R_s changes from 53 to 13 Ω/sq and the average visible transmittance from about 49% to 56%. By plotting $R_s\delta^3$ as a function of the Ag thickness (δ) for the different samples we estimated the percolation threshold to be at 7 nm for Ag film (figure 5.4 left) [42]. At the percolation thickness, the Ag film goes from an island like to a continuous layer structure. The

existence of these different film structures as a function of the thickness is in agreement with the evolution of thin film growth proposed by Seal et al. [43].

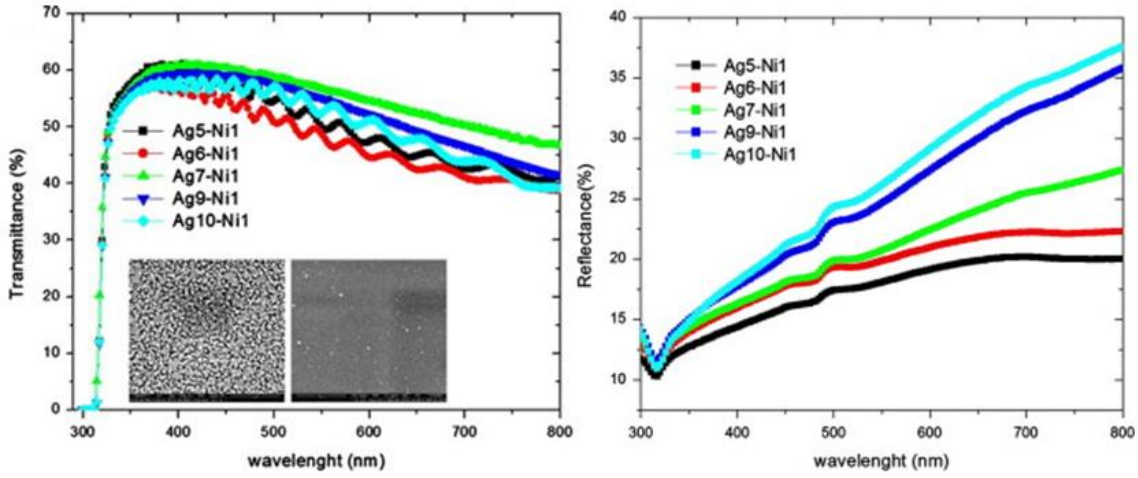

Figure 5.5*: Visible transmittance spectra of Ag(δ)–Ni 1 nm films. The inset shows the SEM image of Ag films at the percolation threshold (left) and above the percolation; (right) Reflectance spectra of Ag(δ)–Ni 1 nm films for different δ Ag thicknesses.*

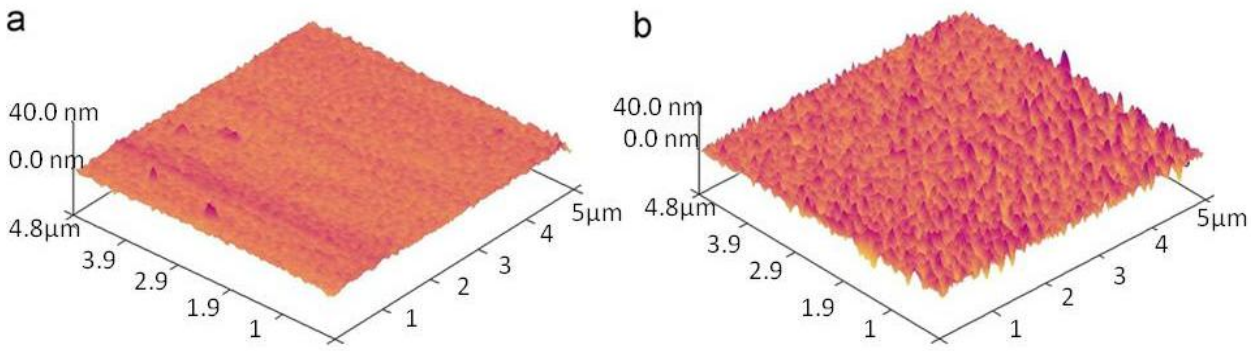

***Figure 5.6**: AFM images (scanning area of 5×5 µm^2) of (a) ultrathin Ag 7 nm and (b) Ag 7 nm+Ni 1 nm films on PET substrate*.

The effect of the thickness on properties of Ag films is crucial, e.g, the structure, morphology, electrical, optical properties, thermal stability rely on the thickness of Ag films. The effect of thickness on electrical and optical properties can be correlated with the size and the shape of Ag grains.

Optical transmittance and reflectance spectra in the 300–800 nm range for the Ag (δ) +Ni1 films are represented in Figure 5.5. Reflectance curves show a minimum corresponding to a characteristic absorption edge in the UV spectral region at a wavelength of 320 nm due to PET substrate. The reflectance increases with increasing Ag film thickness, while due to significant scattering effects resulting from the islands the transmittance decreases with the film thickness up to the percolation threshold. At the percolation, the scattering becomes lower for quasi continuous films and the transmittance increases. Beyond the percolation thickness, the Transmittance starts decreasing again as one expects for continuous films. From the transmittance spectra of silver films with various thicknesses, the optical percolation transition was found to occur near a film thickness of 7 nm.

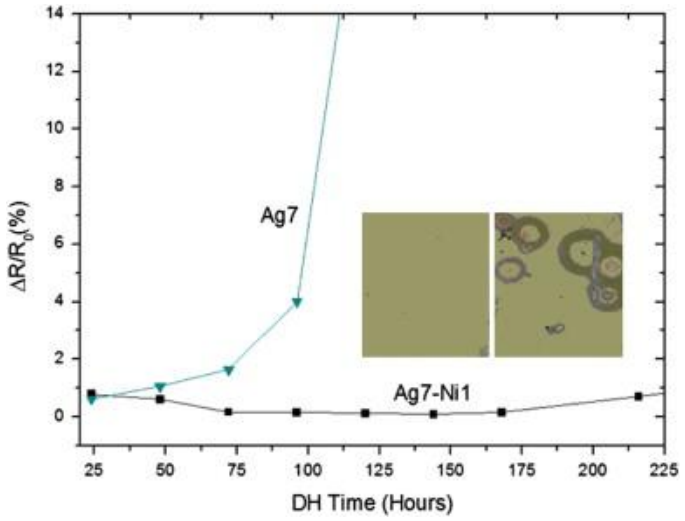

Figure 5.7*: Relative sheet resistance variation of Ag7/PET and Ag7–Ni1/PET samples during 85 °C/85% humidity DH test; the inset is the Optical microscope image of Ag7–Ni1/PET sample (left) before DH test and (right) after 9-day DH test*.

The AFM topography images shown in Figure 5.6 reveal an average RMS surface roughness of 1.51 nm for Ag7 and 3.9 nm for Ag7–Ni1 film. This latter RMS value for Ag–Ni film is still acceptable compared to the data reported in literature for Ag layers grown by conventional techniques, including e-beam evaporation and sputtering [44-47]. In addition, the peak-to-valley value measured by AFM for those samples with Ag thickness corresponding to 7 nm is higher than the film thickness, which implies that the films are discontinuous over microscopic dimensions. To further investigate its stability, the Ag7–Ni1 sample, with heat and Ar plasma pretreatment, underwent a post-deposition cumulative thermal annealing. The samples were kept in ambient air for a dwell time of 60 min at several temperatures (35 °C–150 °C) and the corresponding sheet resistance was measured after each thermal cycle once the sample was cooled down to room temperature.

We compared Ag7–Ni1/PET and Ag7/PET samples (pretreated by a combination of heat and Ar plasma) for temperature stability test. No fluctuation in the sheet resistance values was observed

for our sample even up to a high annealing temperature (150 °C). The test temperature intentionally did not go above 150 °C, as PET itself cannot withstand temperatures above 170 °C.

We measured and compared the RMS roughness before and after annealing cycles. SEM and AFM measurements of this annealed sample indicate that the surface topography and morphology remain unchanged, as the RMS roughness values do not significantly change after annealing. The environmental stability of Ag7–Ni1 and Ag7 thin films was also investigated by damp heat (DH) test at 85 °C and 85% relative humidity. As it can be seen in Figure 5.7, the sample with Ni capping layer is electrically more stable compared to Ag thin film, which degrades quickly. However a microscope analysis reveals that, after 9-day DH, some pinholes and spots appear on the surface at the border, where oxygen and water can easily penetrate from the side of the substrate (inset Figure 5.7).

5.5 Highly transparent TiO_2/Ag/AZO multilayer TC on flexible substrate at room temperature

The TCO/metal/TCO multilayer structures work in a different manner than TCs based on single TCOs or metal thin films. The overall sheet resistance is measured in a coplanar configuration on the upper layer of the stack deposited on an insulating (glass or plastic) substrate and is mainly related to the metal film, as has been depicted in Figure 5.8, by an electric circuit with resistors representing the TCO and metal layers, where $1/R_s=1/R_{metal}+2/R_{TCO}$. Considering a typical case in which $R_{TCO}=100\ R_{metal}$, $R_s=R_{metal}/1.02\approx R_{metal}$. The overall optical transmission is controlled by destructive interference in the beams reflected from the interfaces, and constructive interference

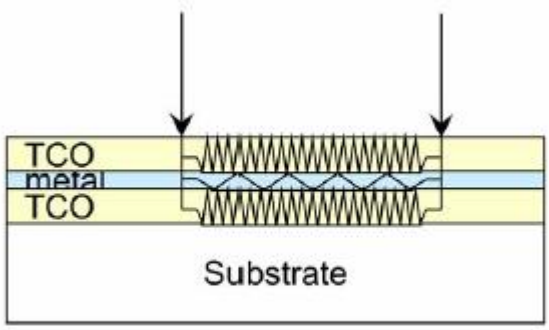

***Figure 5.8**: Schematic representation of the electrical behaviour of TCO/metal/TCO multilayer structures [1].*

in the corresponding transmitted beams through the multilayer structure and the transparent substrate.

From the literature, Ag is the most common metal interlayer for TCO/ metal/TCO TCs. Various trilayer structures with sheet resistance below 15 Ω/sq and optical transmittance above 70% are reported. All the TCO/metal/TCO structures were prepared by sputtering the TCO layers and using sputtering or evaporation for the metal interlayer, with deposition processes performed at room temperature. For the different TCOs used, sheet resistance values decreasing from 15 to 3 Ω/sq are obtained with Ag film thicknesses increasing from 8 to 20 nm, although the specific sheet resistance value depends on the deposition conditions [48-53]. In spite of the higher resistivity achieved by TCO films prepared without heating, they are useful to be applied in TCO/metal/TCO structures because the metal conductivity dominates the overall electrical performance. The TCO conductivity should be only sufficient to assure a good electrical connection between the metal film and any point on the structure surface. However, their optical characteristics are very important for the transparency of the stack. The principal mission of the TCO layers in stacked TCO/metal/TCO TCs is to increase the overall transmittance in the visible spectral range by reducing reflection from the metal surface. The limitation in the transmittance

of the metal film is mainly due to reflectance losses, and consequently it is possible to boost the transmittance by adding layers that act as antireflective coatings. The objective is to adjust the interference phenomena that take place between multiple reflections at the different interfaces to obtain the minimal value of reflectance or the maximum value of transmittance in a certain spectral band. For this purpose, TCO film thicknesses in the 30–60 nm range are commonly used and are finely adjusted to obtain maximum transmission at some specific wavelength, typically 550 nm [54], or maximum integral transmission in the visible spectral region (400–800 nm) [55].

5.5.1 Characterization of TiO_2/Ag/AZO structure onto Willow and PET

We optimized a trilayer TiO_2/Ag/AZO structure first on Corning Inc. willow glass and then we extended this investigation to PET substrate. The Ag film was capped with a thin AZO layer, which acts as an anti-reflective medium for the highly reflecting Ag layer beneath it and also protects the underneath metal from oxidation. Titanium dioxide (TiO_2) was chosen as undercoat layer and interposed between the substrate and Ag film to reduce further the reflection and correspondingly increase the transmittance. TiO_2 has good adhesion to the glass and plastic substrates [56, 57] and has many excellent physical properties such as a high dielectric constant, strong mechanical and chemical stability. Due to its high refractive index (about 2.7) and large optical transparency (negligible absorption), TiO_2 can be used as optical coatings on large area substrates for architectural, automotive and display applications and protective layers for very large-scale integrated circuits [58–60]. Besides reducing further the reflection and correspondingly increases the optical transmission of the whole trilayer TC, TiO_2 is an efficient seed layer for Ag that improves its smoothness and continuity at very low thicknesses, in this way reducing the Rs and the light scattering (haze).

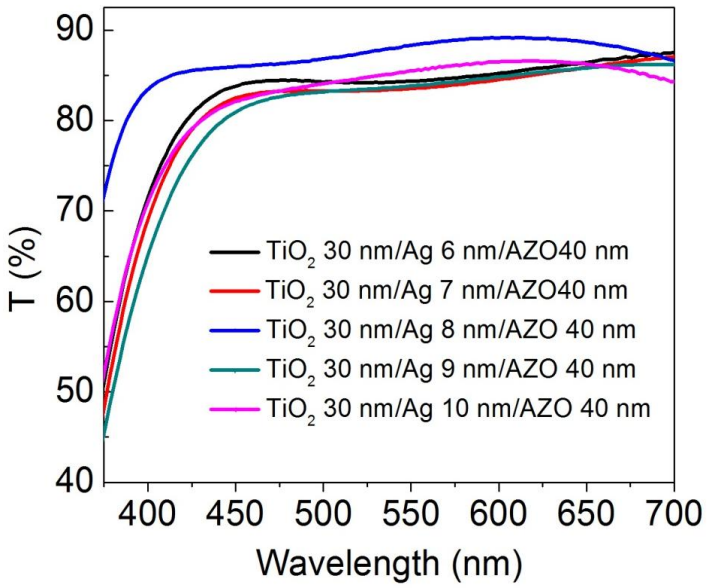

***Figure 5.9**: Optical transmittance of $TiO_2$30 nm/Ag(x)/AZO 40 nm with different Ag thicknesses.*

First we examined the effect of Ag mid-layer thickness on the opto-electrical properties of the multilayer structure. Figure 5.9 shows optical transmittance as a function of wavelength of the TC for different Ag thicknesses while keeping constant the thicknesses of TiO_2 and AZO layers, 30 nm and 40 nm, respectively. At thicknesses lower than 8 nm the Ag film is more discontinuous (more granular), giving a non-optimised antireflection effect, larger scattering and plasmonic absorption. For thicknesses larger than 8 nm the intrinsic film absorption starts dominating. There thus exists an optimum thickness (about 8 nm) corresponding to which the transmission is higher for most of the wavelength range of interest. It is worth noting that Ag films become effectively continuous for thicknesses greater than 10 nm on conventional glass substrates. Seeding the metal film growth by depositing an intermediate layer on the substrate can reduce the percolation thickness. The Ag film growing on an amorphous TiO_2 surface follows the Volmer-Weber model growth mechanism, already described in par. 2.3 of Chapter II.

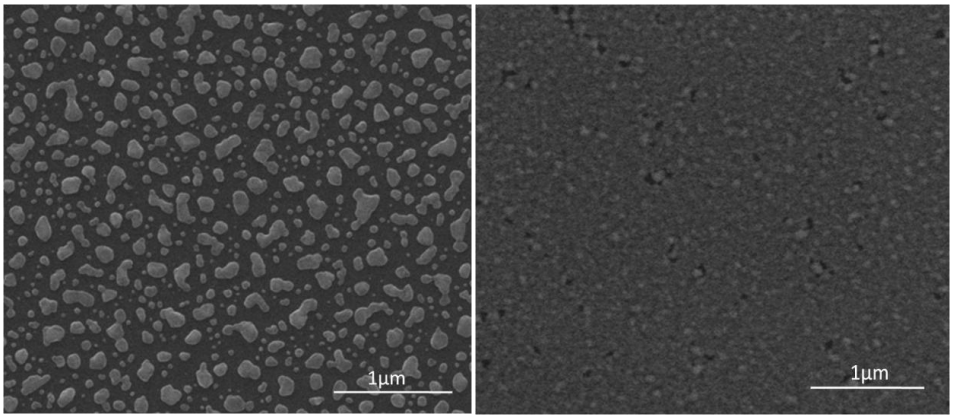

***Figure 5.10**: Top-view SEM images showing (left) 5 nm Ag film and (right) 8nm Ag deposited on 30 nm thick TiO_2 films*.

The transition from an aggregated (granular) Ag film to a continuous film was also investigated by SEM. Figure 5.10 shows the SEM images of 5 nm and 8 nm Ag film on top of the TiO_2 undercoat layer. The 5 nm thick film is discontinuous while the 8 nm thick Ag forms a continuous film. This confirms that the TiO_2 undercoat layer reduces the percolation thickness of Ag film which becomes completely continuous at 8 nm. In fact, the TiO_2 30 nm/Ag 8 nm/AZO 40 nm multilayer structure exhibits the highest transmittance (average 86%) in the 375-700 nm range, together with a very low R_S, 6 Ω/sq (Table 5.4).

***Table 5.4**: R_s and average Transmittance (T_{vis}) in the 365-700nm range of TiO_2 30nm/Ag(x)/AZO 40 nm samples for different Ag thicknesses*.

Samples	Rs [Ω/sq]	Tvis (375 nm-700 nm)
TiO_2 30 nm/Ag6 nm/AZO 40nm	9.3	82.4%
TiO_2 30 nm/Ag7 nm/AZO 40nm	7.1	81.3%
TiO_2 30 nm/Ag8 nm/AZO 40nm	6.3	86.7%
TiO_2 30 nm/Ag9 nm/AZO 40nm	5	80.5%
TiO_2 30 nm/Ag10 nm/AZO 40nm	4.2	82.2%

Considering that in our case R_{AZO}, $R_{TiO_2} \gg R_{Ag}$, the overall R_S is mainly given by the Ag film. By keeping constant the Ag and AZO thicknesses at 8 and 40 nm, respectively, we optimised the TiO_2 bottom layer thickness, by varying it from 23 nm to 46 nm. From Figure 5.11 and Table 5.5 one can see that 34 nm TiO_2 undercoat layer provided the optimum transmission (average of 87.66%).

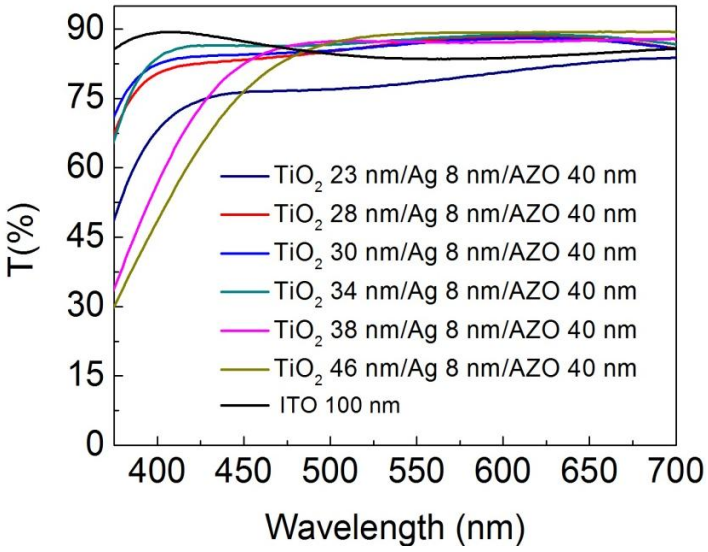

***Figure 5.11**: Optical transmittance spectra of TiO_2(x)/Ag 8 nm/AZO 40 nm with different TiO_2 thicknesses, compared with the optical spectrum of commercial 100 nm ITO.*

***Table 5.5**: Average Transmittance of various TiO_2(x)/Ag 8 nm/AZO 40 nm films.*

Samples	Tvis (375 nm-700 nm)	Samples	Tvis (375nm-700nnm)
TiO_2 23 nm/Ag 8 nm/AZO 40nm	78.4%	TiO_2 46 nm/Ag8nm/AZO 40 nm	81.8%
TiO_2 28 nm/Ag 8 nm/AZO 40nm	86.3%	ITO 100 nm	84.9%
TiO_2 30 nm/Ag 8 nm/AZO 40nm	86.6%		
TiO_2 34 nm/Ag 8 nm/AZO 40nm	87.7%		
TiO_2 38/Ag 8 nm/AZO 40nm	82.4%		

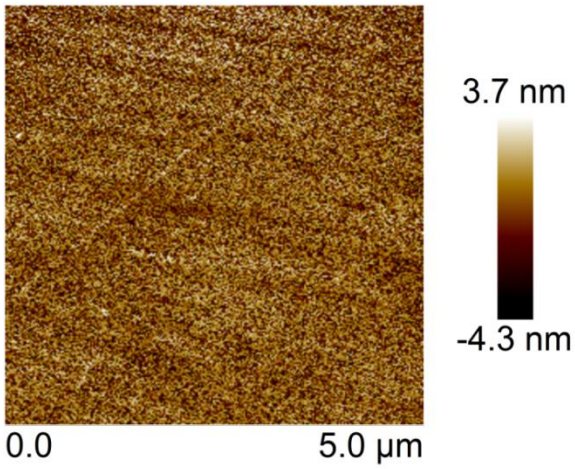

***Figure 5.12**: AFM micrograph of a TiO_2 34 nm/Ag 8 nm/AZO 40 nm film imaging 5×5 μm^2 area of the film surface.*

Since the TiO_2/Ag/AZO based TC is supposed to be used as bottom electrode in OSC devices, the surface roughness of this structure must be low to avoid electrical shorts. Figure 5.12 displays an AFM image of the multilayer structure. The roughness is 1.3 nm root mean square (RMS), which is suitable for use as TC in OSCs [61].

Afterwards we took into account even the influence of the PET substrate on the optimum TiO_2 thickness. In Figure 5.13 we report some optical spectra of the prepared samples on PET which have almost the same trend as willow glass substrates but lower transmittance values.

Before depositing the OSC's layers, annealing steps are usually employed to obtain an optimum morphology of the blend which improves the cell's performance. In this case the proposed TC was subjected to annealing treatment from room temperature up to 150 °C for 10-15 min to evaluate its thermal stability. No measurable variations were observed in the optical transmission

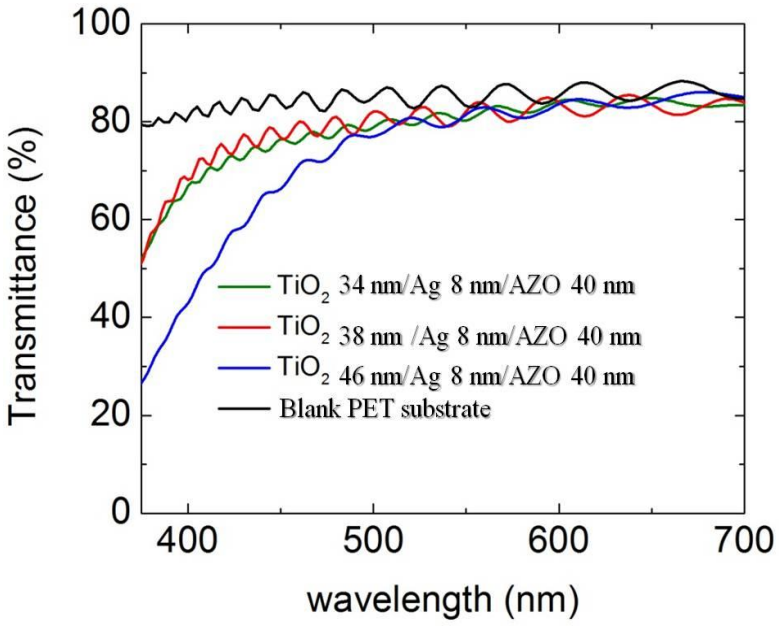

***Figure 5.13**: Comparison of optical transmittance spectra obtained from the TiO_2(x)/Ag(8)/AZO(40) multilayer on PET substrates as a function of the TiO_2 thickness.*

and sheet resistance of the multilayer, confirming that AZO films as thin as 30-40 nm act as excellent protective barrier for the underlying Ag.

Multilayer TCO/metal/TCO TCs were also found to be sensitive to atmosphere and environmental changes, especially moisture. Discoloration spots have been detected in our samples when exposed to DH at 85°C and 85 % relative humidity. As it can be seen in figure 5.14 which shows the sheet resistance variation as function of the DH time, the electrical properties remain unchanged during almost 1 week and the sample started degrading significantly after 10 days. The moisture induced degradation is responsible of the formation of spots. The worsening of the TCO/Ag/TCO characteristics is caused by the agglomeration of the Ag layer, whose surface diffusivity is controlled not only by temperature and humidity but even by the surrounding layers, the substrate, and particulate contamination on the surface [62].

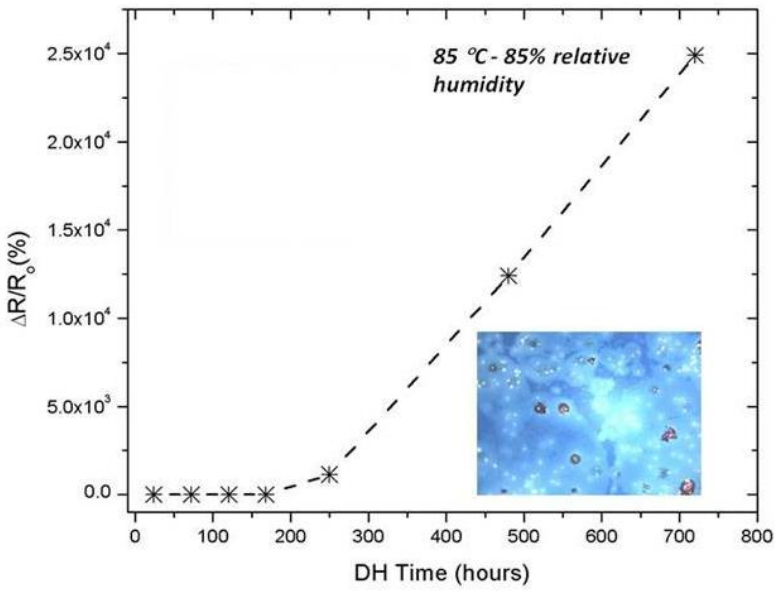

Figure 5. 14*: Sheet resistance variation as function of Damp Heat (DH) time for TiO_2 34 nm/Ag 8 nm/ AZO 40 nm samples. The inset shows the degradation of the samples surface observed by an Optical Microscope.*

To estimate the adhesion of the structure to the substrate, we carried out pull-tests using standard tape. The test is highly qualitative, but allows screening films involving poor adhesion from those where adhesion is acceptable. For all the tested samples the structure always remains on the surface practically unaltered, indicating good adhesion to the substrate.

5.6 Flexibility tests

Flexible electronic devices require that the TCs are stable during bending and unbending cycles.Evolution of the sheet resistance as a function of the substrate curvature radius or increasing tensile strain are commonly used indicators for the practical design of reliable devices on flexible substrates.

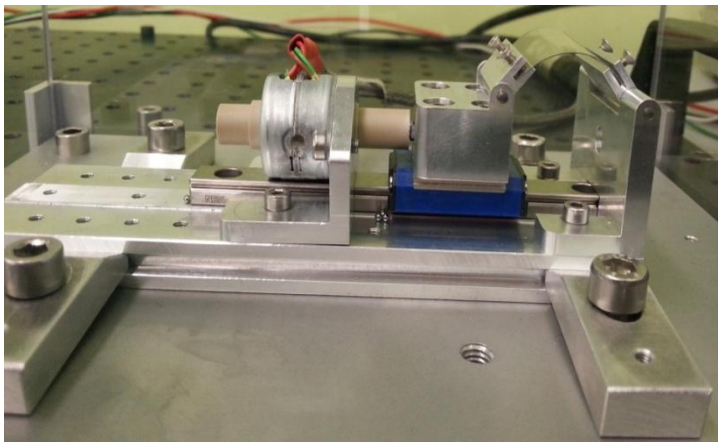

Figure 5.15*: Set-up showing the bending apparatus*.

To study the flexibility properties of our TCs, a set-up as shown in Figure 5.15 was developed.

The film to be analyzed is deposited onto 1 × 1 inch flexible PET substrate and is mounted onto the clips with two of its ends fixed. The set-up is connected to a motor which in turn is controlled by an electronic controller which moves the arm in the horizontal direction. The cycling movement – back and forth translation - of the arm results in bending of the sample, with a minimum radius of curvature of 4 mm and maximum of 12 mm. The R_S value and transparency of the TC is measured before and after a finite number of bending cycles**.**

Figure 5.16 shows the variation of the sheet resistance of the best Ag-AZO structure, described in **Chapter III**, as a function of the number of bending cycles, compared to state-of-art 100nm-thick ITO. It has been observed that the electrical properties of Ag(11)/AZO(30) are very stable (constant R_s) even after 10^4 bending cycles while the R_s of ITO increases to 1580% after only 20 cycles.As mentioned before, ductile Ag conductive layer beneath the AZO in our proposed structure helps in retaining the electrical properties after bending [63].

As it can be seen in the SEM images of the ITO and Ag(11)/AZO(30) films before and after bending test shown in figure 5.17, cracks were formed in the case of ITO while no observable degradation in surface morphology is found in the case of Ag(11)/AZO(30).

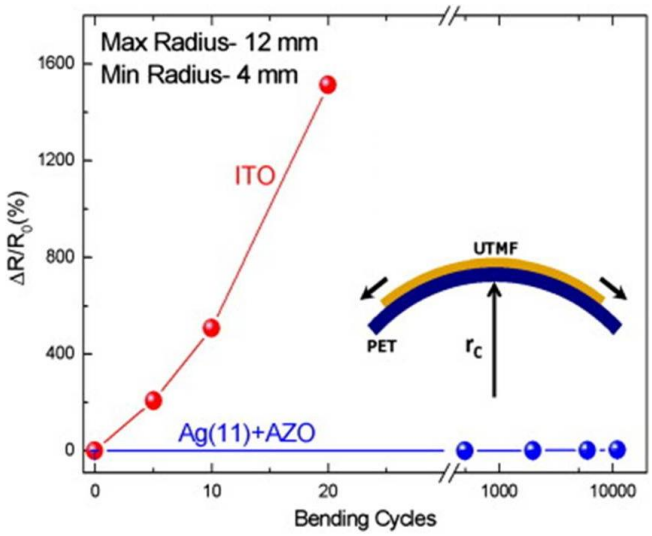

***Figure 5.16**: Sheet resistance change after bending as a function of bending cycles for Ag(11)/AZO(40) and ITO on PET.*

Electrical measurements performed for ITO films deposited on PET reveals the existence of a critical strain for which the resistance starts to increase dramatically because the conductive layer fails mechanically.

Even for the optimized TiO_2/Ag/AZO multilayer TC a constant R_s trough thousands of bending cycles was observed on 1inch×1inch PET and large size, 3 inch×5inch, Corning Inc. Willow glass demonstrating the robustness of the TC structure on any flexible substrate. Compared to single TCO layer based TC the high flexibility of the proposed multilayer is related to the presence of the ductile Ag interlayer between TiO_2 and AZO.

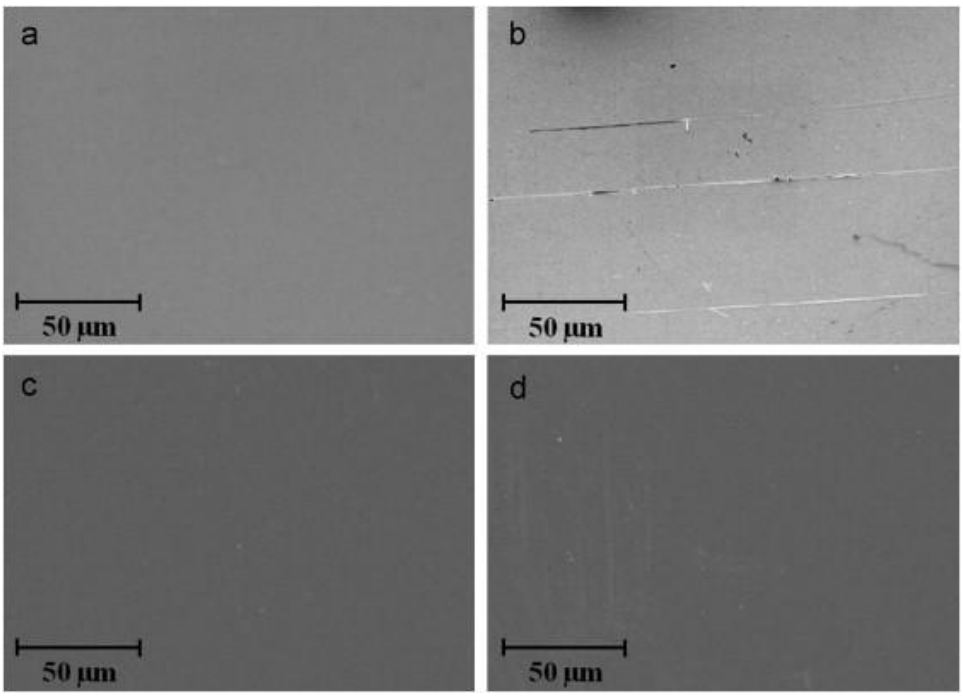

Figure 5.17*: SEM images of the ITO and Ag(11)/AZO (30) films on PET before and after bending: (a) ITO before bending (b) ITO after 20 bending cycles (c) Ag(11)/AZO(30) before bending (d) Ag(11)/AZO(30) after* 10^4 *bending cycles.*

References

[1] C. Guillen, J. Herreo, Thin Solid Films 520, 1, 2011.

[2] J. A. Jeong, Y. S. Park, and H. K. Kim, J. Appl. Phys. 107, 023111, 2010.

[3] S. H. Choa,C. K. Cho,W. J. Hwang, K. Tae Eun and H. K. Kim, Sol. Energy Mater. Sol. Cells 95, 3442, 2011.

[4] J. A. Jeong and H. K. Kim, Sol. Energy Mater. Sol. Cells 93, 1801, 2009.

[5] H. K. Park, J. W. Kang, S. I. Na, D. Y. Kim and H. K. Kim, Sol. Energy Mater. Sol. Cells 93, 1994, 2009.

[6] T. Dimopoulos, G. Radnoczi, Z. Horvàth and H. Brückl, Thin Solid Films 520, 5222, 2012.

[7] J. Montero, C. Guillèn and J. Herrero, Thin Solid Films 519 7564, 2011.

[8] D. Sahu, C. Chen, S. Lin and J. L. Huang, Thin Solid Films 515, 932, 2006.

[9] William S. Wong, Alberto Sallueo Editors, Springer, Flexible electronics: materials and applications.

[10] W. A. MacDonald, M.K. Looney, D. Mackewon, R. Eveson, R. Adam, K. Hashimoto, K. Rakos, Journal of the SID, 15,12, 2007.

[11] Flexible flat Panel displays Editor Gregory P. Crowford Wiley and Sons, Ltd. 2005.

[12] J. S. Lewis, Weaver MS (2204) IEEE Selected top Quantum Electron 10:45-57.

[13] www.dupont.com

[14] www.corning.com

[15] A. Yoshida, S. Fujimura, T. Miyaka, T. Yoshizawa, H. Ocho, A. Sugimoto, H. Kubota, T. Miyadera, S. Ishizuka, M. Tsuchida and H. Nakada, Proc. Soc. Infor. Display Symp. Dig. Tech. papes, 34, 856, 2003.

[16] E. Lueder, Electrochem. Soc. Proc. 98-22, 336, 1998.

[17] B. M. Henry, F. Dinelli, K–Y. Zhao, C.R. M. Grovenor, O. V. Kolosov, G. a. D. Briggs, A. P. Roberts, R.S. Kumar and R. P. Howson, Thin Solid Film 355, 500, 1999.

[18] www.vitexsys.com

[19] M.R. Wertheimer, L. Martinu& E.M. Liston, in Plasma Sources for Polymer Surface Treatment, part E3.0. of Handbook of Thin Film Process Technology, edited by D.A.

Glocker and S.I. Shah, Institute of Physics Publishing, Bristol, UK and Philadelphia, USA (1995).

[20] L.J. Gerenser, in Surface Chemistry of Plasma-Treated Polymers, part E3.1. of Handbook of Thin Film Process Technology, edited by D.A. Glocker& S.I. Shah, Institute of Physics Publishing, Bristol, UK and Philadelphia, USA (1995). [21] E. Arenholz, J. Heitz, M. Wagner, D. Bäuerle, H. Hibst& A. Hagemeyer, Appl. Surf. Sci. 69, 16, 1993.

[22] W. Wong, K. Chan, K.W. Yeung& K.S. Lau, J. Mater. Process.Technol. 6020, 1, 2002.

[23] Y. Han, D. Kim, J.-S.Cho, Y.-W.Beag& S.-K.Koh, Thin Solid Films 496, 58, 2006.

[24] Y. Leterrier, Prog. Mater.Sci. 48, 1, 2003.

[25] S. Petit, P. Laurens, J. Amouroux& F. Arefi-Khonsari, Appl. Surf. Sci. 168, 300, 2000.

[26] S. Tamulevičius, Vacuum 51, 127, 1998.

[27] Y. Leterrier, Prog. Mater.Sci. 48, 1, 2003.

[28] P. F. Carcia, R.S. McLean, M.H. Reilly, Z.G. Li, L.J. Pillione, R.F. Messier, J. Vac. Sci. Technol. A 21, 745, 2003.

[29] F.L. Wong, M.K. Fung, S.W. Tong, C.S. Lee, S.T. Lee, Thin Solid Films 466, 225, 2004.

[30] C. Koidis, S. Logothetidis, S. Kassavetis, A. Laskarakis, N.A. Hastas, O. Valassiades, , Phys. Status Solidi A 207, 1581, 2010.

[31] B. Sim, E.H. Kim, J. Park, M. Lee, Surf. Coat.Technol. 204, 309, 2009.

[32] B. Sim, H. Hwang, S. Ryu, H. Baik, M. Lee, Jpn. J. Appl. Phys. 49, 060205, 2010.

[33] Y.S. Park, K.H. Choi, H.K. Kim, J. Phys. D: Appl. Phys. 42, 235109, 2009.

[34] K.H. Choi, H.J. Nam, J.A. Jeong, S.W. Cho, H.K. Kim, J.W. Kang, D.G. Kim, W.J. Cho, Appl. Phys. Lett. 92, 223302, 2008.

[35] J. Lewis, S. Grego, B. Chalamala, E. Vick, D. Temple, Appl. Phys. Lett. 85, 3450, 2004.

[36] J.W. Seo, J.W. Park, K.S. Lim, S.J. Kang, Y.H. Hong, J.H. Yang, L. Fang, G.Y. Sung, H.K. Kim, Appl. Phys. Lett. 95, 133508, 2009.

[37] D. Kim, Appl. Surf. Sci. 256, 1774, 2010.

[38] J.Y. Lee, J.W. Yang, J.H. Chae, J.H. Park, J.I. Choi, H.J. Park, D. Kim, Opt. Commun. 282, 2362, 2009.

[39] D. Kim, J. Alloys Compd. 493, 208, 2010.

[40] Yong Xiang, Teng Li, ZhigangSuo, and Joost J. Vlassak a) Appl. Phys. Lett. 87, 161910 2005.

[41] S. Cheylan, D.S. Ghosh. D. Krautz, T.L. Chen, V. Pruneri, Organic Electronics 12, 818, 2011.

[42] A.I. Maaroof, B.I. Evans, Journal of Applied Physics 76, 1047, 1994.

[43] K. Seal, M.A. Nelson, Z. C. Ying, D.A. Genov, A.-K.Sarychev, V.M. Shalev, Physical Reviw B 67, 0353183, 2003.

[44] N. Marechal, E. Quesnel, Y. Pauleau, Journal of Vacuum Science and Technology A 12, 707, 1994.

[45] M.S. Islam, Z. Li, S.C. Chang, D.A.A. Ohlberg, D. R. Stewart, S. Y. Wang, R.S. Williams, Proceedings of he IEEE Conference Nanotechnology, 5th IEEE, Angoya, Ajpan, 80, 983, 2005.

[46] S.T.M. Neddermeyer, Critical Reviews in solid State Materials Science 16, 309-335, 1990.

[47] S. Kundu, S. Hazre, S. Bonerjee, M.K. Sanyal, S.K. Mandal, S. Chandhuri, A.K. Pal, Journal of Physics D: Applied Physics 31, L73, 1998.

[48] M. Chakaroun, B. Lucas, B. Ratier, C. Defranoux, J.P. Piel, M. Aldissi, Thin Solid Films 518, 1250, 2009.

[49] Y. Abe, T. Nakayama, Mater. Lett. 61, 3897, 2007.

[50] A. Indluru, T.L. Alford, J. Appl. Phys. 105, 123528, 2009.

[51] S.H. Mohamed, J. Phys. Chem. Solids 69, 2378, 2008.

[52] S. Song, T. Yang, Y. Xin, L. Jiang, Y. Li, Z. Pang, M. Lv, S. Han, Curr. Appl. Phys. 10, 452, 2010.

[53] M. Bender, W. Seelig, C. Daube, H. Frankenberger, B. Ocker, J. Stollenwerk, Thin Solid Films 326, 67, 1998.

[54] A. Klöppel, W. Kriegseis, B.K. Meyer, A. Scharmann, C. Daube, J. Stollenwerk, J. Trube, Thin Solid Films 365, 139, 2000.

[55] H. Han, N.D. Theodore, T.L. Alford, J. Appl. Phys. 103, 013708, 2008.

[56] K. Koike, S. Fukuda, J. Vac. Sci. Technol. A 26, 444, 2008.

[57] M. Bender, W. Seelig, C. Daube, H. Frankenberger, B. Ocker, J. Stollenwerk, Thin Solid Films 326, 67-71, 1998.

[58] I. Dima, B. Popescu, F. Iova, and G. Popescu, Thin Solid Films 200, 11, 1991.

[59] C. H. Heo, S.-B. Lee, and J.-H. Boo, Thin Solid Films 475, 183, 2005.

[60] K. Hashimoto, H. Irie, and A. Fujhishima, Jpn. J. Appl. Phys. 44, 8269, 2005.

[61] Hans Schmidt et al. Energy Procedia 31, 110, 116 113, 2012.

[62] E. Ando, M. Miyazaki, Thin Solid Films 351, 308, 1999.

[63] B.Sim,E.H.Kim,J.Park,M.Lee, Surface and Coatings Technology 204, 309, 2009.

Chapter VI

Organic Photovoltaics

This chapter starts with an overview on different renewable energy sources, with particular attention to solar power and, more specifically, to the potential of organic photovoltaics (OPV) technology. The physical mechanisms of the organic photovoltaic devices and the most commonly used materials are described. Finally, the performance of OPV devices employing UTMFs based TCs are discussed and compared with that of ITO based devices.

6.1 World energy consumption and solar energy

In 2012, oil, gas, and coal accounted for 87.1% of global primary energy use while nuclear power for 4.9%. Renewable sources only contributed to 8 %, whose 6.4% coming from hydropower [1]. The strong dependence on fossil fuels of the world energy consumption causes a detrimental environmental impact due to CO_2 emissions which contributes to global warming. To minimize the impact on the environment, the increase of renewable sources becomes a must and, for achieving this, their development has to be considered a worldwide priority.

The most widely used renewable energy source is hydropower. Its potential production of energy per year has been estimated around 1194 Milion tonnes of oil equivalent (Mtoe). Latin America is the first country using this energy at the largest scale with 26% of the total energy consumption supplied by hydropower. [2]. However, this energy largely depends on the local natural resources and that makes it a very limited source for many other countries. Additionally, this technology implies some negative consequences on the environment mostly because of the need to build dikes which imply deforestation.

The other renewable energy sources, i.e. solar, wind, geothermal and biomass, last year provided 1.6% of the total global energy consumption [1]. During 2011 the entire renewable energy sector experienced a 17.7% annual growth rate, which was the largest one, followed by a 5.4% of the non-

renewable energy based on coal. All these different alternative energy sources have an enormous potential for power generation which has been estimated in 14.330 Mtoe for wind, 11.942 Mtoe for geothermal, 5.972 Mtoe for biomass and 38.215 Mtoe for solar per year [2].

Solar power is one of the most promising renewable energy sources and at the same time is one of the least exploited. As indicated above, this kind of energy alone has the potential to produce 38.215 Mtoe [2] per year, which is more than three times the global energy consumption in 2011. Additionally, its production and distribution is environmentally friendly. According to Figure 6.1 of the National Renewable Energy Laboratory [3], the most efficient solar device to date exhibits a power conversion efficiency (PCE) of 44.0%. From the emerging photovoltaic technologies, the top efficiency obtained for an organic (tandem) solar cell is 10.6%. This performance has shown a 16% average growing rate over the last years.

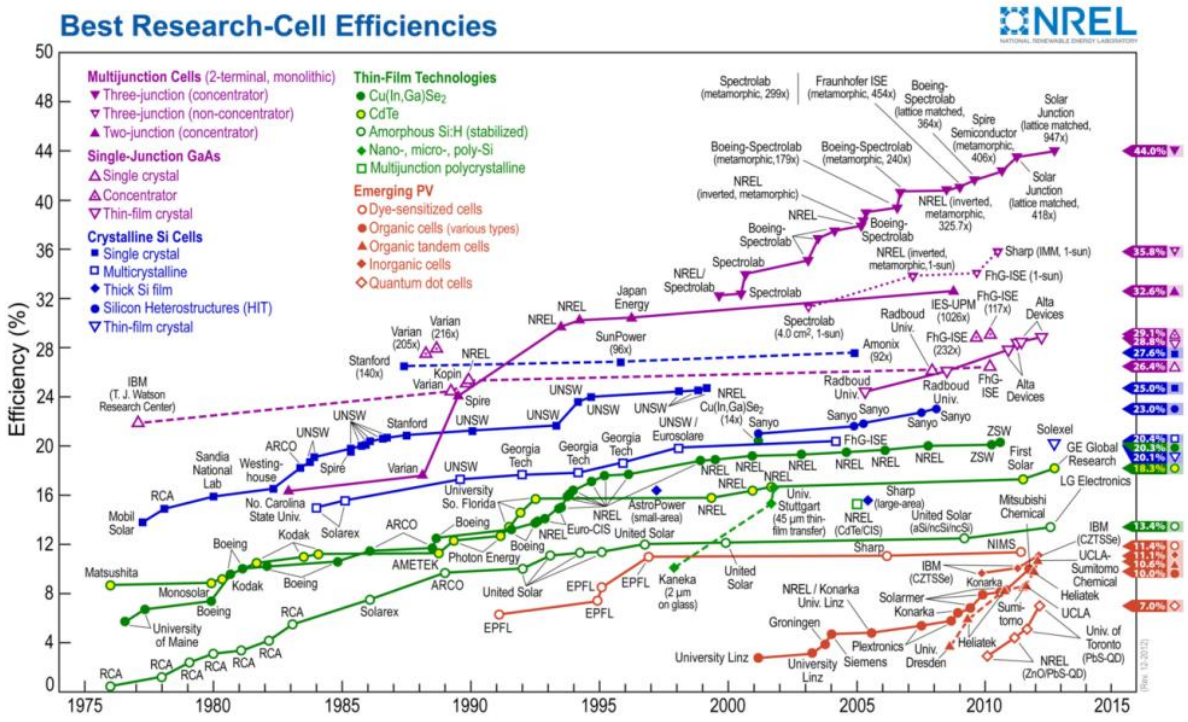

***Figure 6.1**: Best solar devices certified by NREL [3]*

Organic photovoltaics has many attractive features, including

- the potential to be flexible and semitransparent,
- potential to be manufactured in a continuous printing process,
- large area coating, easy integration in different devices,
- significant cost reduction compared to traditional solutions,
- substantial ecological and economic advantages.

6.2 Basics of the organic solar cells

Organic solar cells (OSCs) essentially comprise the following layers: first electrode, electron transport layer, photoactive layer, hole transport layer, and second electrode. In general, a solar cell absorbs light, separates the created electrons and holes from each other and delivers electrical power at the contacts. The fundamental difference between the working principles of organic and inorganic solar cells is the direct generation of free charge carries in the inorganic solar cells. In organic materials the light absorption is followed by the creation of excitons with a typical binding energy (due to coulomb-interaction) of 0.3-0.5 eV. After its generation, the exciton starts to diffuse in the active material. Its lifetime is about 0.5 ns [4] which is equivalent to a diffusion length of about 20 nm [5]. During this period the exciton needs to split into charges, otherwise a recombination process, radiative or non-radiative, would take place. The morphology of the active layer is fundamental for preventing this energy loss. Due to the small exciton diffusion length, the donor and acceptor materials which form the absorbing or photoactive layer can be mixed together to minimize the distance an exciton must travel to reach a donor / acceptor interface. This structure is called a bulk heterojunction since the heterojunction is dispersed throughout the bulk of the layer. In this sense, the morphology of this heterojuction blend is very important, as percolation pathways for the holes and electrons through donor and acceptor phases to the correct electrode are necessary. The splitting into separated electron and hole charges takes place when the exciton reaches the donor-acceptor interface. Afterwards, the charges travel in their corresponding semiconducting

buffer layer named electron transporting layer (ETL), also known as hole blocking layer, and hole transporting layer (HTL), also known as electron blocking layer, which must also block excitons for preventing recombination. Finally, such buffer layers are connected to the electrodes (anode and

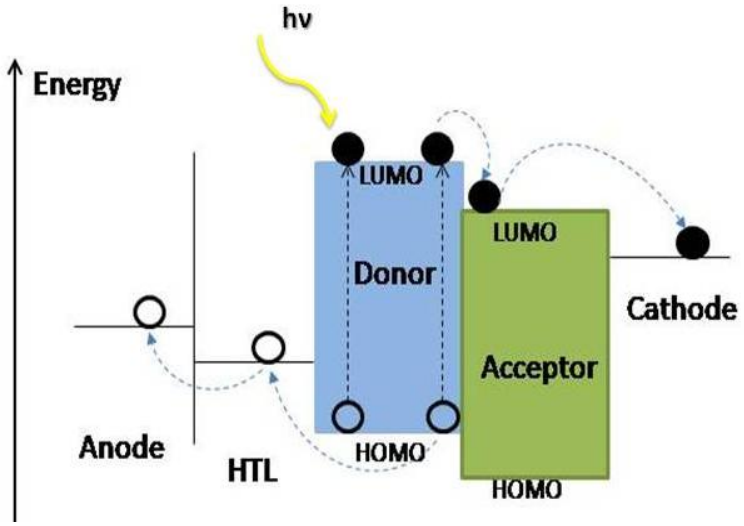

***Figure 6.2**: Fundamental mechanism of the photon-to-electron conversion process in bulk heterojunction solar cells*.

cathode) to extract the charges. Such connection depends on the work function of the electrode and the corresponding valence or conduction band, called HOMO (Highest Occupied Molecular Orbitals) and LUMO (Lowest Unoccupied Molecular Orbitals) levels, of the ETL or HTL, respectively. Figure 6.2 illustrates the fundamental steps involved in the photon to electron-hole (exciton) conversion mechanism for OSCs.

Several materials and device architectures have been implemented in the OSCs field. At the interface between the active layer and the electrodes the most commonly used HTL is PEDOT. Several alternatives have been found such as molybdenum oxide (MoO_3), nickel oxide (NiO) and tungsten oxide (WO_3) [6–11]. For the complementary buffer layer, that is the electron transporting layer (ETL), several materials have also been developed, for instance lithium fluoride (LiF), Anatase titanium oxide (TiO_2) , zinc oxide ZnO, bathocuproine (BCP) and poly [(9,9-bis(3′-(*N*,*N*-dimethyla-mino) propyl)-2,7-fluorene)- *alt* -2,7-(9,9–dioctylfluorene)] (PFN). Sometimes metals as

calcium of ytterbium are also employed [12-16]. As electrode ITO is the most commonly used but there are other alternatives such as AZO, FTO and thin metallic layers made of copper, nickel and silver [8,17–19].

For the donor materials probably the most commonly used one is the Poly(3-hexylthiophene) (P3HT) which can be used to fabricate devices with efficiencies that are typically between 3 and 5%. Recently new low-bandgap donor materials have been developed such as for instance Poly[[9-(1-octylnonyl)-9H-carbazole-2,7-diyl] -2,5-thiophenediy l-2,1,3-benzothiadiazole-4,7-diyl-2,5-thiophenediyl] (PCDTBT), Poly[4,8-bis-substituted-benzo[1,2-b:4,5-b0]dithiophene-2,6-diyl-alt-4-substituted-thieno[3, 4-b]thiophene-2,6-diyl] (PBDTTT) and Poly[[4,8-bis[(2-ethylhexyl)oxy]-benzo[1,2-b:4,5-b'] dithiophene-2,6-diyl] [3-fluoro-2-[(2-ethyl-hexyl)carbonyl]thieno[3,4-b]thiophe-nediyl]] (PTB7) which has allowed to fabricate single junction OSCdevices with efficiencies above 8% [12-13,20-21]. On the other hand, the most efficient known acceptor materials are the fullerene and fullerene derivatives particularly [6,6]-Phenyl-C61-butyric acid methyl ester $PC_{61}BM$ and [6,6]-Phenyl-C71-butyric acid methyl ester $PC_{71}BM$ [12,21].

Depending on the type of charges collected by the semi-transparent electrode through which the sunlight enters the device, two types of cell configurations can be defined: *direct* if the collected charges by such electrode are holes and *inverted* if those carriers are electrons. A scheme of such devices is shown in Figure 6.3.

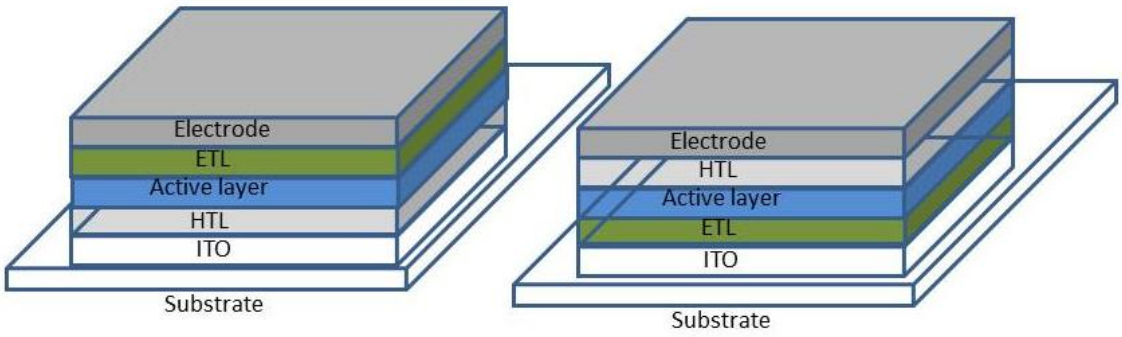

Figure 6.3*: Device structures of a) standard direct solar cell and b) inverted solar cell*.

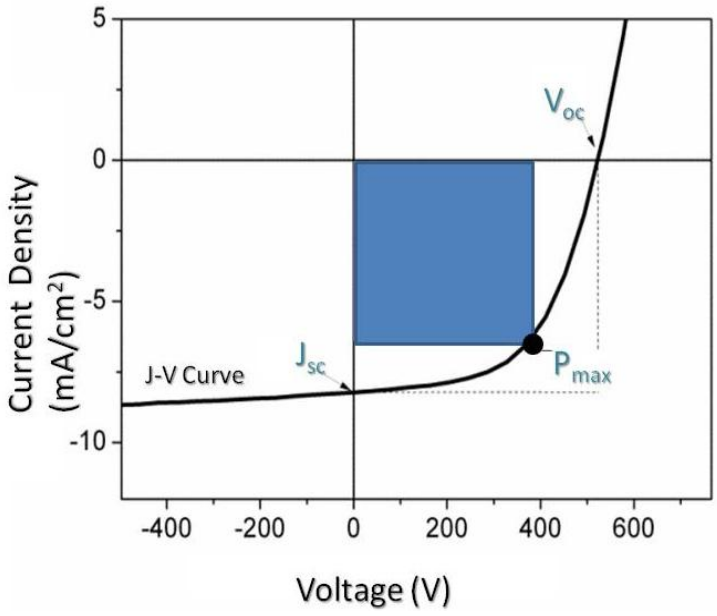

***Figure 6.4**: Example of a typical J-V curve of a photovoltaic device.*

The electrical characterization of a solar device is achieved with a Current density – Voltage curve commonly named J-V or I-V curve as the one shown in Figure 6.4.

The most discussed performance parameters that can be found from the J-V curve of a device under a known illumination source are open-circuit voltage (V_{oc}), short-circuit current density (J_{sc}), fill factor (FF), and power conversion efficiency (PCE) [22].

Open-circuit voltage

The open-circuit voltage (V_{oc}) is the voltage at which no current flows through the external circuit. It is the maximum voltage that a solar cell can deliver. The V_{oc} corresponds to the forward bias voltage, at which the dark current compensates the photo-current. The V_{oc} depends on the saturation current of the solar cell and the photo-generated current. The saturation current density depends on the recombination in the solar cell. Therefore it is a measure of the amount of recombination in the device.

Short-circuit current density

Similar to V_{oc}, the short-circuit current density (J_{sc}) is the current density when V = 0, which is the same condition as the two electrodes of the cell being short-circuited together. Again, there is no power produced at this point, but the J_{sc} does mark the onset of power generation. In ideal devices, the J_{sc} will be the same as the photocurrent density (J_{ph}). However, several effects such as surface recombinations can lower the J_{sc} from this ideal value. Although J_{sc} is technically a negative number with the conventions used here, discussions of different J_{sc} values will focus primarily on the magnitude of the value and treat it as a positive number, e.g., a higher J_{sc} corresponds to a higher J_{ph}.

Fill-factor

The Fill factor FF is a parameter which in conjunction with V_{oc} and J_{sc} determines the maximum power P_{max} from a solar cell. P_{max} occurs at the voltage V_{max} and current-density J_{max} where the product of J and V is at a minimum (or maximum in absolute value), as shown in Figure 6.4. The fill factor FF is defined as:

$$FF = \frac{P_{max}}{J_{sc}\, V_{oc}} = \frac{J_{max} V_{max}}{J_{sc}\, V_{oc}} \tag{6.1}$$

FF is an indication of how close J_{max} and V_{max} come to the boundaries of power production of J_{sc} and V_{oc} and also an indication of the sharpness of the exponential J-V curve that connects J_{sc} and V_{oc}. Since higher FF is related to higher maximum power, high FF is desired; however, the diode-like behavior of solar cells results in FF always being less than one.

Power conversion efficiency

The power conversion efficiency (PCE) is defined as the percentage of incident irradianceI_L (light power per unit area) that is converted into output power. Because the point where the cell operates on the J-V curve changes depending on the load, the output power depends on the load. For consistency, the maximum output power is used for calculating PCE using the following equation:

(6.2) $$PCE = \frac{|J_{max}|V_{max}}{I_l} \times 100\% = \frac{FF \times |J_{sc}|V_{oc}}{I_L} \times 100\%$$

this clearly shows that FF, J_{sc} , and V_{oc} all have direct effects on PCE. Furthermore, the area used to calculate J can affect PCE and should include inactive areas that are integral to the solar cell, such as grids and interconnections for large area devices or modules.

PCE is important since it determines how effectively the space occupied by a solar cell is being used and how much area must be covered with solar cells to produce a given amount of power. Since larger areas require more resources, higher PCE is very desirable. However, there are trade-offs between $PCE\eta$ and cost for each solar cell technology.

PCE is also very dependent on the power and spectrum of the light source since solar cells do not absorb and convert photons to electrons at all wavelengths with the same efficiency. To draw comparisons between various solar cells, a standard spectrum must be chosen for the calculation of PCE.

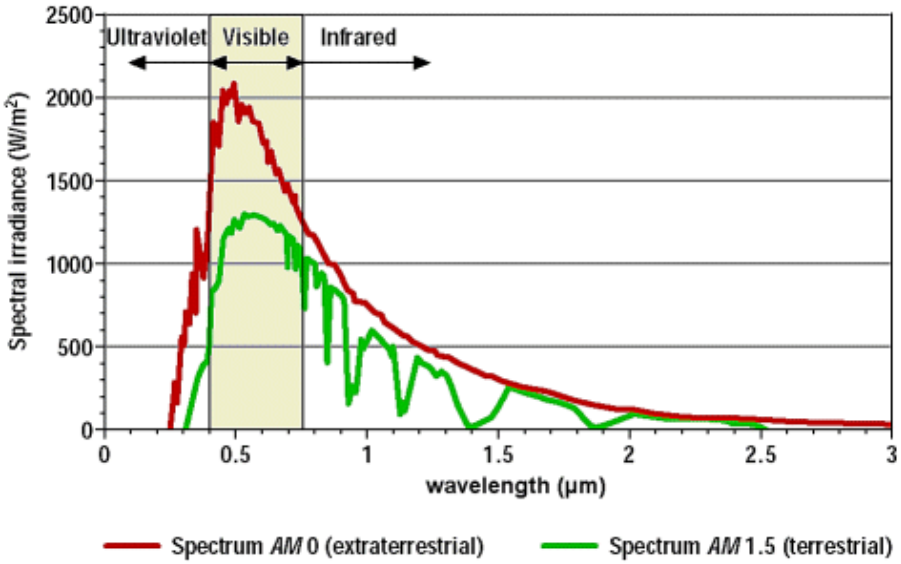

***Figure 6.5**: Solar Spectra Irradiation [23].*

Although the spectrum of the sunlight at the earth's surface varies with location, cloud coverage, and other factors, the AM1.5 G spectrum in Figure 6.5 is the most commonly used standard

spectrum for measuring and comparing the performance of solar cells that are intended for outdoor use. Because of difficulties recreating this exact spectrum in the laboratory with standard lamps, PCE measurements must often be corrected based on the external quantum efficiency.

External quantum efficiency

The external quantum efficiency (EQE) of a device is the fraction of incident photons converted into current and depends on wavelength. One reason for the wavelength dependence is that the absorption in the active layers is a function of wavelength. Another reason, especially in inorganic solar cells, is that the location where a photon is absorbed in a device can also affect the probability of the resulting charges being collected or recombining and being lost.

The J_{sc} expected under a light source can be estimated from the EQE and the spectral irradiance of the light source by integrating the product of the EQE and the photon flux density. For the standard AM1.5 G spectrum, the calculation is

$$J_{sc} = \int_0^\infty e\, EQE(\lambda) \frac{\lambda}{hc} E_\lambda^{AM1.5\,G}(\lambda) d\lambda \tag{6.3}$$

where AMG E .5 1 λ is the spectral irradiance of the AM1.5 G spectrum, λ is the wavelength, h is Planck's constant, c is the speed of light, and e is the elementary charge. If the EQE was measured at low light intensities, then this calculation will only be accurate if the short-circuit current density is a linear function of irradiance, as is expected for ideal devices. Otherwise, EQE must be measured with a dc bias light source that generates a photocurrent in the device similar to what is expected under AM1.5 G.

In the following paragraphs we demonstrate that the UTMF based TCs described in the previous chapters are competitive electrodes to realize OSCs with efficiency comparable to that of ITO.

6.3 Integration of Cu-Ag alloy Transparent Conductors into OSC device

In collaboration with Jaehyung Hwang and Ingmar Bruder from BASF-The Chemical Company, the

developed alloy TC has been used in OSCs. The OSC had the following configuration: Anode/MoO_3(5 nm)/ID529 [Fullerene]:C60(1:1,35 nm)/C60(25 nm)/Bphen (5 nm)/Ag (100 nm)

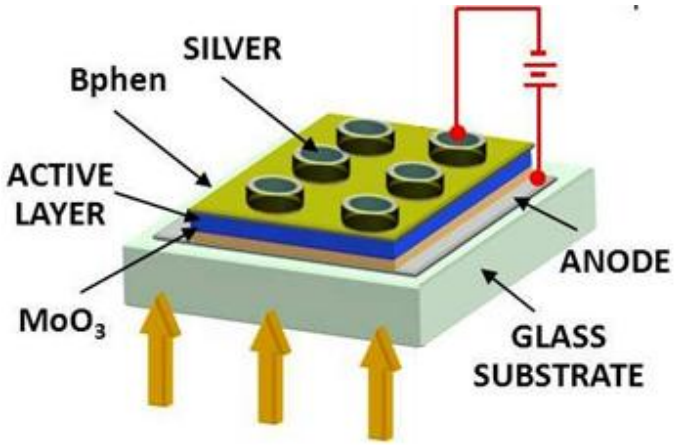

***Figure 6.6**: Device Structure of the OSC with Alloy/Ni TC as anode*.

(Figure 6.6). Devices incorporating standard ITO and single component Cu and Ag were also made for comparison (the reference used is a standard ITO, 100nm thick with 17–21 Ω/sq and T>85%). The ITO substrates were ozone-treated for 10 min. Afterwards, the different layers were deposited under high vacuum conditions (3.8×10^{-0} mbar) by sublimation in a commercially available evaporation chamber (Kurt J. Lesker Company) through a shadow mask. The evaporation temperature of the ID529 material was 220 °C. The photovoltaic *I–V* measurements were evaluated under simulated AM1.5G sunlight illumination. The intensity was monitored by a Si diode that is calibrated using a certified reference diode from the Fraunhofer ISE CalLab. The electrical characterization data are summarized in Table 6.1. The cells incorporating alloy and ITO TCs showed almost the same efficiency. The higher transmittance of ITO TC is compensated by the microcavity effect which is strongly prevalent in alloy based devices due to its higher reflectance in the visible region (>21% compared to ~9% for ITO) [24]. It has been found that the optical resonance effect of the microcavity effect developed between the semi-transparent alloy anode and

top Ag cathode leads to enhanced optical electrical field in the ITO free devices, which ultimately leads to an enhanced optical absorption in the active layer. Besides this lower sheet resistance together with higher work function of the Ni capped alloy TCs also plays a crucial role for lowering the injection barrier. The latter is nicely reflected in the higher open circuit voltage of the alloy/Ni electrode compared to the ITO device. The active area of the fabricated cell was 0.07 cm^2. The error

***Table 6.1**: List of electrical characterization data for the OSCs incorporating alloy and ITO TCs.*

	J_{sc} (mA/cm^2)	V_{oc} (V)	FF	PCE (%)
Cu	-7.4	770	47	2.6
Ag	-8.1	505	46	1.8
Alloy/Ni	-8	770	47	2.9
ITO	-7.3	760	51	2.9

in efficiency due to light intensity uncertainty in both cells is assumed to be ±5%.

Due to instrumentation related reasons an additional error in current of the alloy/Ni layers is present, increasing the error in the measurements of the cells.

With respect to the ITO devices, the OSC cell incorporating the Ni capped Ag/Cu (50%-50%) alloy TC shows higher J_{sc}, V_{oc} and slightly lower FF, the latter possibly due to a higher value of shunt resistance. Both the ITO and alloy cells have the same PCE (2.9%), whereas devices made of Cu/Ni 1 nm show a promising PCE reaching 90% of that of ITO based devices, thus still lower than the alloy ones. The lower J_{sc} for the ITO based devices could be due to its higher sheet resistance and lower microcavity effect which is more prevalent in metal based device due to their higher reflectance in the visible region compared to ITO. Devices incorporating Ag electrodes did not work properly. This could be due to the fact that the transmission of Ag monolayer film is lower in the optical region where the active medium has highest absorption of the photons. Despite having lower

R_s, the lower PCE of the devices incorporating single component metal TCs confirms the fact that a flat optical spectrum is essential for the high performance.

6.4 Performances of OSC device with Ag/AZO bilayer

The best structures of Ag(11)/AZO(30) based TCs were used to fabricate OSCs. 1 nm-thick nickel is added to enhance the work function and stability of the Ag/AZO anode [25]. The developed TCs were used as anode in OSCs with the following structure: Anode/MoO3(5nm)/ [fluorinated zinc phthalocyanine, F4-ZnPc] ID345:[Fullerene] C60(1:1,35nm)/C60(25nm)/ [(4,7-diphenyl-1,10-phenanthroline)] Bphen(5nm)/Ag(100nm). The *I–V* curves, comparing the performance of devices incorporating Ag/AZO/Ni and ITO anodes, are shown in Figure 6.7 and the corresponding electrical characterization data are reported in Table 6.2. The values for V_{oc} and FF for Ag/AZO/Ni and ITO devices are practically the same. The main difference between the devices is in J_{sc}. However, the device incorporating an Ag/AZO/Ni anode shows more than 90% of the efficiency of that incorporating ITO.

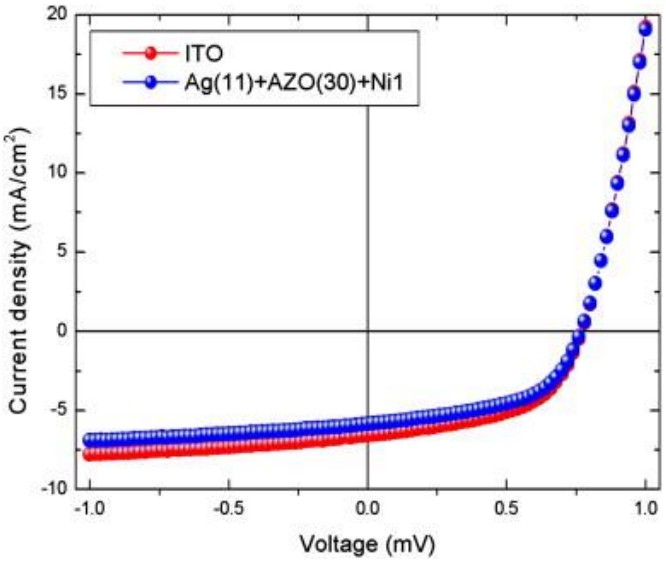

***Figure 6.7**: Comparison of the J-V curves of the solar cells fabricated using the reference ITO and Ag(11)+AZO(30) based TC.*

***Table 6.2**: Photovoltaic performance parameters of the solar cells.*

	J_{sc} (mA/cm^2)	V_{oc} (V)	FF	PCE (%)
Ag/AZO	7.3	760	53	2.6
ITO	6.6	760	53	2.9

6.5 Ag-Ni based TC into OSC device

In collaboration with BASF, the functional potential of the Ag-Ni bilayer structure was demonstrated by fabricating an OSC on glass. The proposed TC was used as anode in the following device architecture: Anode/MoO_3 (5nm)/[fluorinated zinc phthalocyanine, F4-ZnPc] ID345: [Fullerene]C60[1:1,35nm])/C60(25nm)/[4,7-diphenyl-1,10.phenanthroline)]Bphen(5nm)/Ag(100 nm). The cell performance was evaluated under simulated AM1.5G sunlight illumination. The J–V curves for the OSC devices integrating ITO and Ag–Ni TCs on glass substrates are shown in Figure 6.8 and the corresponding electrical characterization data are summarized in Table 6.3. Compared to the ITO-based device, the OSC incorporating Ag–Ni TC shows lower J_{sc} and similar V_{oc}, but it has lower FF which is due to the higher value of shunt resistance. The ITO cell has PCE (%) of 2.67%, whereas the devices incorporating of Ag7–Ni1 nm show a PCE (%) of 2.48%, thus 92% of that of ITO based devices.

***Table 6.3**: List of electrical characterization data for the OSCs device.*

	J_{sc} (mA/cm^2)	V_{oc} (V)	FF	PCE (%)
ITO	6.58	765	53	2.67
Ag-Ni	6.53	760	50	2.48

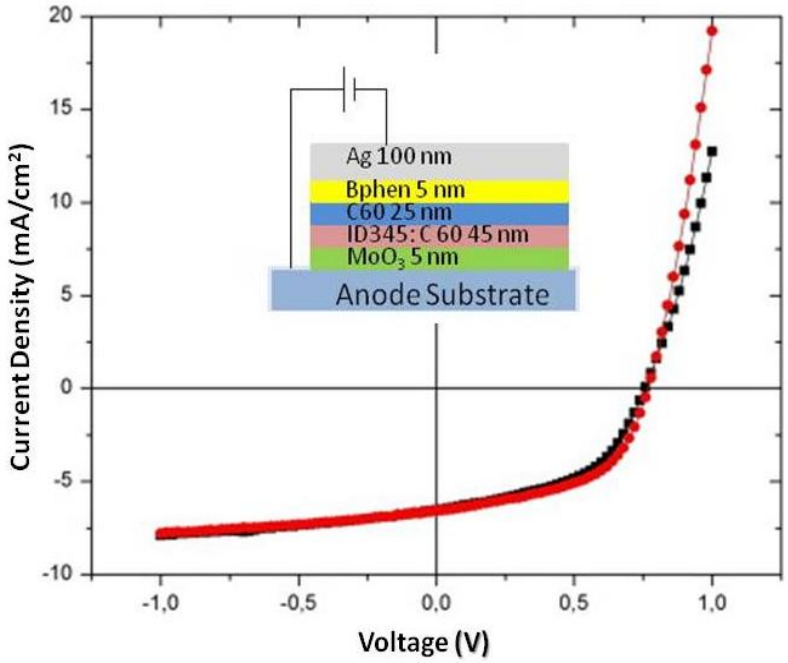

***Figure 6.8**: I–V curves of OSCs incorporating Ag7–Ni1(■) and ITO(●) anodes.*

6.6 AZO/TiO_x TC for inverted OSC devices

In collaboration with the Organic Nanostructured Photovoltaics group at ICFO, the developed AZO/TiO_x TC has also been used in Polymer Solar Cells (PSCs). Inverted solar cells were fabricated by blending PTB7 (1-material, Canada) with $PC_{71}BM$ (ADS, USA) at a 1:1.5 ratio (10 mg mL^{-1} of polymer) and dissolved in a mixed solvent system composed of chlorobenzene (CB) and 1,8-diiodooctane (DIO) (97:3 v/v%). The used structure of the inverted solar cell was as follows: cathode/ZnO/active layer/MoO_3/Ag being the cathode ITO, AZO or AZO/TiO_x. The blend PTB7:$PC_{71}BM$ was spin coated over the different cathodes using the same experimental conditions under controlled atmosphere in a globe box. The anode composed of MoO_3/Ag was thermally evaporated through a mask (0.096 cm^2) in an evaporator connected to the same globe box. The *I–V* characteristics were obtained under a 1 sun AM 1.5G spectrum illumination from a solar simulator (Abet Technologies model Sun 3000). Solar simulator illumination intensity was monitored using a

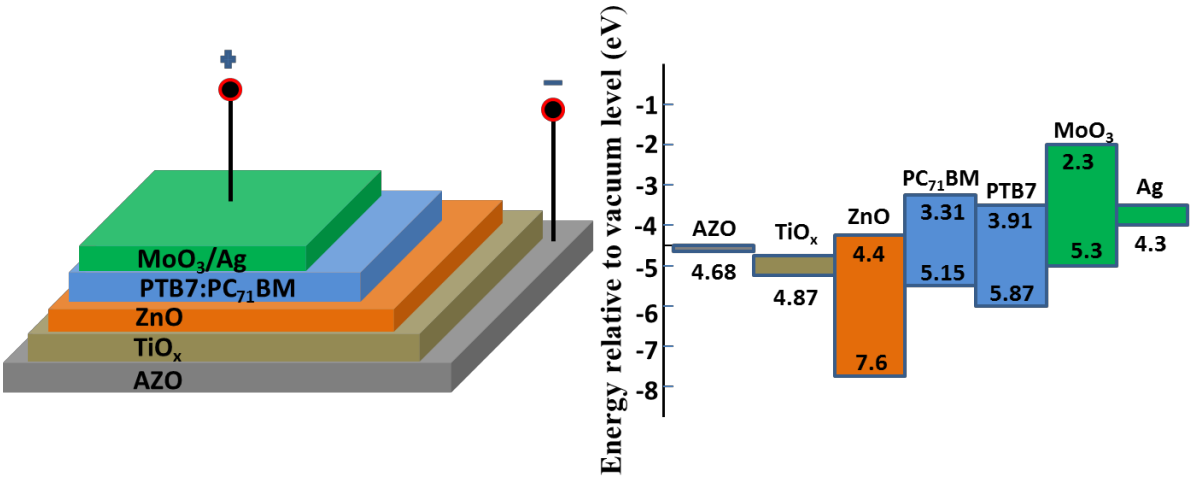

***Figure 6.9**: (left) Device configuration and (right) the energy band diagram of the inverted organic solar cell.*

monocrystal silicon Reference cell (Rera Systems) calibrated against a National Renewable Energy Laboratory (NREL) calibrated reference cell. EQEs were measured using a QEX10 Quantum Efficiency Measurement System from PV Measurements, Inc. For the EQE measurements, the devices were illuminated using monochromatic light from a xenon lamp passing through a monochromator. A calibrated monosilicon diode with a known spectral response was used as a reference inverted PSCs were fabricated over the more commonly used ITO electrode and both AZO TCs developed in this study. PTB7 photovoltaic polymer was chosen as it is one of the best performance polymers reported to date. The architecture of the fabricated AZO/TiO_x device is shown in Figure 6.9 (left) together with the corresponding energy level diagram (right). The approximate work functions of AZO and AZO/TiO_x films, measured experimentally by a Kelvin Probe Force Microscopy, were 4.68eV and 4.87eV, respectively. The J–V curves of the fabricated devices are showed in Figure 6.10 8a). Table 6.4 summarized the J_{sc}, V_{oc}, FF, and PCE of the best devices using ITO, AZO, and AZO/TiO_x as cathodes. When the solar cell device was fabricated on glass/AZO substrates we achieved a PCE of 6.6% with a J_{sc} of 12.0 mA cm^2, a V_{oc} of 0.737V, and a FF of 0.75. When the solar cell device was fabricated on glass/AZO/TiO_x substrates, we achieved

a PCE of 6.3% with a J_{sc} of 12.1mA cm^2, a V_{oc} of 0.732V, and a FF of 0.72. Meanwhile, for the solar cell device fabricated on glass/ITO commercial substrates the J_{sc} ,V_{oc} , and FF obtained were 12.7mA cm^2, 0.737V, and 0.74, respectively, which resulted in a PCE of 7%. The cells on bare ITO and AZO-based substrates show very similar behavior. When a thin Ti oxidized layer is deposited on AZO surface the V_{oc} of the inverted so-lar cell is reduced by less than a 1%. The energy level difference between the HOMO level of ZnO and the work function of TiO_x can explain this slightly reduction of V_{oc} according to the metal-insulator-metal model [26]. Also a slightly difference in the value of the FF of the AZO/TiOx electrode is observed regarded to the AZO or ITO TCs. However, noticeably, the FF values obtained for the different transparent-electrode devices are over 70% which is indicative of low series resistances in the devices. The efficiency losses of the AZO-based devices in comparison with the ITO reference device is mainly due to a 5.5% decrease in the short circuit current for the AZO device and a 4.7% decrease in the short circuit current for the AZO/TiO_x device. The difference in J_{sc} between the reference device and AZO-based cells can be clearly seen in the EQEcurves, shown in Figure 6. 10 (b) where a different distribution of energy absorption can be observed. With respect to the ITO reference, the slightly lower transmittance together with the Fabry-Perot oscillations presented by the AZO-based devices resulted in less energy absorption at 500 nm and between 600 nm and 700 nm where the active material absorbs light. Noticeably, the situation is favorable for the AZO-based devices at around 400 nm and 450 nm where the energy absorption is larger than that of the ITO reference device, which partially compensates the current loss at larger wavelengths. The obtained PCE compares favorably to the state-of-the-art where AZO films are used as TCs for PSCs. In fact, our work has achieved the highest PCE using AZO based TC reported so far.

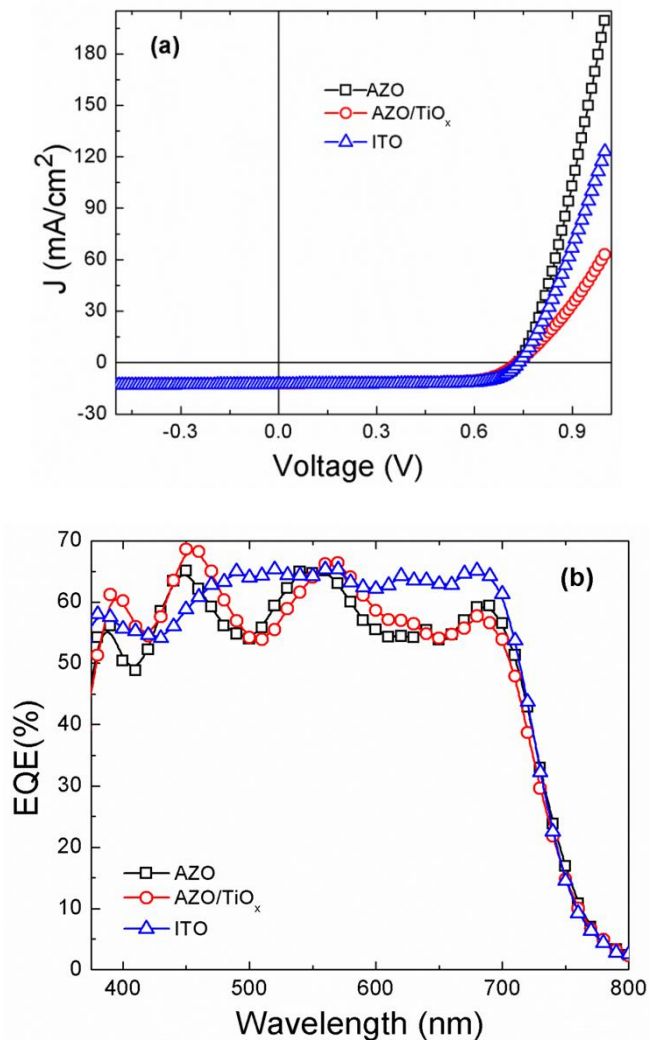

***Figure 6. 10**: (a) J-V curves of the inverted PTB7:PC71BM solar cells with AZO and AZO/TiO_x layers under a 1 sun AM 1.5G spectrum illumination (b) corresponding **EQE** spectra. The ITO-based device curves are shown for comparison.*

***Table 6.4**: Device performance of the inverted organic solar cell with different TCs used as cathodes.*

TC	J_{sc} (mA/cm^2)	Voc (V)	*FF*	*PCE* (%)
AZO	12.0	0.737	0.75	6.6
AZO/TiO_x	12.1	0.732	0.72	6.3
ITO	12.7	0.737	0.74	7.0

6.7 TiO_2/Ag/AZO based polymer solar cell on flexible glass

In collaboration with the Organic Nanostructured Photovoltaics group at ICFO and Corning, the TiO_2/Ag/AZO based TCs were incorporated in the into Polymer Solar Cells devices with the following configuration: flexible Willow Glass/TiO_2/Ag/AZO/ZnO/PTB7:$PC_{71}BM$/MoO_3/Ag (Figure 6.11). The active layer was based on a PTB7:$PC_{71}BM$ film, which is a well characterized photoactive material system that constantly shows PCEs over 6% when incorporated into PSCs, but with few reports of ITO-free solar cells. The reference devices were made with commercially available ITO-coated (100 nm) glass substrates of 1.1 mm thickness [27]. This inverted device structure has been shown to have better ambient stability and be compatible with roll-to-roll coating process [28-29].The current density–voltage (*J–V*) curves together with the External Quantum Efficiency (EQE) curves of the fabricated devices are shown in Figure 6.12. The photovoltaic parameters of PSCs fabricated from TiO_2/Ag/AZO and ITO based TCs on glass are summarized in Table 6.5. When comparing with its ITO counterparts, the PSCs based on TiO_2/Ag/AZO show similar open circuit voltage, enhanced fill factor and lower photocurrent. The similar V_{OC} demonstrates that there is a good ohmic contact between the trilayer TC and the subsequent electron transporting layer, as expected from the kelvin probe measurement. An enhanced fill-factor (FF) follows the improved R_S of the trilayer TC, while the reduced photocurrent is evidenced in the IV

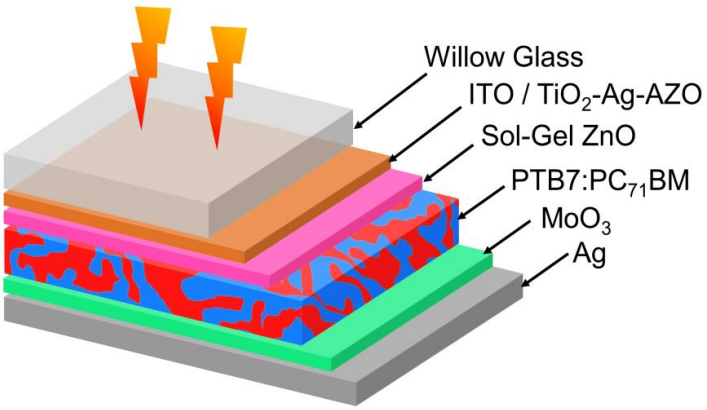

Figure 6.11: *Structure of the fabricated polymer solar cell.*

Table 6.5: *Solar cell parameters for TiO_2(x)/Ag 8 nm/AZO 40 nm samples*

Cell	J_{SC} (mA/cm^2)	V_{OC} (mV)	FF (%)	PCE (%)
Ref ITO	14.3	754.7	69.9	7.5
TiO_2 46 nm/Ag 8 nm/AZO 40nm Electrode	11.8	745.3	72.8	6.4
TiO_2 34 nm/Ag 8 nm/AZO 40nm Electrode	12.1	738.9	73.4	6.6

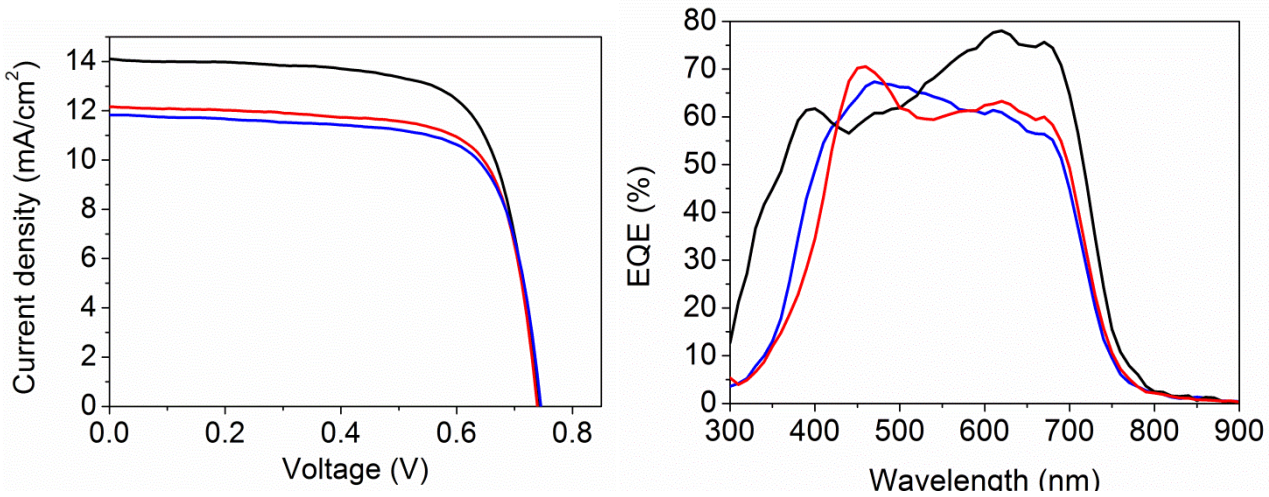

Figure 6. 12*:(left) J-V curves and (right) EQE curves of (black) ITO reference device, (blue) TiO_2 46 nm/Ag 8 nm/AZO 40 nm TC and (red) TiO_2 34 nm/Ag 8 nm/AZO 40 nm TC .*

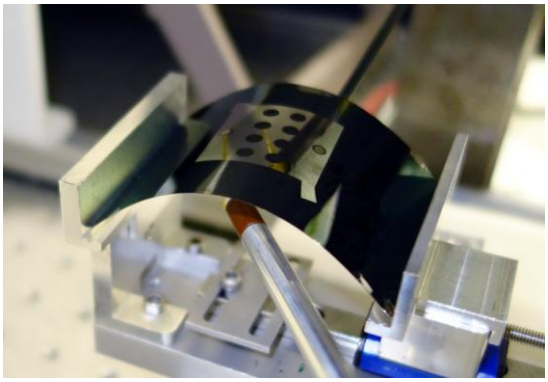

Figure 6.13: *Picture of the TiO_2/Ag/AZO based polymer solar cell during the static and cyclic 2-point bend testing.*

and EQE curves, where the devices on trilayer TCs remain below the reference for the longer wavelengths where the photon flux is higher. Further optical optimization of the TC can lead to increase the photocurrent and overcome the efficiencies of ITO based devices. The PSCs based on the composite TC of TiO_2/Ag/AZO on flexible glass substrates exhibit excellent cell-performances achieving more than 85% of the efficiency of the ITO reference, making this TC a suitable alternative to ITO ones and a promising technology for the realization of flexible ITO-free photovoltaic devices.

To evaluate the mechanical flexibility of the device fabricated on the proposed TC, we measured the PSC parameters as a function of the bending radius and after multiple cycles in a 2-point bend configuration. Figure 6.13 shows a picture illustrating the bending capability of the solar cell, while Figure 6.14 the photovoltaic parameters normalized to the flat geometry (no bending) for different radii of curvature. The maximum bending strain applied to the substrate was approximately 0.16 %, calculated from $\varepsilon = h_S/(2R)$, where h_S is the thickness of the flexible glass substrate and R is the maximum bending radius [30]. When decreasing the bending radius from 6 cm to 3 cm, the V_{OC} and short circuit current (J_{SC}) do not change significantly, always above 95% of the flat geometry's values. The FF also is subjected to similar changes but with a fluctuating behaviour for different bending positions (Figure 6.14 c). Most of these unexpected fluctuations can be attributed to changes in the electrical contact of the probes used during the measurements rather than being an intrinsic and systematic device response to bending. Regardless, the negligible change in FF is related to that of the TC's R_S (Figure 6.15). Finally, the PCE, as an overall indicator including all the aforesaid parameters, shows a trend similar to that of FF, with a value that remains clearly above 92% of that of the reference flat sample for all bending radii.

Performances as a function of number of bending cycles are shown in Figure 6.16. The maximum and minimum radii were 6 and 3 cm respectively and the percentages are relative to the values

measured at 6 cm bending radius. Figure 6.16a shows that the V_{OC} and J_{SC} decreased only slightly (1%), while the small increase in FF indicates that R_S of the TC increased under continuous bending. Overall, one can see from Figure 6.16 b that even after 400 bending cycles the PSC on Willow flexible glass remains at 94% of its initial value.

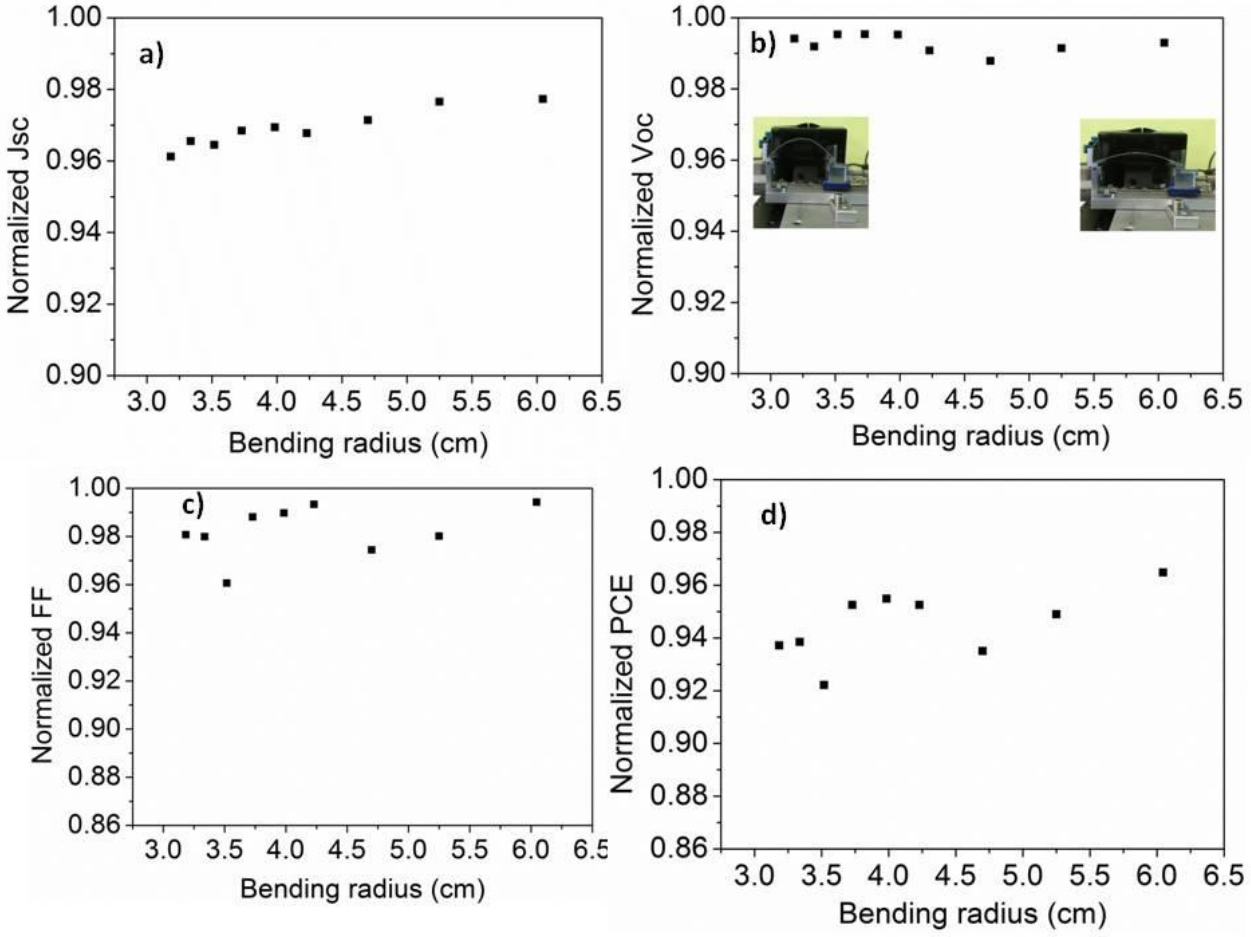

Figure 6.14: *Normalized (a) J_{SC}, (b) V_{OC}, (c) FF and (d) PCE as a function of the bending radius. The inset in (b) shows the bending set up at the maximum and minimum bending radius.*

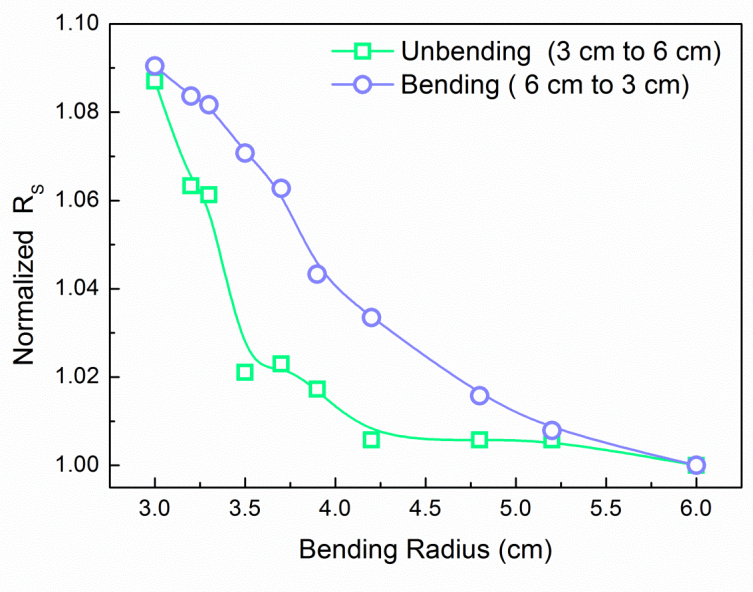

Figure 6.15: *Sheet resistance change of the TiO_2/Ag/AZO TC during reversible bending test.*

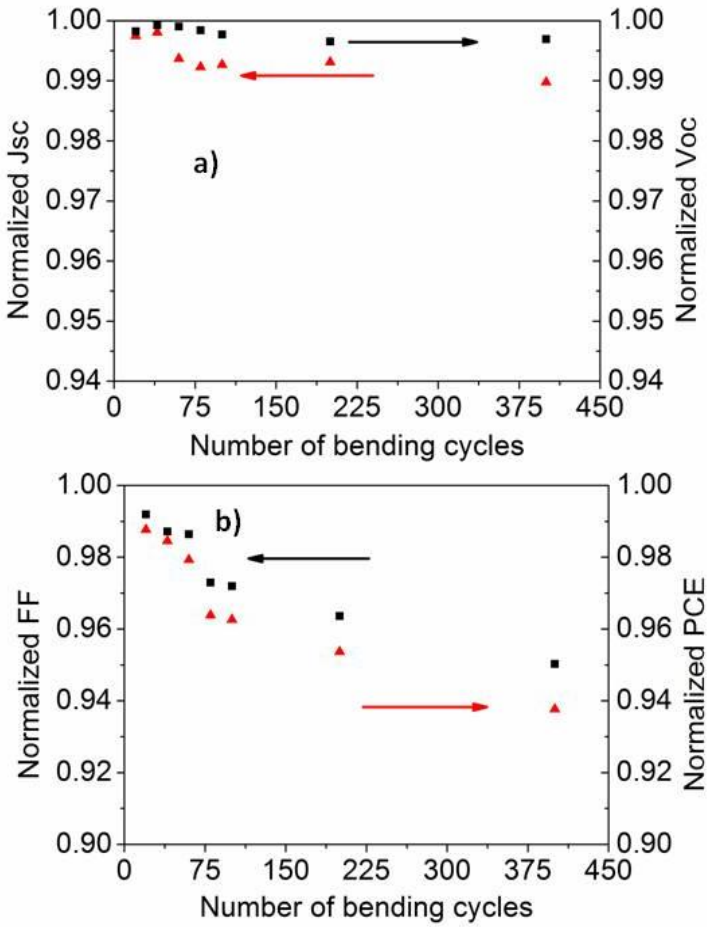

Figure 6.16*: Normalized (a) J_{SC} and V_{OC}, (b) FF and PCE as a function of bending cycles.*

References

[1] British Petroleum, 2012.

[2] World Watch Institute, 2012.

[3] National Renewable Energy Laboratory, 2013.

[4] J.-L. Wu, F.-C. Chen, Y.-S. Hsiao, F.-C. Chien, P. Chen, C.-H. Kuo, M.H. Huang, C.-S. Hsu, ACS Nano 5, 959, 2011.

[5] K. Petritsch, TechnischeUniversitat Graz Austria Doctoral Thesis 1, 159, 2000.

[6] M. Reyes-reyes, I. Cruz-cruz, D. San, L. Potosı, 20220, 2010.

[7] C. Tao, S. Ruan, G. Xie, X. Kong, L. Shen, F. Meng, C. Liu, X. Zhang, W. Dong, W. Chen, Applied Physics Letters 94, 043311, 2009.

[8] N.P. Sergeant, A. Hadipour, B. Niesen, D. Cheyns, P. Heremans, P. Peumans, B.P. Rand, Advanced Materials 24, 728, 2012.

[9] R. Betancur, A. Martínez-Otero, X. Elias, P. Romero-Gómez, S. Colodrero, H. Miguez, J. Martorell, Solar EnergyMaterials and Solar Cells 104, 87, 2012.

[10] M.D. Irwin, D.B. Buchholz, A.W. Hains, R.P.H. Chang, T.J. Marks, 2, 2007.

[11] R. Betancur, M. Maymó, X. Elias, L.T. Vuong, J. Martorell, Solar Energy Materials and Solar Cells 95, 735, 2011.

[12] W. Cai, X. Gong, Y. Cao, Solar Energy Materials and Solar Cells 94, 114, 2010.

[13] Z. He, C. Zhong, X. Huang, W.-Y. Wong, H. Wu, L. Chen, S. Su, Y. Cao, Advanced Materials (Deerfield Beach, Fla.) 23, 4636, 2011.

[14] R. Betancur, A. Martínez-Otero, X. Elias, P. Romero-Gómez, S. Colodrero, H. Miguez, J. Martorell, Solar EnergyMaterials and Solar Cells 104, 87, 2012.

[15] B.E. Lassiter, G. Wei, S. Wang, J.D. Zimmerman, V.V. Diev, M.E. Thompson, S.R. Forrest, Applied Physics Letters 98, 243307, 2011.

[16] C.J. Brabec, S.E. Shaheen, C. Winder, N.S. Sariciftci, P. Denk, Applied Physics Letters 80 1288, 2002.

[17] K.-S. Liao, S.D. Yambem, A. Haldar, N.J. Alley, S. a. Curran, Energies 3, 1212, 2010.

[18] T.L. Chen, R. Betancur, D.S. Ghosh, J. Martorell, V. Pruneri, Applied Physics Letters 100 013310, 2012.

[19] D.S. Ghosh, R. Betancur, T.L. Chen, V. Pruneri, J. Martorell, Solar Energy Materials and Solar Cells 95, 1228, 2011.

[20] L. Huo, S. Zhang, X. Guo, F. Xu, Y. Li, J. Hou, AngewandteChemie (International Ed. in English) 50, 9697, 2011.

[21] Y. Liang, Z. Xu, J. Xia, S.-T. Tsai, Y. Wu, G. Li, C. Ray, L. Yu, Advanced Materials 22, E135, 2010.

[22] Würfel , Physics of Solar Cells: From Principles to New Concepts, Wiley-VCH, 2005.

[23] Quaschning, V.: Technology Fundamentals - The Sun as an Energy Resource. Renewable Energy World 6, 5, 90, 2003.

[24] W. Yu, L. Shen, F. Meng, Y. Long, S. Ruan, W. Chen, Solar Energy Materials and Solar cells 100,226, 2012.

[25] J.C. Bernède, Y. Berredjem, L. Cattin, M. Morsli, Applied Physics Letters, 92, pp. 83304, 2008.

[26] V. D. Mihailetchi, L. J. A. Koster, J. C. Hummelen, and P. W. M. Blom, Phys. Rev. Lett. 93, 216601, 2004.

[27] H. Hoppe, N. S.Sariciftci, J. Mater. Chem. 2006, 16, 45.

[28] Y. Liang, Z. Xu, J. Xia, S. T. Tsai, Y. Wu, G. Li, C. Ray, L. Yu, Adv. Mater. 2010, 22, E135–E138.

[29] S. K. Hau, H. L. Yip, N. S. Baek, J. Zou, K. O'Malley, A. K. Y. Jen, Appl. Phys. Lett. 2008, 92, 253301-1.

[30] S. Park, J. H. Ahn, X. Feng, S. Wang, Y. Huang, and J. A. Rogers, Adv. Funct. Mater. 2008, 18, 2673.

Chapter VII

Conclusions and future work

This Thesis has investigated the potentials of Ultrathin Metals Films (UTMFs) and their combination with Transparent Conductive Oxides (TCOs), such as Aluminum doped Zinc Oxide (AZO), as Transparent Conductors (TCs) for organic solar cells (OSCs).

A TC is a key element in almost any optoelectronic device, including organic light emitting diodes (OLEDs) and OSCs. An ideal TC must be highly transparent to allow the maximum amount of light through and, at the same time, conductive to provide adequate and uniform electrical current density. This is the case of indium doped tin oxide (ITO), which is the most widely used TC in industry today. Although ITO offers very high electro-optical performance, it suffers from several drawbacks: (i) high cost of indium which is a scarce element, (ii) low compatibility with organic materials, (iii) poor mechanical flexibility and (iv) high temperature processing.

In this thesis it has been demonstrated that UTMF based TCs are an effective and viable alternative to ITO. In fact, they exhibit high optical transmittance and electrical conductivity, their work function can be easily tuned by choosing different metals, are mechanically more stable and flexible than ITO, and they can be fabricated over large areas by low cost roll-to-roll production. Another crucial advantage for many applications, for example flexible electronics on plastic substrate, is that UTMFs, unlike ITO, can be deposited at low temperatures, including room temperature.

Polymeric substrates such as polyethylene terephthalate (PET) can absorb a substantial amount of moisture which eventually penetrates through the film and potentially leads to the degradation of UTMFs and other devices' layers. The Thesis has also focused on solving this problem by developing effective barrier layers, which, besides stability, can enhance UTMFs adhesion to the substrate, without affecting their mechanical flexibility.

The developed UTMF based TCs were used to fabricate, on glass and polymer substrates, OSCs that showed efficiency comparable to that of ITO based devices.

The main outcomes of the Thesis include:

- An effective method to deposit atomically smooth ultrathin silver (Ag) films by employing ≤1 nm copper (Cu) seed layer, which provides energetically favorable nucleation sites. In this way, the Ag film undergoes a layer-by-layer growth mode resulting in a smaller grain size and extremely low surface roughness (<0.5 nm), while the minimum thickness required to obtain a continuous Ag film (percolation thickness) is reduced to 3 nm, compared to 6 nm without the seed layer. The resulting optical and electrical properties are much better than those obtained without Cu seeding, especially for thicknesses below 6 nm.
- The combination of different UTMFs to form novel TCs structures, for example, ultrathin Ag films and Cu-Ag alloys capped by a 1nm Ni layer. The ultrathin Ni capping layer enhances he stability against temperature and oxidation without affecting the electro-optical properties and provides also larger work function. The performances of Ag and Ag-Cu alloy-Ni based TCs have been investigated in OSCs, achieving conversion efficiencies of 2.48%, and 2.9 %, respectively that correspond to 92 to 100% % of those with similar ITO based devices.
- The development of bilayer doped metal oxide/metal (AZO capped Ag nano-thick film) which can overcome the high reflection of metals and retain their good electrical behavior, while still keeping the minimum total film-thickness. Electrical and optical properties as well as environmental stability of the doped metal oxide/metal bilayer structure were theoretically and experimentally studied. It has also been assessed that the combined structure can act both as anode and hole transporting layer in OSCs, achieving a conversion efficiency of 2.6%, compared to 2.9% obtained by using ITO.

- An hybrid TC consisting of AZO layer capped with an ultrathin oxidized Ti filmto protect AZO from degradation in harsh environment. The oxidized Ti increases the chemical, environmental, stability and the surface smoothness of AZO while still maintaining its electrical and optical properties. The application potential of the TC is demonstrated in an inverted Polymer Solar Cell (PSC), which shows an efficiency of 6.3%, very close to the value (7%) obtained in a similar structure using ITO. This efficiency is the highest reported to date for PSCs incorporating AZO based TCs.
- a TiO_2/Ag/AZO trilayer TC on flexible thin glass sheets, which shows remarkably low roughness, high optical transmission, low electrical sheet resistance, and high mechanical robustness under repetitive bending cycles. The use of thin glass carries several advantages with respect to more common polymeric substrates, such as higher surface quality, impermeability to oxygen and moisture and the possibility of higher temperature processing. The polymer solar cell built upon this TC results in an efficiency of 6.6 %, which is more than the 85% of that of a reference cell on conventional ITO substrate.

Besides optimizing further the TC structures developed in the Thesis, future work should focus on their environmental and mechanical stability. Damp heat tests in humid and high temperature environments as well as bending tests will be extensively performed on TC deposited on both flexible polymeric and glass substrates. In addition, besides deposition, a simple process flow includes an effective way to pattern the developed TCs, this being crucial for low cost mass production. This activity will also be part of future research.